DEVELOPMENT OF A HYBRID ANTI-ICING COATING WITH SUPERHYDROPHOBIC AND ELECTROTHERMAL PROPERTIES

By

© ANDREW G. SULLIVAN

A thesis submitted to the School of Graduate Studies in partial fulfillment

of the requirements for the degree of

MASTER OF ENGINEERING

Faculty of Engineering and Applied Science

Memorial University of Newfoundland

October 2022

St. John’s, Newfoundland and Labrador

Canada

ABSTRACT

This work involves the development of a hybrid anti-icing coating. The multi-layered coating consists of an electrothermal heating film and superhydrophobic top coating. The heating film is composed of a thin layer of conductive copper-based epoxy, insulated between layers of a polydimethylsiloxane (PDMS) elastomer. The superhydrophobic coating is based on FAS-13 modified SiO_2 nanoparticles dispersed in a PDMS matrix. The composite coating was applied to a stainless steel substrate by consecutively depositing each layer by spray-coating.

The SiO_2/PDMS coating exhibited a static contact angle of 164.3° and contact angle hysteresis of 2.8°, confirming its superhydrophobic properties. The anti-icing properties of the superhydrophobic coating were investigated experimentally inside a cold chamber at -20°C. The ice adhesion strength was reduced from 284 kPa on the untreated substrate to 50 kPa on the superhydrophobic coating, while the droplet freezing time was delayed from 8 seconds to 76 seconds. The heating film demonstrated a fast thermal response and excellent thermal stability. With the maximum surface power density of 3.46 W/cm^2, the surface temperature of the heating film could be raised to 10°C in just 45 seconds.

In simulated spray-icing tests, the hybrid superhydrophobic-heating film achieved complete anti-icing with a minimum surface power density of 0.26 W/cm^2. Consequently, the superhydrophobic coating was found to reduce the energy required for anti-icing of the heating film by 41%. The hybrid coating was found to be durable and retained its superhydrophobicity after being subjected to repeated icing and de-icing cycles. The results demonstrate that the hybrid coating has potential for practical applications in the marine and offshore industries due to its simple, versatile fabrication process and energy-efficient anti-icing performance.

ACKNOWLEDGEMENTS

I would like to express my deepest gratitude to my supervisor, Dr. Xili Duan, for his continued support and encouragement over the past two years. His guidance allowed me to overcome numerous challenges throughout my research and it was a pleasure to work under his supervision. I would also like to thank my co-supervisor, Dr. James Yang, for sharing his expertise and insight.

I sincerely appreciate the assistance provided by the students in our research group, whose knowledge and experience in the lab were instrumental in the development of my experimental setup and processes.

I gratefully acknowledge the financial support received from the Ocean Frontier Institute (OFI) and the School of Graduate Studies of Memorial University of Newfoundland that made this research possible.

Finally, I would like to thank my parents, grandparents, and friends for their constant love and support throughout my program.

TABLE OF CONTENTS

LIST OF FIGURES

LIST OF TABLES

LIST OF ABBREVIATIONS

ACA	Advancing Contact Angle
BSE	Backscattered Electron
CA	Contact Angle
CAH	Contact Angle Hysteresis
CBS	Circular Backscatter
CNT	Carbon Nanotube
CVD	Chemical Vapour Deposition
DC	Direct Current
ETD	Everhart-Thornley Detector
EHT	Electrical Heat Tracing
FPS	Frames per Second
GFRP	Glass Fiber Reinforced Polymer
HF	Heating Film
HVLP	High-volume Low-pressure
IAS	Ice Adhesion Strength
IR	Infrared
MWCNT	Multi-walled Carbon Nanotube
PCC	Phantom Camera Control
PH	Precipitation Hardening
PS	Polystyrene
PTFE	Polytetrafluoroethylene
PU	Polyurethane
PDMS	Polydimethylsiloxane
RCA	Receding Contact Angle
SA	Sliding Angle
SB	Sandblasted
SEM	Scanning Electron Microscope
SEI	Secondary Electron Imaging
SHC	Superhydrophobic Coating
SH-HF	Superhydrophobic Heating Film
SH-SS	Superhydrophobic Stainless Steel
SS	Stainless Steel
TTFOS	Triethoxy-1H,1H,2H,2H-tridecafluoro-n-octylsilane (FAS-13)

NOMENCLATURE

A_c	Ice-solid Contact Area	m²
A	Surface Area	m²
CAH	Contact Angle Hysteresis	°
c_p	Specific Heat Capacity	J/kg·K
d	Sample Thickness	m
f	Solid Contact Area Fraction	-
F_{max}	Peak Ice Removal Force	N
g	Gravitational Acceleration	m/s^2
h	Total Heat Transfer Coefficient	W/m^2·K
h_C	Convection Heat Transfer Coefficient	W/m^2·K
h_R	Radiation Heat Transfer Coefficient	W/m^2·K
I	Electric Current	A
k	Thermal Conductivity	W/m·K
L	Characteristic Length	m
Nu	Nusselt Number	-
P_d	Surface Power Density	W/m²
P_{el}	Electrical Power	W
$\dot{Q}_{cond}$	Conductive Heat Transfer Rate	W
$\dot{Q}_{conv}$	Convective Heat Transfer Rate	W
Q_d	Energy Density	J/m²
$\dot{Q}_{net}$	Net Heat Transfer Rate	W
$\dot{Q}_{rad}$	Radiation Heat Transfer Rate	W
r	Roughness Factor	-
R	Electrical Resistance	Ω
R_o	Electrical Resistance at Reference Temperature	Ω
R_s	Sheet Resistance	Ω/sq
Ra	Rayleigh Number	-
t	Time	s
t_f	Film Thickness	m
T	Temperature	K
ΔT	Temperature Rise	K
T_o	Environmental Temperature	K
T_{ss}	Steady State Temperature	K
V	Volume	m^3

w_A	Work of Adhesion	J/m²
α	Temperature Coefficient of Resistance	K^{-1}
β	Volumetric Thermal Expansion Coefficient	K^{-1}
γ_{SL}	Solid-liquid interfacial energy	J/m²
γ_{SA}	Solid-air interfacial energy	J/m²
γ_{LA}	Liquid-air interfacial energy	J/m²
ε	Thermal Emissivity	-
θ	Young's Contact Angle	°
θ_A	Advancing Contact Angle	°
θ_{CB}	Cassie-Baxter Contact Angle	°
θ_M	Mixed Model Contact Angle	°
θ_R	Receding Contact Angle	°
θ_W	Wenzel Contact Angle	°
κ	Thermal Diffusivity	m²/s
ν	Kinematic Viscosity	m²/s
ρ	Density	kg/m^3
ρ_{el}	Electrical Resistivity	Ω·m
σ	Stefan-Boltzmann Constant	$W/m^2 \cdot K^4$
τ	Shear Ice Adhesion Strength	N/m²
τ_c	Time Constant	s

CHAPTER 1

Introduction

1.1 Background

The reduction in the extent and duration of arctic sea ice driven by climate change has resulted in an increase in shipping activity in Arctic waters. The number of unique vessels operating in the Arctic increased by 25% from 2013 to 2019, and the total distance sailed increased by 75% in the same period [1]. The continued increase in Arctic shipping activity has exposed a need for more effective and efficient ice protection technologies for offshore vessels and structures operating in the region.

Undesirable ice accretion can cause damage to infrastructure, delay operations, and present safety hazards to personnel due to falling ice, slippery walking surfaces, blocked access to safety and process equipment, and loss of vessel stability [2]. Traditionally, accumulated ice on offshore vessels and structures has been removed using manual methods. Due to the risk to personnel and equipment associated with manual methods, numerous anti-icing and de-icing technologies have been developed to assist in mitigating ice accretion. Ice protection technologies can be divided into two categories: (i) active methods, which include mechanical, thermal, and chemical techniques; and (ii) passive methods, including surface modification and icephobic coatings [3]. Active ice protection methods are effective and reliable but tend to be expensive, energy-intensive, or harmful to the marine environment. Passive methods are attractive due to their ability to prevent icing without requiring external energy. In reality, most passive methods can only delay icing while also requiring frequent maintenance to remain effective. Superhydrophobic coatings have been demonstrated to effectively delay ice accretion and facilitate ice removal. However, the widespread adoption of superhydrophobic coatings has been limited by their high cost, complex

fabrication methods, and low durability. Therefore, there exists a need for the development of robust, energy-efficient, and cost-effective ice protection techniques for offshore applications.

1.2 Research Objectives

This thesis presents a detailed study into the development and experimental characterization of a hybrid superhydrophobic-electrothermal heating film for marine and offshore applications. The thin film electric heating element and superhydrophobic top coating are each applied to a metal substrate using a simple sequential spray coating process. A schematic drawing of the cross-section of the hybrid coating is presented in Figure 1.

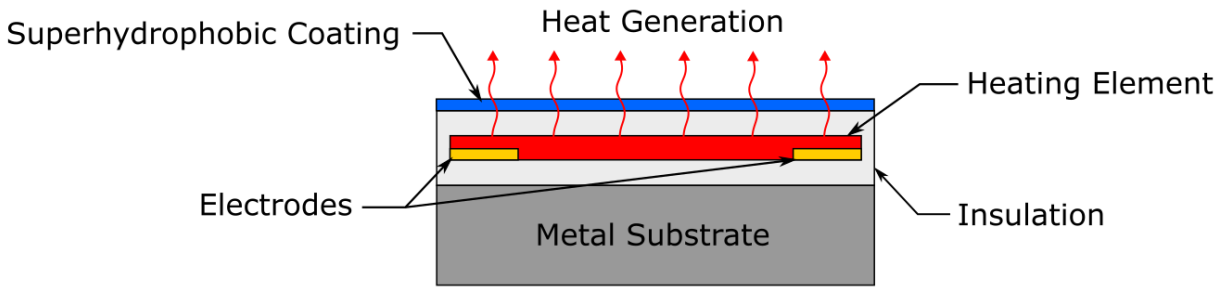

Figure 1: Schematic drawing of the proposed hybrid electrothermal/superhydrophobic anti-icing/de-icing coating.

The mechanism by which the hybrid superhydrophobic-electrothermal coating prevents icing is twofold. The superhydrophobic coating mitigates icing by allowing liquid water to roll off of the target surface before freezing, delaying the freezing process, and reducing the adhesion of ice to the surface. The electrothermal heating film can achieve anti-icing by converting electrical energy into heat to raise the temperature of the target surface above the freezing point of water. Combining the electrothermal heating film with a superhydrophobic top coating has a synergistic effect which can dramatically improve energy efficiency and enhance anti-icing performance when compared to either method alone. This effect was first reported by Antonini et al. [4] who demonstrated that applying a superhydrophobic coating to the heated leading edge of an airfoil could significantly

reduce the energy usage required for anti-icing. Zhao et al. [5] were the first to introduce the concept of the hybrid superhydrophobic – electrothermal anti-icing coating. The hybrid coating was shown to achieve anti-icing using 27% less energy than the electric heating coating alone. Moreover, the heating effect can extend the longevity of the superhydrophobic coating by reducing the amount of degradation caused by repeated freezing and thawing action [6]. Heating the surface also mitigates frost formation, allowing superhydrophobic coatings to remain effective at shedding water at lower temperatures.

In recent years, several other researchers have developed novel hybrid superhydrophobic-electrothermal coatings with unique materials, methods, and properties [6, 7, 8]. Many of these studies have focused on application to non-conductive glass, polymer, and composite substrates. Limited research has been performed thus far on the direct application to metal substrates which present an additional challenge during the fabrication process due to their electrical conductivity. The unique structure and material composition of the coating presented in this work allows for application to common engineering materials such as carbon steel, stainless steel, or aluminum alloys. Many of the existing coatings are fabricated using complex methods and advanced equipment. Designing the coating such that all of the materials can be applied by spray coating will simplify the fabrication process and facilitate scaling to large surfaces or complex geometry in practical applications. Further research can also present opportunities for improvements to the energy efficiency and durability of hybrid superhydrophobic-electrothermal coatings.

The primary research objectives of this thesis are listed as follows:

- Design a hybrid anti-icing coating consisting of an electric heating film and superhydrophobic top-coating for application to a metal substrate.

- Fabricate the coating using simple methods that are scalable for practical engineering applications.
- Characterize the surface wettability and surface morphology of the fabricated samples.
- Measure the key electrothermal properties and thermal response of the heating film.
- Compare the ice adhesion strength and droplet freezing time on the coated and uncoated surfaces.
- Verify the anti-icing and de-icing performance of the coating in a simulated spray icing environment and compare the energy consumption between samples.
- Evaluate the abrasion resistance and durability of the coating under repeated icing and de-icing cycles.

1.3 Thesis Outline

Chapter 2 reviews current and recent technological advances in ice protection methods, focusing primarily on those suitable for marine and offshore applications. The basic principles and models of wetting are also discussed in this chapter. The materials, methods, and anti-icing/de-icing properties of superhydrophobic coatings and electrothermal heating films are each reviewed and discussed in detail. Concluding this chapter, existing research on the topic of hybrid superhydrophobic-electrothermal coatings is presented and evaluated for later comparison to the coating developed in this work.

The materials for each component of the hybrid superhydrophobic-electrothermal coating are discussed in Chapter 3. An overview of the methods and equipment used in the sample preparation and spray coating processes is then provided. The experimental methodology and instruments used in the characterization of the surface wettability, microstructure, and electrothermal properties are introduced. The experimental methods employed to evaluate the anti-icing/de-icing performance

of the coating are presented, with an analysis of the uncertainties in the experimental processes concluding this chapter.

Chapter 4 details each stage of the fabrication process for the hybrid superhydrophobic-electrothermal coating. The static and dynamic contact angle measurement data is displayed and subsequent analysis of the wettability is performed. SEM micrographs of the samples were obtained to characterize the surface microstructure and describe the nature of the surface roughness features. The key electrothermal properties of the heating film were analyzed; including the thermal response time, temperature rise, power density, cycling stability, and temperature uniformity.

The anti-icing/de-icing capabilities of the hybrid coating are demonstrated in Chapter 5. The series of experiments presented in this chapter investigate the ice adhesion strength, droplet freezing time, and energy consumption for anti-icing and de-icing. Furthermore, the durability of the coating is evaluated by subjecting the samples to light abrasion and repeated icing/de-icing cycles.

Chapter 6 summarizes the main conclusions of the work presented in this thesis and provides several recommendations for future work.

CHAPTER 2

Literature Review

2.1 Sources of Marine Icing

There are two primary sources of icing in cold marine environments: atmospheric icing and sea spray icing. Atmospheric icing is a process in which freshwater ice is formed as a result of fog, precipitation, or water vapour in the air [9]. Atmospheric icing is the primary source of icing for stationary marine structures. As shown in Figure 2, elevated superstructures such as masts, antennas, derricks, and cranes are the most susceptible areas to atmospheric icing [9]. Precipitation such as snow, sleet, or freezing rain can also accumulate on horizontal surfaces such as decks, stairs, and helipads [2].

Figure 2: General locations susceptible to each type of icing on a semi-submersible drilling rig [10].

Sea-spray icing is caused by saltwater spray generated from waves, wind, and vessel interactions [11]. For stationary structures, the spray is only generated by waves impacting against the structure and the amount of spray can be minimized through structural design. For vessels in motion, significantly more spray is generated as waves impact the bow of the ship, as illustrated in Figure 3. Consequently, sea-spray icing is the dominant source of icing for vessels [9]. In reports from

ships in arctic seas, sea-spray alone contributed to 50% of icing cases, sea spray combined with atmospheric icing in 41% of cases, and atmospheric icing alone in just 9% of cases [9]. As shown in Figure 4, layers of ice up to 25cm thick can form per day during intense storms, which can add up to 1000MT of additional weight to a vessel in extreme cases [2]. Consequently, sea spray icing poses the greatest risk to the safety of offshore vessels and structures. Added weight can cause a vessel to lose stability and heel, potentially leading to the loss of the vessel. In addition, sea spray icing can create dangerous conditions for workers and damage or restrict access to critical process and safety equipment.

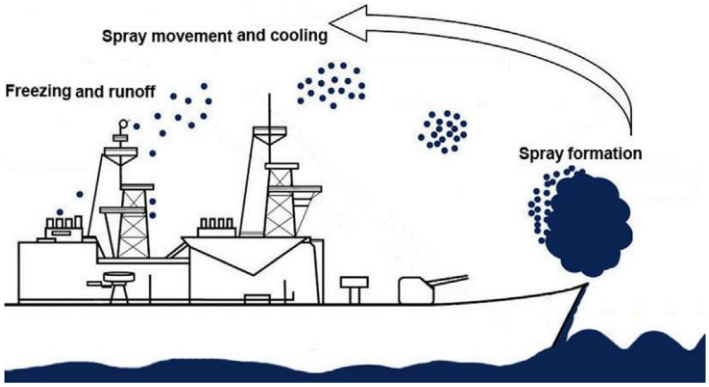

Figure 3: Sea-spray is generated by wave-bow interactions and is carried over the vessel before freezing [11].

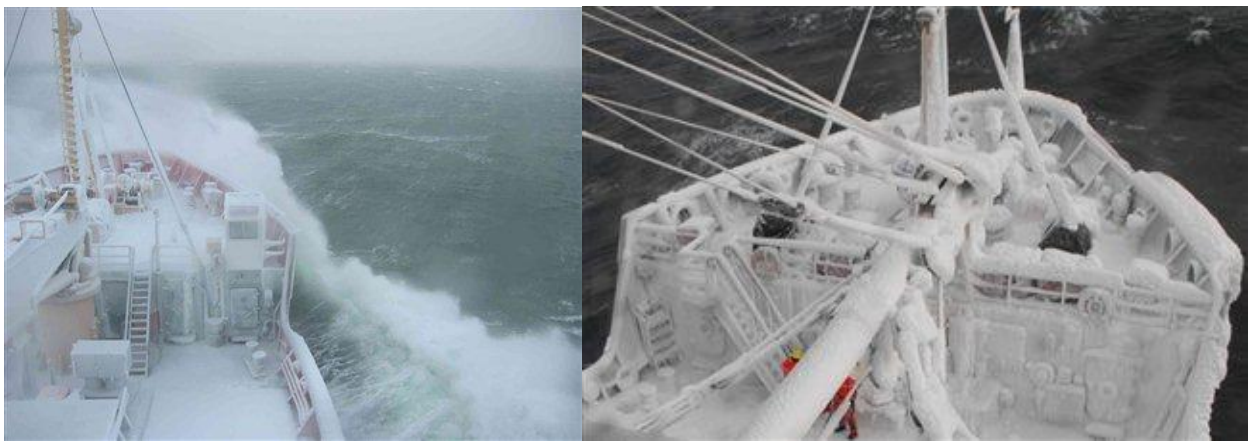

Figure 4: A Canadian Coast Guard Vessel during and after encountering severe sea-spray icing conditions [12].

2.2 Ice Protection Methods

Numerous ice protection techniques have been developed for industries affected by undesirable ice accretion. Ice protection techniques can be divided into two categories: anti-icing, where ice accumulation on a surface is delayed or completely prevented; and de-icing, where already accumulated ice is removed from a surface. Ice protection techniques can be further divided into three categories: active, passive, and hybrid techniques. Active techniques use external mechanical, thermal, or chemical energy to remove ice or prevent ice accumulation. Passive techniques are defined by their ability to provide ice protection without requiring any external energy input by manipulating surface properties. Recently developed hybrid techniques combine one or more active or passive methods to improve the effectiveness and efficiency of anti-icing/de-icing when compared with a single method.

Figure 5: Manual de-icing of a ship being performed by workers with hand tools [12].

Historically, manual force has been the primary technique for removing ice on vessels and offshore structures [10]. As shown in Figure 5, manual de-icing is accomplished using hand tools such as hammers, axes, and shovels. Manual de-icing remains commonplace for its simplicity, despite it being a slow, laborious, and dangerous process. The impact forces involved in manual de-icing can also damage equipment, chip paint, and accelerate wear [10]. Furthermore, manual methods are restricted to areas of a vessel or structure that are accessible to workers. Due to these

considerable limitations, alternative methods should be employed to replace manual methods whenever possible. Technological developments have provided safer and more efficient alternatives to manual de-icing. Mechanical de-icing methods employ the use of mechanical force in the form of vibrations, actuators, pneumatics, and high-pressure water jets [10]. Thermal energy can be applied to raise the temperature of a surface above the freezing point to prevent ice accretion, or sufficient heat can be applied to melt ice directly. Thermal anti-icing is an energy-intensive process since sufficient heat must be provided to prevent the release of latent heat from water which would cause it to freeze. Less thermal energy is required for de-icing since ice can be released from a surface if the ice is melted at the ice-solid interface [10]. Thermal anti-icing and de-icing methods include electrothermal heating [13], hot fluids (i.e. air, water, steam), and infrared heating [14].

Figure 6: Electrical heat tracing installed on handrails and stairs on a marine vessel [13].

Electrothermal heating is frequently used for anti-icing/de-icing on marine vessels and structures in the form of heating cables or electrical heat tracing (EHT) [10]. As shown in Figure 6, EHT can be installed on a variety of ship structures such as decks, gangways, stairs, superstructures, railings, and process equipment [13]. The minimum power requirements for conventional EHT are 300 W/m^2 for open deck areas, 200 W/m^2 for superstructures, and 50 W/m for railings [13]. Despite

the high energy consumption, EHT is widely used for ice protection in marine applications due to its controllability, high reliability, and versatility.

Chemicals are widely used to prevent ice accretion on roadways and aircraft, and as antifreeze agents in industrial systems. Chemical de-icers function by lowering the freezing point of the resulting water-chemical solution or by undergoing an exothermic reaction with water. De-icing chemicals can largely be broken down into three categories: chlorides, acetates, and alcohols. The most widely used chloride-based de-icing chemicals include sodium chloride, calcium chloride, magnesium chloride, and potassium chloride [10, 15]. Chlorides are inexpensive and widely available, however, they have limited use on marine structures due to their high corrosivity. The effectiveness of chlorides is diminished at low temperatures, for example, sodium chloride loses its effectiveness at temperatures lower than -10°C [10]. Acetate-based de-icing chemicals include calcium magnesium acetate, potassium acetate, and sodium acetate [10, 15]. Acetates generally have lower corrosivity and lower working temperatures than chlorides. However, acetates are more expensive than chlorides and can be harmful to the marine environment in large volumes [10]. Propylene glycol is an alcohol-based de-icing chemical that is the base of most aircraft de-icing fluids. Propylene glycol is fast-acting, non-corrosive, and can remain effective at temperatures as low as -48°C. However, propylene glycol has high biological oxygen demand and is toxic to the marine environment [10]. In addition, propylene glycol can leave behind slippery residue on surfaces, potentially causing workers to fall if applied to walking surfaces [15]. Generally, chemical de-icing techniques are considered impractical for marine applications because of corrosion, the difficulty of controlled application, and the negative environmental impacts of various chemicals [10, 9, 16].

The development of icephobic coatings is one of the most active areas of ongoing anti-icing/de-icing research [10]. Icephobic materials are defined by their ability to passively prevent freezing of condensation and incoming water droplets on the surface, while also reducing the adhesion between the ice and the solid to facilitate removal [17]. Ideally, an icephobic coating would be able to reliably prevent icing on its surface under all environmental conditions without external energy. However, this has proven to be challenging, since no coating that has been developed to date has achieved this feat. Furthermore, practical factors such as durability/longevity, cost-effectiveness, and ease of application have limited the widespread use of icephobic coatings. Icephobic coatings include low surface energy materials [18], air-isolating surfaces, oil-isolating surfaces [19], and phase change material-embedded coatings [20]. Superhydrophobicity is closely related to icephobicity. Superhydrophobic coatings combine the effects of low surface energy materials and high surface roughness to create air-isolating surfaces. Air-isolating surfaces trap pockets of air in the rough surface morphology to minimize contact between the liquid droplet and the solid surface. Superhydrophobic coatings have been shown to effectively reduce the rate of ice accretion and also the ice adhesion strength. Similarly, oil-isolating surfaces are created by infusing a nanostructured surface with a water-immiscible liquid lubricant, resulting in a thin and smooth layer of water-repelling lubricant being maintained on the surface [19]. The presence of the lubricant layer results in extremely low ice adhesion strength due to the smooth liquid-liquid interface which has fewer defects and pinning points than the liquid-solid interface of air-isolating surfaces [21].

2.3 Wetting Theory and Models

Wettability is defined as the ability of a solid surface to allow a liquid to spread over its surface and is quantified by the contact angle (CA) between the liquid droplet and the underlying solid

surface. As illustrated in Figure 7, a surface is considered hydrophilic for water CA < 90°, hydrophobic if 90 < CA < 150°, and superhydrophobic for CA > 150°.

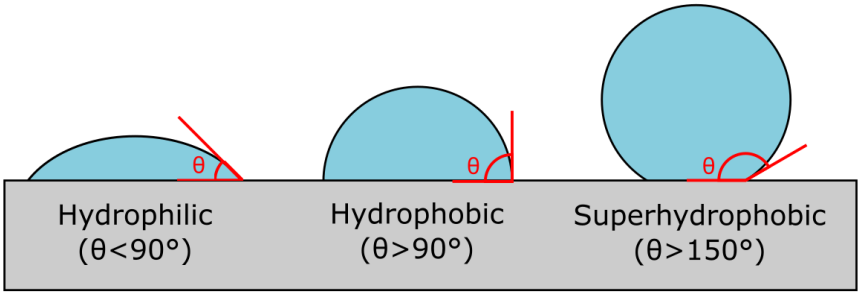

Figure 7: Illustration of the wetting behaviour on hydrophilic, hydrophobic, and superhydrophobic surfaces.

The contact angle of a liquid droplet on a smooth, homogenous solid surface is determined by Young's equation, Equation (1). Three interfaces exist for a liquid droplet on a solid surface under atmospheric conditions: solid-liquid, liquid-air, and solid-air. The contact angle, θ, that forms at the three-phase contact line depends on the relative interfacial energies of the solid-liquid (γ_{SL}), liquid-air (γ_{LA}), and solid-air (γ_{SA}) interfaces [22].

$$cos\theta = \frac{\gamma_{SA} - \gamma_{SL}}{\gamma_{LA}} \tag{1}$$

Young's equation is limited for application to real solid surfaces since they are not ideally smooth nor homogenous. To address this limitation, the Wenzel and Cassie-Baxter models were developed to describe the wetting behaviour of rough surfaces. The Wenzel model assumes a rough, homogenous surface and that there is complete penetration of the liquid into the cavities in the rough surface. To account for the increase in the area of the solid-liquid interface caused by roughness, Wenzel defined a roughness factor, r, as the ratio of a surface's actual area to its projected geometric area [22]. The Wenzel contact angle, θ_W, of a liquid droplet on a solid surface in the Wenzel state is determined by Equation (2). The Wenzel model demonstrates that surface

roughness amplifies the underlying wetting behaviour of a surface. If a surface is inherently hydrophobic, then increasing surface roughness will also cause the contact angle to increase. Conversely, if a surface is hydrophilic, then increasing surface roughness will decrease the contact angle. In the Wenzel state, droplets on a surface will typically display high adhesion and will not slide easily.

$$cos\theta_W = rcos\theta \tag{2}$$

Unlike the Wenzel model, the Cassie-Baxter model assumes that there is no penetration of liquid into the cavities of the rough surface. The Cassie-Baxter model assumes that the droplet sits on a smooth, heterogeneous surface composed of solid and air. Each phase is characterized by its own contact angle and fractional area [22]. For the case of a superhydrophobic material, the Cassie-Baxter model can be simplified by letting $f_1 = f$ and $f_2 = 1 - f$, where f is the contact area of the solid protrusions and $f - 1$ is the contact area of the air pockets. The Cassie-Baxter contact angle, θ_{CB}, is then calculated using Equation (3). The Cassie-Baxter model shows that the contact angle will increase regardless of the underlying wetting behaviour of the surface, provided that the fractional area of air is over a certain threshold. In the Cassie-Baxter state, droplets on a surface will typically have very low adhesion and slide easily. Therefore, superhydrophobic surfaces are designed with hierarchical micro and nanoscale features to amplify roughness which allows a high fraction of air to become trapped in the surface structure.

$$cos\theta_{CB} = fcos\theta + f - 1 \tag{3}$$

The Wenzel and Cassie-Baxter models represent the limit cases of wetting behaviour when there is either complete or zero penetration of liquid into the surface cavities. The Wenzel and Cassie-Baxter equations can be combined to more accurately describe real scenarios where there is only

partial penetration of liquid in the surface cavities. Equation (4) is used to obtain the mixed model contact angle, θ_M, on a rough heterogeneous surface with partial liquid penetration. The mixed model demonstrates that for inherently hydrophobic surfaces, increasing the surface roughness will always cause the contact angle to increase. For hydrophilic surfaces, the contact angle will also increase with increasing roughness if there is a high fraction of air pockets. However, if the roughness is reduced such that fraction of air pockets falls below a critical value, a transition to the Wenzel state will occur, after which the contact angle will decrease with increasing roughness.

$$cos\ \theta_M = rfcos\theta + f - 1 \tag{4}$$

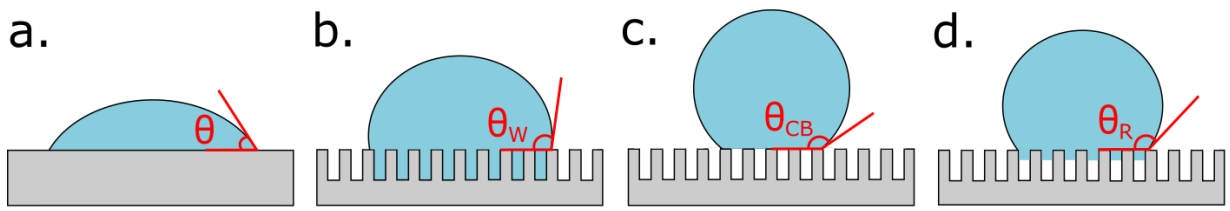

Figure 8: Illustration of the wetting states assumed by each of the theoretical models: (a) Young state, (b) Wenzel state, (c) Cassie-Baxter state, (d) Mixed state.

In addition to the static contact angle, the contact angle hysteresis (CAH) is required to fully characterize the wetting behaviour of a surface. CAH is defined as the difference between the advancing contact angle (θ_A) and receding contact angle (θ_R), and is calculated by Equation (5).

$$CAH = \theta_A - \theta_R \tag{5}$$

The advancing and receding contact angles are the maximum and minimum metastable contact angles respectively, as a liquid droplet wets or unwets a solid surface. CAH is caused by droplet pinning at the three-phase contact line due to roughness or chemical heterogeneities on the solid surface [23]. Therefore, the CAH indicates the extent of the interaction that occurs at the liquid-solid interface and is a measure of the adhesion of the droplet to the solid surface [22]. When the

CAH is high, droplets will tend to stick to the solid surface and thus will have a high sliding angle (SA). Higher CAH values are typically observed in the Wenzel state because a greater area of solid surface must be wet and unwet as the liquid fills into the surface protrusions as the droplet slides across the rough surface. When the CAH is very low, the surface will appear slippery and droplets will begin to slide at very low SA. Low CAH suggests that the droplet is in the Cassie-Baxter state because the droplet glides across the top of the composite surface, only contacting the tips of the solid protrusions [22]. As illustrated in Figure 9, the advancing and receding contact angles can be measured in two scenarios; from a droplet sliding on an inclined surface, or by adding liquid to and removing liquid from a sessile droplet on a horizontal surface [22].

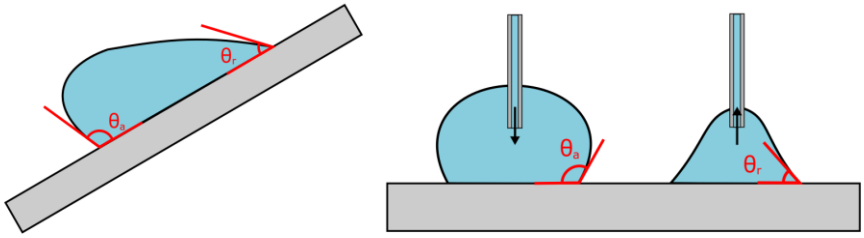

Figure 9: Advancing and receding contact angles can be measured from a droplet sliding on an inclined surface or by adding/removing liquid from a sessile drop.

2.4 Superhydrophobic Coatings

Superhydrophobic materials are characterized by a CA exceeding 150° and CAH less than 10°. Inspired by natural materials such as plant leaves, insect wings, and waterfowl feathers, superhydrophobic materials have garnered great research interest in recent decades. Technological advancements in scanning electron microscopy (SEM) allowed researchers to examine these natural materials to further study the mechanism behind the phenomenon of superhydrophobicity [24]. Two critical factors are responsible for superhydrophobicity; surface roughness and chemical composition [21]. Synthetic superhydrophobic surfaces have been developed which mimic this

non-wetting behaviour and have found promising uses in anti-icing/de-icing, self-cleaning, anti-corrosion, and drag reduction applications.

Superhydrophobic surfaces can be fabricated by three distinct methods: 1) by roughening an intrinsically hydrophobic surface; 2) by roughening a surface that is not intrinsically hydrophobic, followed by deposition of a hydrophobic material; and 3) by depositing a hydrophobic material that has a rough surface texture. The third method is of greatest interest for practical applications since it is independent of the chemical composition of the substrate and does not necessitate damaging the substrate by roughening or texturing. The rough geometry and hydrophobic surface chemistry necessary for superhydrophobicity can be produced in a convenient single-step coating process.

Superhydrophobic coatings can be applied by conventional coating methods such as brushing/spreading, dip-coating, spin coating, or spray-coating. Brushing or spreading methods are the simplest processes that can be used to quickly apply a superhydrophobic coating to a surface. These manual methods are imprecise, making it challenging to produce homogenous coatings of uniform thickness. Dip-coating is a straightforward coating process that offers good control over the film thickness. One of the drawbacks of dip-coating is that a large volume of solution is required such that the substrate can be fully immersed, which can lead to wastage if samples are fabricated in small batches. Dip-coating also coats all sides of the substrate, which may not be desirable in all situations. Spin-coating is a simple coating method which can reliably produce uniform films of specified thickness. The major drawbacks of the spin coating process are that it is limited to small, flat substrates which restricts its use to laboratory settings. Spray-coating is a simple, yet highly versatile and practical coating application method. The spray-coating method can be used to quickly coat large areas and components with complex geometry. Most

coatings and paints can be applied by spraying provided that the viscosity of the solution is appropriate. Spray-coating typically creates a higher quality surface finish than brushing or dip-coating, but the control over the layer thickness is not as precise as spin-coating. The main drawbacks of spray coating are the relatively weak adhesion to substrates and the difficulty in controlling the surface morphology and nanostructure [24]. The coating adhesion can be improved by roughening the substrate by sandblasting or by application of a primer or adhesion-promoting compound. Adjusting the spraying parameters such as the nozzle diameter, air pressure, flow rate, and spray time can give some control over the surface morphology but still not to the degree of more advanced fabrication methods [22]. Advanced superhydrophobic surface fabrication techniques include electrodeposition, sol-gel methods, chemical vapour deposition, lithography, and electrospinning [24, 22, 21, 25]. These advanced methods typically enable the use of novel materials or produce unique nanostructured surfaces that cannot be achieved by conventional coating methods. These methods are capable of creating very high-quality coatings, but specialized equipment and facilities are required for the fabrication processes.

Superhydrophobic coatings often consist of multiple components to create a composite coating with the beneficial properties of each material. Inorganic nanomaterials are used as aggregates to create rough micro-nanostructures. The aggregates are often dispersed in a polymer matrix, which binds them together and adheres them to the substrate [26]. Low surface energy polymers such as polydimethylsiloxane (PDMS) [27], polyurethane (PU) [28], and polystyrene (PS) [29] are all frequently used as matrix materials. Common aggregate nanomaterials are listed in Table 1, including silica (SiO_2), metals and metal oxides, carbon, and polymer materials.

Table 1: Summary of common aggregate materials used to fabricate superhydrophobic coatings.

Category	Material	Ref.
Silica	Silica (SiO_2)	[27, 30, 29, 31, 31, 32]
Metals and metal oxides	Titanium Oxide (TiO_2)	[26, 33]
	Zinc Oxide (ZnO)	[34, 35]
	Aluminum oxide (Al_2O_3)	[36]
	Cobalt (Co)	[37]
	Nickel (Ni)	[38]
Carbon	Graphene	[39]
	Carbon Nanotubes (CNTs)	[40, 41]
Polymers	Polytetrafluoroethylene (PTFE)	[42]
	Polyvinylidene Fluoride (PVDF)	[43]

SiO_2-based superhydrophobic coatings are the most common because SiO_2 nanoparticles are widely available, inexpensive, and possess desirable chemical and mechanical properties [21, 44]. SiO_2-based coatings have been shown to possess good durability, thermal stability, and corrosion resistance [27, 29]. SiO_2-based coatings can be applied to almost any substrate material including metals [27, 45, 31], glass [28, 30], plastics [31], and textiles [46] using simple conventional coating methods such as spray-coating [30, 28], spin-coating [26], and dip-coating [46, 29]. Xie et al. demonstrated a simple method of preparing a SiO_2/PDMS-based superhydrophobic coating on magnesium alloy substrates [27]. This simple preparation process is illustrated in Figure 10. SiO_2 nanoparticles (40nm - 250nm) were hydrophobically modified by adding them to a solution of triethoxy-1H,1H,2H,2H-tridecafluoro-n-octylsilane (TTFOS/FAS-13) dissolved in ethanol. The mixture was dispersed by ultrasonic and mechanical stirring for several hours before PDMS and a curing agent were added to the solution. The solution was scraped onto the substrate and cured in an oven at 160°C for 5 minutes. The prepared coating demonstrated a maximum CA of 153.6° and SA less than 10°. Multiple sizes of SiO_2 nanoparticles were used to create the hierarchical micro-nanostructure consisting of SiO_2 agglomerations which maximized the surface roughness and thus

the contact angle. An SEM image of the surface morphology of the resulting coating is shown in Figure 10.

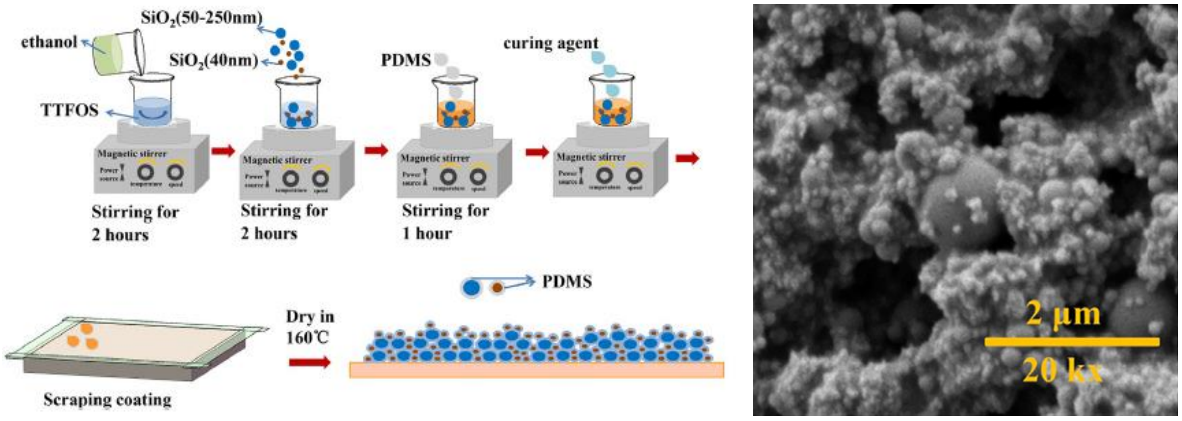

Figure 10: Example of a simple process used to prepare a PDMS/SiO_2-based superhydrophobic coating and SEM image of the surface morphology of the coating [27].

The anti-icing/de-icing properties of superhydrophobic coatings have been widely researched as a promising passive solution to the problems imposed by icing. Currently, there is no single material that can completely prevent ice accretion under all environmental conditions, however, superhydrophobic coatings can effectively delay icing or facilitate de-icing by one or more of the three distinct mechanisms illustrated in Figure 11 [47]. First, water droplets can roll off of inclined or vertical superhydrophobic surfaces before icing can occur due to the low adhesion between the droplet and solid surface. Second, icing is delayed for droplets in the Cassie-Baxter state due to the reduced heat transfer rate between the droplet and cold substrate. Finally, the ice adhesion strength on superhydrophobic surfaces is reduced due to the small interfacial contact area [47].

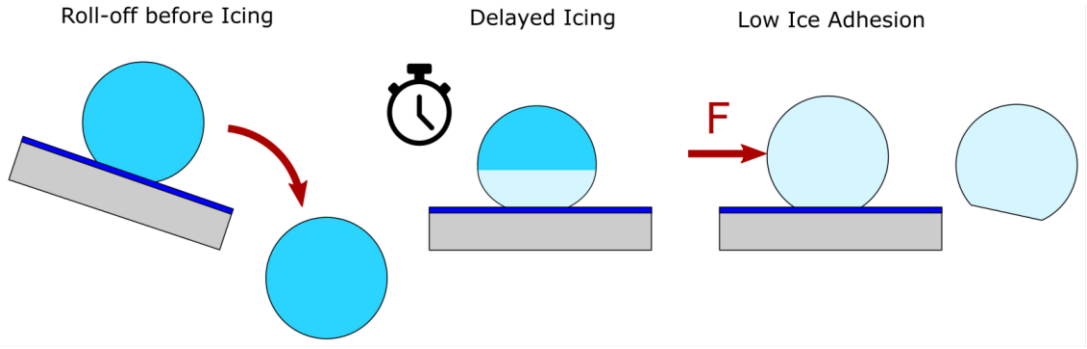

Figure 11: Illustration of the three mechanisms by which superhydrophobic surfaces can mitigate icing.

Researchers have observed that water droplets can take much longer to freeze on superhydrophobic surfaces than on an uncoated surface at the same temperature. Superhydrophobic coatings reduce the heat transfer rate between the water droplet and the substrate, which can delay the onset of freezing by a few seconds to over thirty minutes [31, 48, 32, 35]. The presence of interfacial air pockets, characteristic of the Cassie-Baxter state, are primarily responsible for the high thermal resistance of superhydrophobic coatings. Miljkovic et al. found that the enhanced thermal resistance of a nanostructured superhydrophobic coating reduced heat flux by 71% compared to a flat hydrophobic surface [49]. As illustrated in Figure 12, the air pockets reduce the contact area between the droplet and the solid surface. The thermal resistance at the interface can be modelled by considering two parallel conduction pathways. One path represents the thermal resistance of the air pockets, while the other represents the solid pillars. For droplets in the Cassie-Baxter state, the solid contact area fraction, f, is often very low ($f < 0.1$) and therefore limits the heat that can be transferred by direct conduction through the pillars [49]. Therefore, the air that comprises the majority of the interfacial area provides an effective layer of insulation that inhibits the heat transfer process. Moreover, the overall heat transfer rate is reduced further by the low thermal conductivity of the coating materials, such as SiO_2 and various hydrophobic polymers, which are poor conductors of heat. The smaller contact area due to the sphere-like shape of the droplet also contributes to a reduction in the overall heat transfer rate.

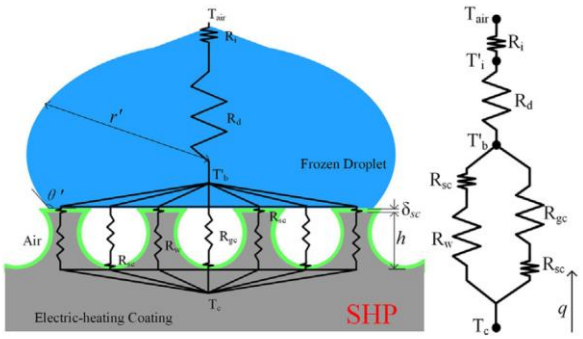

Figure 12: Thermal resistance diagram illustrating the heat transfer process between a frozen droplet and the superhydrophobic surface [8].

Liu et al. investigated the effect of increased thermal resistance on the icing and de-icing processes [8]. They found that the de-icing time was longer for the superhydrophobic coating than for an equivalent oil-infused porous surface when heating the substrate. Since the thermal conductivity of the silicone oil was an order of magnitude greater than that of air, the oil-infused surface had greater heat transfer efficiency and thus a faster de-icing time. These results demonstrate that the thermal barrier created by the air film can be detrimental to de-icing performance, where efficient heat transfer from the surface to the ice is necessary. Therefore, the insulative properties of superhydrophobic coatings generally allow them to be better suited to anti-icing than de-icing.

Surfaces with low ice adhesion strength allow ice to be more easily removed by small external forces such as wind or vibration [47]. Three physical mechanisms are responsible for the adhesion of ice to surfaces: chemical adhesion, thermodynamic adhesion, and mechanical adhesion. Chemical adhesion includes the contributions of covalent and electrostatic forces, thermodynamic adhesion involves van der Waals forces and hydrogen bonding, and mechanical adhesion is caused by interlocking with surface roughness [50]. The adhesion strength of ice can be estimated using the work of adhesion, which is defined as the free energy required to separate the ice from the solid surface [51]. For a liquid droplet on a solid surface, the work of adhesion (w_A) is a function of

surface tension (γ_{LA}) and the contact angle (θ). The theoretical work of adhesion is calculated by the Young-Dupre equation, Equation (6).

$$w_A = \gamma_{LA}(1 + cos\theta) \tag{6}$$

The Young-Dupre equation shows that the theoretical work of adhesion will decrease as the contact angle increases due to the reduction in interfacial area. However, the results given by the Young-Dupre equation do not align well with experimental studies of ice adhesion strength. Therefore, the work of adhesion is generally not regarded as a suitable parameter to estimate ice adhesion characteristics [50]. In practice, it is difficult to characterize and predict the ice adhesion strength over a variety of different surfaces due to the number of uncertainties and sensitivities to internal and external factors. Ice adhesion is affected by the temperature, ice type, test arrangement, and properties of the substrate including its chemical composition, surface morphology, stiffness, and thermal expansion coefficient. Consequently, the ice adhesion strength is most often measured experimentally through tensile or shear testing [52]. The shear ice adhesion strength, τ, is defined as the maximum force (F_{max}) required to separate ice from the substrate divided by the interfacial area of the ice (A_c) and is calculated by Equation (7) [51, 52]. Typically ice adhesion strength can range from about 10 kPa to 1 MPa, depending on the properties of the ice, surface, and testing conditions [51]. Materials possessing an ice adhesion strength of less than 100 kPa can be considered icephobic [53].

$$\tau = \frac{F_{max}}{A_c} \tag{7}$$

Researchers have investigated superhydrophobic coatings with a variety of compositions for anti-icing applications. Lei et al. developed a SiO_2/PDMS coating which was applied to glass substrates by spray-coating to achieve a maximum CA of 165.5° [54]. Icing tests were performed where the

sample was inclined at an angle of 15° and water droplets continually impinged on the sample for 30 minutes in freezing conditions. The coating was completely effective at preventing ice from forming on the surface at temperatures as low as -8°C and remained partially effective at -12°C due to droplets rolling off before freezing. At temperatures below -16°C, ice rapidly accumulated on the surface due to frost formation which increased wettability and prevented droplet roll-off. Liu et al. demonstrated that a SiO_2/PU coating could significantly delay icing [31]. The prepared coating was spray-coated onto an aluminum substrate and had a CA of 160°. When tested at a temperature of -10°C, the freezing time was found to increase from 5 minutes on bare aluminum to 37 minutes on the coated surface [31]. Similarly, Yang et al. showed that a ZnO/PDMS coating could delay icing by 23 minutes on a horizontal surface at -10°C due to the reduced solid-liquid contact area and low thermal conductivity of the coating [35]. Liu et al. investigated the reduction in the ice adhesion strength on a SiO_2/PDMS superhydrophobic coating applied to an aluminum substrate [55]. Ice adhesion tests were performed using a centrifuge method at a temperature of -5°C. An ice adhesion strength of 20 kPa was measured on the SiO_2/PDMS surface, compared to 155 kPa on the untreated aluminum substrate. The anti-icing properties of superhydrophobic coatings have been widely reported by other researchers, which are summarized in Table 2.

Table 2: Summary of properties of various superhydrophobic anti-icing coatings on metallic substrates.

Aggregate	Matrix	Substrate	Methods	Contact Angle [°]	Ice Adhesion Strength [kPa]	Ambient Temperature [°C]	Icing Delay [s]	Ref.
PTFE	PDMS	Aluminum	Spin Coating	163.6	-	- 3.6	~ 50	[42]
ZnO	PDMS	Aluminum	Drop-casting	159.5	-	- 10	1380	[35]
SiO_2	PU	Aluminum	Spraying	160	-	- 10	1920	[31]
SiO_2	PDMS	Aluminum	Brushing	157	155 / 20	- 10	10.6	[55]
SiO_2	PS	Aluminum	Spin Coating	163	~ 150 / 25	- 10	265	[32]
-	CNT/PDMS	Kanthal	Laser Etching	152.7	385 / 90	- 20	~ 260	[48]

Superhydrophobic coatings have several limitations in anti-icing applications. Superhydrophobic coatings gradually deteriorate when subjected to repeated freeze/thaw cycles due to the expansion of water as it freezes causing damage to the delicate surface structures. Ruan et al. [42] showed that the CA on a PTFE/PDMS-coated aluminum surface decreased from 163.6° to 140° after being subjected to 34 icing/de-icing cycles. When droplets impact the surface at high velocity, air can be pressed out of the rough surface causing a transition to the Wenzel state. This results in a significant increase in ice adhesion due to mechanical interlocking with the surface microstructure. Similarly, condensation or frost formation on superhydrophobic surfaces can drastically diminish their effectiveness [47].

2.5 Electrothermal Heating Films

Electrothermal heating systems can be used for anti-icing by continuously generating heat to maintain a sufficiently high surface temperature to prevent ice accretion. Alternatively, these systems may also be used for de-icing by intermittently generating heat to melt accumulated ice. Each of these mechanisms is illustrated in Figure 13. In recent years there has been considerable research into electrothermal heating systems in the form of electrically conductive films, coatings, and textiles. These systems are attractive for anti-icing/de-icing because of their high heat transfer efficiency and improved energy efficiency when compared to conventional resistance heating methods. Various conductive materials have been investigated as heating elements including silver [56, 57], copper [58], graphene [59], and carbon nanotubes [60]. The application of electric heating films to a metallic or conductive substrate presents an additional challenge due to the requirement for electrical insulation to prevent short-circuiting between the heating element and substrate. Electrical shorting can be mitigated by separating the heating element from the substrate using layers of glass fibers [58, 61] or thin polymer films [61].

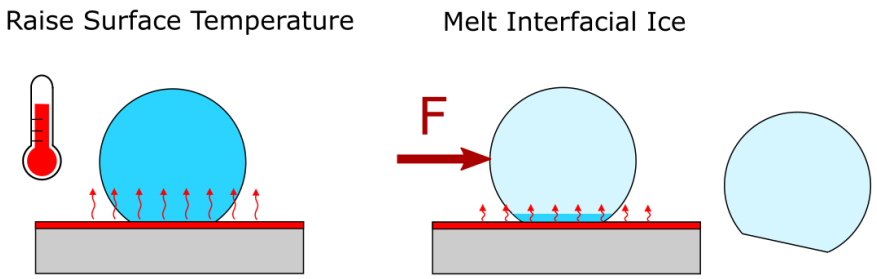

Figure 13: Illustration of the mechanisms by which electrothermal heating can mitigate icing. Icing can be prevented by raising the surface temperature above the freezing point. Alternatively, ice can be easily removed after melting the interfacial ice layer.

Joule heating occurs when a voltage difference is applied across a conductive material and the electrical energy is converted into heat. Joule heating converts 100% of the electrical energy into heat, therefore the heating power, P_{el}, can be calculated as a function of the electric current (I) and resistance (R), as shown by Equation (8). Electro-conductive films are typically designed with very low resistance to maximize their heat generation potential.

$$P_{el} = I^2 R \tag{8}$$

The resistance of the heating element is temperature-dependent according to Equation (9). The resistance at the heater temperature, T, is determined based on the resistance, R_o, at the reference temperature, T_o. The temperature coefficient of resistance, α, is positive for most conductive materials such as silver and copper, therefore the resistance of the heating element will typically increase as the temperature increases.

$$R = R_o(1 + \alpha(T - T_o)) \tag{9}$$

Sheet resistance (R_s) is an electrical property that is essential to characterize conductive films of uniform thickness. The sheet resistance of a film quantifies its lateral resistance per square area and is expressed in units of Ω/sq. The four-point probe method is the most common method used to measure sheet resistance, however, if the resistivity (ρ) and film thickness (t_f) of the conductive material are known the sheet resistance can be easily calculated using Equation (10) [62].

$$R_s = \frac{\rho}{t_f} \tag{10}$$

The temperature of the heater is determined by the energy balance, Equation (11), between the inflow of electrical energy and the rate that heat is lost to the surroundings due to conduction ($\dot{Q}_{cond}$), convection ($\dot{Q}_{conv}$), and radiation heat transfer ($\dot{Q}_{rad}$). A detailed analysis of the heating and cooling processes is carried out in Section 4.4.

$$\dot{Q}_{net} = P_{el} - \dot{Q}_{cond} - \dot{Q}_{conv} - \dot{Q}_{rad} \tag{11}$$

Thermal response time, maximum temperature rise, and surface power density are critical performance indicators of conductive film heaters. A fast thermal response time allows for rapid de-icing by concentrating heating power at the ice-solid interface and minimizing wasteful heat loss to the surroundings. Petrenko et al. (2011) demonstrated that the energy consumption for de-icing could be reduced further by applying heat in short pulses to minimize the thermal penetration depth into the ice. Pulse heating limits the thermal penetration depth into the ice such that only the ice-solid interface is melted and the heat loss into the ice is minimized. Once the interface is melted, the film of melted liquid water at the interface acts as a lubricant which allows the remaining ice to easily slide off the surface. Consequently, electrothermal pulse heating is highly efficient and requires only a fraction of the energy of conventional electric heating techniques [57].

Surface power density, P_d, is a measure of the power output per unit of coated surface area, A, (neglecting the area covered by the electrodes) and is calculated by Equation (12).

$$P_d = \frac{P_{el}}{A} \tag{12}$$

The surface power density is useful to quantify the power required for anti-icing/de-icing independent of the size of the target surface. Values of power density for anti-icing/de-icing

typically range from 0.3 W/cm^2 to 1.6 W/cm^2 depending on the substrate material and thickness, and test conditions such as the rate of icing and ambient temperature [5, 57, 60, 61]. The electrothermal properties of various electro-conducive films, coatings, and textiles from the literature are listed in Table 3.

Table 3: Electrothermal properties of various electro-conductive films and coatings.

Material	Method	Thickness [μm]	Sheet Resistance [Ω/sq]	Voltage [V]	ΔT_{max} [°C]	Heating Rate [°C/s]	Power Density [W/cm^2]	Ref.
Ag Nanowires	Doctor-blading	< 1	3 – 4	3 – 6	100	1.0	0.27	[56]
Ag Alloy	Sputtering	-	-	200	30	0.6	1.4 - 1.6	[57]
Cu-Mn Alloy	Thermal Spraying	100	7 – 9	-	135	4.5	3	[58]
Aligned CNTs	CVD	6 – 24	21 – 76	16	140	2.6	0.49	[60]
CNTRENE^{TM}	Spin-coating	-	-	120	70	0.85	0.24	[63]
Graphene	Scraping	194	-	750	40	0.2	0.15	[59]
Carbonized Textile	Lamination	268	70	6.7 - 9.2	35	0.1	1.2	[61]

The anti-icing/de-icing performance of various heating films has been investigated through laboratory testing by many other researchers. Falzon et al. (2015) demonstrated the anti-icing ability of a carbon-based electro-conductive textile. Anti-icing tests in a cold chamber at -20°C demonstrated that there was no icing of the textile surface after one hour while the film was supplied with a power density of 0.838 W/cm^2 [61]. Yao et al. (2018) developed a heating film composed of stacked CNT web layers capable of rapid de-icing. At an environmental temperature of -12°C, a 3 mm-thick layer of ice was removed from the film in under 15 seconds with a power density of 0.49 W/cm^2 [60].

2.6 Hybrid Superhydrophobic - Electrothermal Coatings

In many cases, one method alone is insufficient for adequate icing protection. Hybrid techniques combine elements of one or more passive or active techniques and have been demonstrated to be a more effective solution to the challenges posed by icing [64]. Superhydrophobic coatings can

delay ice accretion and reduce ice adhesion but they cannot completely prevent icing over a prolonged time period. The durability of many superhydrophobic coatings is also limited when subjected to harsh environmental conditions, further limiting their longevity for anti-icing. Electrothermal heating coatings are a more reliable ice protection technique for harsh environments, however, they can be highly energy-intensive. Robust and efficient anti-icing/de-icing can be achieved by applying a superhydrophobic coating on the outer surface of an electrothermal heating film. Energy consumption for heating can be reduced, while the longevity of the superhydrophobic coating is increased. In addition, heating can mitigate the formation of condensation and frost on the superhydrophobic coating, improving the effectiveness in humid conditions.

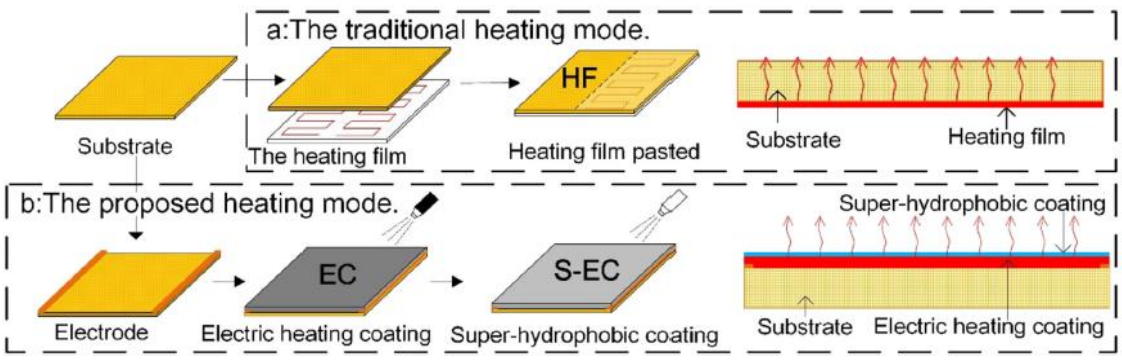

Figure 14: Fabrication process of the traditional heating film and the hybrid superhydrophobic - electrothermal coating [5].

Zhao et al. (2018) developed a novel hybrid anti-icing/de-icing coating which combined a polymer-MWCNT heating element with a SiO_2-based superhydrophobic top-coat [5]. The coating was applied by spray-coating onto a glass fiber reinforced polymer (GFRP) substrate. The fabrication process of the hybrid coating is illustrated in Figure 14. Icing tests were conducted on the electric heating coating (EC) and superhydrophobic electric heating coating (S-EC) samples inside a cold chamber at -43°C. The anti-icing tests showed that S-EC could be maintained ice-free with a lower power density of 0.41 W/cm^2, compared to the 0.56 W/cm^2 required for EC. The

lower power density corresponded to a 27% reduced energy consumption on S-EC compared to EC. The de-icing time was reduced from 118s on EC to 97s on S-EC when both samples had the same power density of 0.70 W/cm^2. The thin layer of liquid water created by the ice melting resulted in ultra-low adhesion forces, such that ice could be easily blown away by the wind for energy-efficient de-icing [5]. Peng et al. (2021) investigated the durability of a superhydrophobic electrothermal coating fabricated from modified graphene embedded in PDMS. The samples retained their superhydrophobicity after 25 de-icing cycles, demonstrating the ability of the hybrid coating system to mitigate damage from freeze/thaw cycling and increase superhydrophobic coating longevity [6]. The properties of several hybrid coatings reported in existing research are summarized in Table 4.

Table 4: Anti-icing/de-icing properties of hybrid superhydrophobic - electrothermal coatings. Values are compared before and after the application of a superhydrophobic coating to the heating films.

Materials	Substrate	Methods	Contact Angle [°]	Power Density [W/cm^2]	Ambient Temperature [°C]	De-icing Time [s]	Energy reduction [%]	Ref.
MWCNT / PU SiO_2	GFRP	Scraping Spraying	54 / 156	0.59 / 0.43	-25	49 / 34	27	[7]
MWCNT / PU SiO_2	GFRP	Spraying	100.9 / 162.3	0.75 / 0.65	-48	112.6 / 57.0	13	[8]
MWCNT / polymer SiO_2	GFRP	Spraying	87 / 160	0.56 / 0.41	-43	118 / 97	27	[5]
Graphene / PDMS	Glass	Mesh Screening	162	-	-5	115	-	[6]

2.7 Summary

This research aims to fabricate and characterize a hybrid anti-icing coating with superhydrophobic and electrothermal properties. A need has been identified for robust and efficient ice protection methods that will ensure the safety of vessels and structures operating in cold, harsh offshore environments. In this chapter, electrothermal methods were identified as one of the most versatile and reliable active ice protection methods despite their high energy usage. Numerous icephobic and superhydrophobic coatings have been developed by other researchers in an effort to achieve

passive ice protection. The electrothermal and superhydrophobic coating methods can be combined to create a hybrid ice protection solution with enhanced low-temperature performance and improved energy efficiency.

The materials, fabrication methods, and anti-icing performance of various superhydrophobic coatings and heating films presented by other researchers were reviewed. Existing research on hybrid superhydrophobic – electrothermal anti-icing coatings was also presented and evaluated to identify areas for further research and potential improvements. Despite the few existing studies of hybrid coatings, there is limited information on the direct application of such a coating to a conductive metal substrate. The anti-icing and de-icing performance of these coatings may also be investigated further under a wider range of environmental conditions. Many previous studies used advanced equipment and expensive materials to fabricate their samples. In this work, considering suitability for practical applications, the coating will be applied by a simple spray-coating process and inexpensive materials were selected for the development of the hybrid superhydrophobic – electrothermal anti-icing coating.

CHAPTER 3

Materials and Methods

3.1 Materials

3.1.1 Substrate

Precipitation hardened (PH) stainless steel (SS) is a widely used material in the marine and offshore petroleum industries. 17-4 PH SS is a martensitic precipitation-hardening stainless steel which derives its name from its composition containing approximately 17% chromium and 4% nickel. 17-4 PH SS is frequently used in the marine and oil and gas industries due to its attractive combination of high tensile strength, high toughness, and good corrosion resistance [65]. 1/8" thick, 12" x 12" sheets of cold worked 17-4 PH SS (McMaster-Carr) were used as the substrate material for this study. The as-received material was cut into several 50 mm x 50 mm samples using a band saw.

3.1.2 Electric Heating Film

The electric heating film has three components: the heating element, electrodes, and insulation. For application to the conductive metal substrate, the heating element must be insulated from the substrate to prevent short-circuiting. Fully insulating the heating element also prevents exposure of the energized conductor and protects the heating element from physical damage. Polydimethylsiloxane (PDMS) is a non-conductive silicone elastomer that is widely used as an encapsulant for electronic devices. Sylgard 182 (Dow Chemical Company) is a two-component kit that contains a vinyl-terminated PDMS polymer and a cross-linking curing agent. The PDMS base and curing agent are mixed in a 10:1 ratio and then heat-cured at 125°C for 30 minutes to form a strong and flexible transparent silicone elastomer. Sylgard 182 possesses high dielectric strength, is chemically inert, and has good thermal stability. Sylgard 182 can be easily applied by spray coating when its viscosity is reduced by dilution with hexane. Hexane has a high vapour

pressure which allows the majority of the diluent to evaporate in-flight, minimizing the amount of hexane that reaches the target surface during the spraying process [66].

The PDMS curing process is inhibited when there is contact between uncured PDMS and certain paints, adhesives, and epoxies. Curing inhibition occurs when the platinum-based catalyst contained within the PDMS curing agent is rendered inert after contamination by another material that reacts with the catalyst. This results in the PDMS having a sticky texture and appearance, and poor adhesion to the substrate. DOWSIL 92-023 primer (Dow Chemical Company) was used to mitigate curing inhibition when PDMS was applied over the metallic epoxy used for the conductor. DOWSIL P5200 adhesion promoter (Dow Chemical Company) was also used to improve the adhesion of the PDMS to the substrate and the superhydrophobic coating.

The electrodes provide a point of connection for power to be supplied to the heating element and help maintain an even heating distribution across the sample. Electrodes were made from lengths of copper foil (McMaster-Carr) 6.4 mm wide and 0.1 mm thick. The copper foil electrodes were pasted onto the sample using a two-part polymer adhesive (LePage).

The heating element can be fabricated using electrically conductive films, paints, or foils. Metallic paints are versatile, inexpensive, and can typically be applied using simple methods such as brushing, rolling, or spraying. 843ER Super Shield (MG Chemicals) is a two-part silver-coated copper epoxy conductive paint. The paint contains highly conductive silver-coated copper flakes which give the coating excellent electrical conductivity. The resin and hardener are mixed in a 100:28 ratio by weight. The paint is easily applied by spray-coating and can be rapidly heat-cured at 80°C for 2 hours. The cured Ag-Cu epoxy is durable, corrosion resistant, and has strong adhesion to low surface energy polymers [67].

3.1.3 Superhydrophobic Coating

The superhydrophobic coating is based on modified SiO_2 nanoparticles embedded in a matrix of PDMS. SiO_2 nanoparticles (US Research Nanomaterials Inc.) were selected as the aggregate material due to their favourable mechanical properties, simplicity, and low cost compared to other nanomaterials. To create the desired hierarchical micro-nanostructure, spherical SiO_2 nanoparticles of three different diameters (15-20nm, 60-70nm, and 200nm) were procured for the fabrication of the coating.

The SiO_2 nanoparticles were hydrophobically modified with triethoxy-1H,1H,2H,2H-tridecafluoro-n-octylsilane (TTFOS, Fisher Scientific Canada), also known as FAS-13. FAS-13 is a low surface energy fluorinated alkyl silane compound that is commonly used to modify the wetting behaviour of SiO_2 to become hydrophobic [27, 32, 68, 69, 70]. When FAS-13 is dispersed in ethanol, a hydrolysis reaction will occur which causes the ethyl groups on the FAS-13 molecule to be replaced with hydroxyl groups to form a fluorosilane hydroxyl polymer. When the SiO_2 nanoparticles are added to the solution, polymerization occurs and the fluorosilane hydroxyl polymer reacts with the hydroxyl groups present on the surface of the SiO_2. This reaction bonds perfluorinated groups to the surface of the SiO_2 nanoparticles. The perfluorinated groups are non-polar and cause a significant reduction in surface energy resulting in hydrophobic SiO_2 nanoparticles [27].

PDMS (Sylgard 182) was also used as the adhesive constituting the matrix of the superhydrophobic coating. In addition to its aforementioned favorable electrical properties, Sylgard 182 also possesses low surface energy, good durability, and strong adherence. Furthermore, a strong bond is easily formed between the PDMS adhesive and the SiO_2 aggregate

material [27]. The use of Sylgard silicone elastomers has been widely reported in the fabrication of superhydrophobic SiO_2/PDMS-based coatings [71, 27, 43, 72, 73].

3.2 Coating Methods

The base metal substrate was sandblasted with 100 μm aluminum oxide abrasive particles to improve the adhesion of subsequent coatings. A Vaniman Problast – 80008 micro-abrasive sandblaster, as shown in Figure 15a, was used to prepare the samples. A nozzle standoff distance of approximately 5 cm was maintained while making a series of vertical, horizontal, and diagonal passes in each direction to create consistent roughness across the entire surface of each sample.

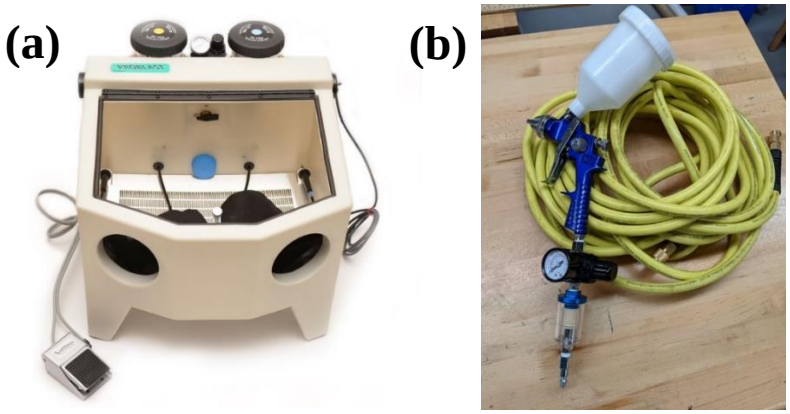

Figure 15: (a) Vaniman Problast - 80008 micro-abrasive sandblaster [74]. (b) HVLP spray coating gun with in-line air filter and pressure regulator.

All layers of the coating were applied using a simple manual spray-coating method. The high-volume low-pressure (HVLP) gravity-feed spray gun with a 1.4 mm nozzle, pictured in Figure 15b, was used throughout the fabrication process. The air pressure was set at 20 psi and a standoff distance was maintained at approximately 30 cm while spraying. The number of passes over the surface varied depending on the viscosity of the sprayed material and the target dry-film thickness of each layer.

3.3 Experimental Procedures

3.3.1 Surface Wettability Measurement

The static and dynamic contact angles of deionized water on the sample surfaces were measured using the optical-based contact angle measurement system (Dataphysics OCA 15EC) shown in Figure 16. The system consists of an adjustable sample stage, dosing system, and optics system. Dataphysics SCA 20 software was used to receive the live video feed, adjust the dosing parameters, and analyze the droplet to calculate the contact angle [75].

Figure 16: Dataphysics OCA 15EC Contact Angle Measurement System.

The wettability of a surface is quantified by the static contact angle, which is most commonly measured using the sessile drop technique [23]. To measure the static contact angle, the sample was first placed on the levelled stage. The syringe was then lowered until the tip of the needle was positioned about 1mm above the sample surface. A 20 μL water droplet was then dispensed at a rate of 5 μL/s. The needle was slowly retracted upwards once the droplet had settled, leaving the droplet pinned on the sample surface. The focus of the camera was manually tuned until a clear image of the droplet was obtained. The SCA 20 software was used to identify the baseline at the liquid-solid interface, then automatically detect the droplet contour using a polynomial fitting model. The static contact angle was calculated as the average of the left and right contact angles.

The dynamic contact angles are necessary measurements to determine contact angle hysteresis. The advancing contact angle (ACA) and receding contact angle (RCA) were measured by adding and removing liquid from a sessile droplet on a horizontal surface. The SCA 20 software was configured to add liquid to, then remove liquid from the drop over a specified time interval. The contact angle was dynamically tracked and recorded by the software throughout the process as the droplet volume changed.

To measure the ACA and RCA, the syringe was lowered until the tip of the needle was about 1mm above the sample surface and a 5 μL water droplet was dispensed on the surface at 2 μL/s. With the needle still in the droplet, 10 μL was added at 2 μL/s to obtain the ACA. Following a 5-second delay, 10 μL was removed at 2 μL/s to obtain the RCA. The CAH was calculated as the difference between the ACA and RCA. The static and dynamic contact angles were each measured at five distinct points on every sample. The results were averaged to account for any irregularities in the surface structure or composition.

3.3.2 Microstructure Characterization

The surface topology of the fabricated samples was examined using the FEI MLA 650F scanning electron microscope (SEM) shown in Figure 17. The SEM images were analyzed to characterize the microstructure, optimize the fabrication process, and investigate the coating's durability. Secondary electron imaging (SEI) was used to characterize the topography of the as-received, sandblasted, and coated samples. Low-energy secondary electrons are emitted from within a few nanometers of the surface of the sample as a result of inelastic interactions with incident electrons from the electron beam. The SEI image depends on the number of ejected secondary electrons that are detected by the SEM's Everhart-Thornley detector (ETD). Sharp features and edges have larger interaction volumes than flat surfaces and thus emit more secondary electrons and appear brighter

in the image. This results in well-defined topographical images of the surface that were captured at a magnification of 150 to 5000 times.

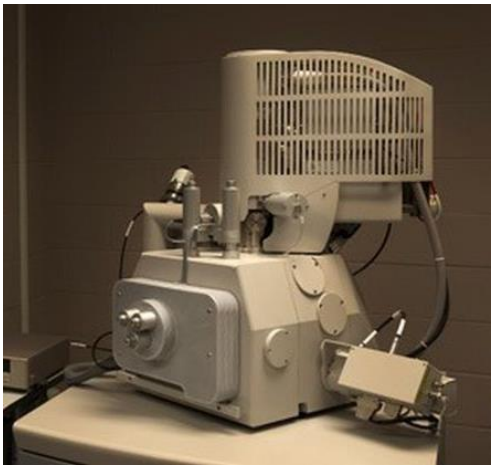

Figure 17: FEI MLA 650F Scanning Electron Microscope [76].

Backscattered electron (BSE) mode was used while imaging the cross-section of the sample to visually distinguish each layer of the coating. When the electron beam hits the sample surface, the trajectories of the incident electrons are altered by interaction with the atomic nuclei of the sample material. The high-energy incident electrons that are elastically scattered back from the sample are detected by the SEM's circular backscatter (CBS) detector. The resulting BSE image depends on the atomic number of the sample material, with higher atomic number materials yielding more backscattered electrons. BSE mode results in heavier materials appearing brighter in the image, therefore the substrate and metallic layers appear lighter while the polymeric layers appear darker.

3.3.3 Coating Thickness Measurement

The dry-film thickness of the coating was verified using an Elcometer 456 coating thickness gauge, shown in Figure 18 (a). Calibration of the instrument and ferrous probe was performed on the uncoated stainless steel substrate with foils of verified thickness. The probe has a resolution of ± 0.1 μm. To measure the coating thickness, the probe tip was gently brought into contact with the sample surface and held until the thickness measurement was displayed on the gauge. The final

dry-film thickness was calculated as the average of five gauge readings taken from nine different locations in a grid pattern on each sample as illustrated in Figure 18 (b).

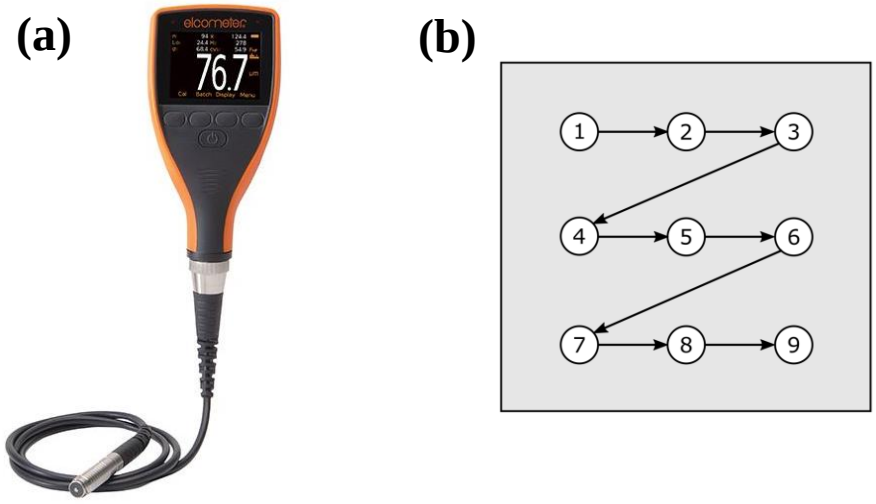

Figure 18: (a) Elcometer 456 digital coating thickness gauge [77]. (b) Sampling plan for the nine measuring points on each sample.

3.3.4 Temperature Measurement and Control

Temperature measurement and control of the heating film were accomplished using a National Instruments cDAQ-9178 chassis and NI-9211 temperature input module. Three type-K thermocouples were used to record the surface temperature, substrate temperature, and environmental temperature. The thermocouple probes were secured to the sample with Kapton tape, with the tip of the probe placed in the approximate center of the heated area on the sample. The data acquisition system was connected to a computer where NI DAQExpress software was used to create a LabView virtual instrument (VI) that processed and displayed the temperature data. Power was delivered to the heating film via a BK Precision 9182B programmable direct current (DC) power supply. The test arrangement is illustrated in Figure 19 (a). Infrared (IR) images of the heating film were captured using a FLIR E60 thermal imaging camera, pictured in Figure 19 (b), to verify the temperature uniformity across the surface of the coating. The camera was calibrated with a thermal emissivity, ε, of 0.95 which provided good agreement with the

surface temperature measurements from the thermocouples. The electrothermal properties and thermal response of the heating film were measured at an environmental temperature of -20°C.

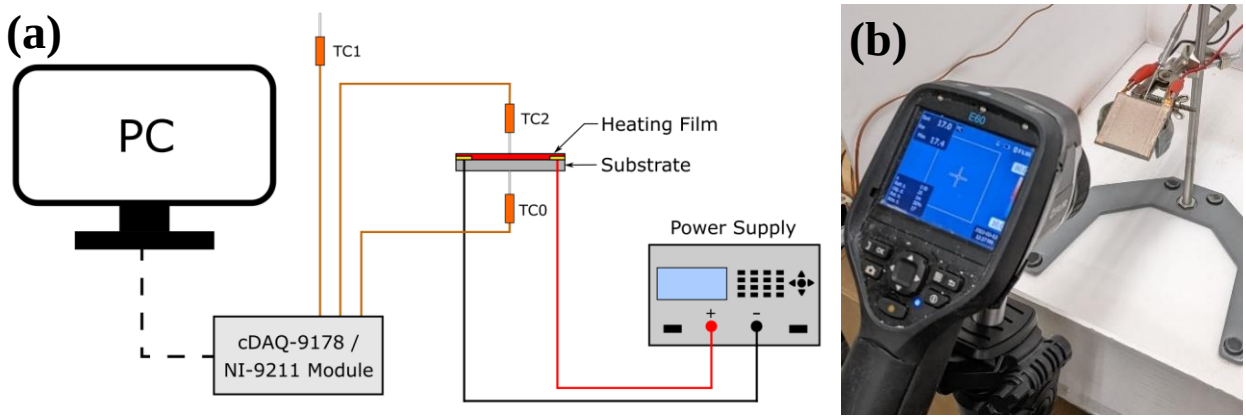

Figure 19: (a) Schematic drawing of the thermocouple arrangement during the temperature measurement process. Three thermocouples were used to record the substrate temperature (TC0), air temperature (TC1), and surface temperature (TC2) simultaneously. (b) The surface temperature was verified using a FLIR E60 thermal imaging camera.

3.3.5 Ice Adhesion Strength Measurement

The ice adhesion strength on the sample surfaces was quantified by measuring the ice adhesion force of an ice sample with a known cross-sectional area using the horizontal shear test method. The ice adhesion force was measured using an Omega DFG55 digital force gauge that was mounted on a modified vise that allows for the smooth linear motion of the probe. The probe has a resolution of ± 0.1 N. The apparatus is pictured in Figure 20.

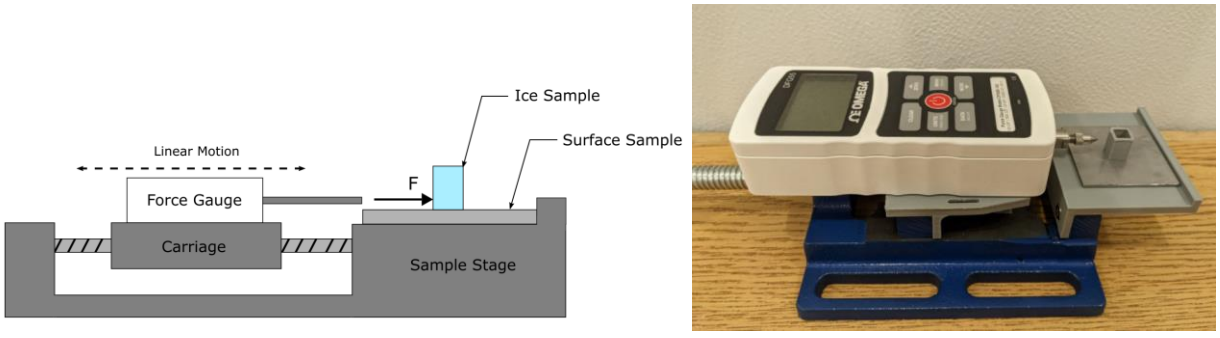

Figure 20: Schematic drawing and photograph of the ice adhesion force measurement apparatus.

The ice samples were prepared using a syringe to inject 1 mL of pre-cooled de-ionized water into a 3D printed square mold with a cross-sectional area of 64 mm². The samples were placed in a

cold room at -10 ± 1°C for 90 minutes to allow the ice to completely freeze on the sample surfaces. Each sample was then placed onto the stand and the probe tip was aligned such that the point of contact was about 7 mm above the sample surface. The gauge was then pushed against the mold until the ice fractured at the interface and was shed from the surface. The peak compressive force was recorded directly from the display on the gauge. The ice adhesion strength was then calculated using Equation (7). The experiment was repeated six times to obtain a reliable average value of the ice adhesion strength for each sample.

3.3.6 Droplet Impact and Icing Test

High-speed imaging was employed to investigate the droplet impact dynamics and freezing behaviour on the fabricated surfaces. Footage of the droplet impact and freezing processes were captured using a Vision Research Phantom v611 high-speed camera with a Sigma 105mm F2.8 DG macro lens. The liquid droplet impact and icing test apparatus is shown in Figure 21. The apparatus consists of an adjustable sample stage, dosing syringe, and LED backlight. The apparatus can be used either at room temperature or inside the cold room for investigation of the freezing behaviour. The high-speed camera is directly connected to a computer for data acquisition in Phantom Camera Control (PCC) software. The PCC software also enables the user to specify the resolution, frame rate, and exposure time settings. The camera was configured to capture footage at 600 frames per second (FPS) at a resolution of 512 x 384px.

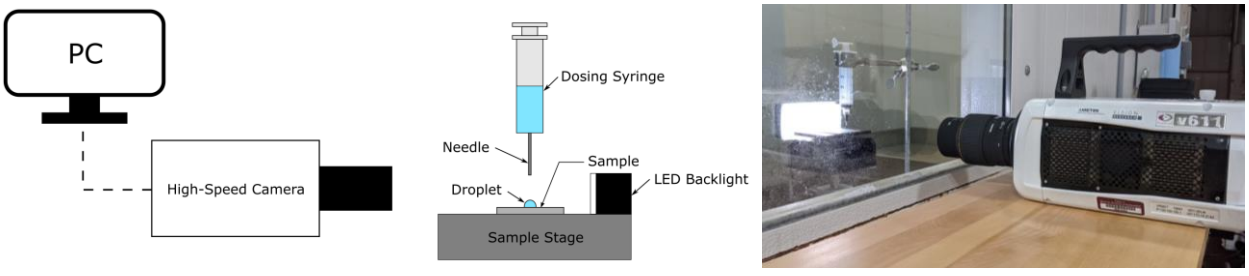

Figure 21: Schematic drawing and photograph of the droplet impact and icing test apparatus.

3.3.7 Anti-icing and De-icing Tests

The samples were subjected to icing conditions to investigate their practical anti-icing and de-icing capabilities. The experimental setup used to quantify the anti-icing performance is pictured in Figure 22. To simulate spray icing, the samples were clamped in a stand inclined at 45° inside a low-temperature chamber at -20 ± 1°C. A commercial pressure sprayer was used to generate a continuous stream of fine mist (flow rate: 0.16 L/min). The nozzle was inserted through a port at the top of the chamber, approximately 50 cm from the sample. The 3.8 L water reservoir was filled with an ice-water mixture which reduced the temperature of the water exiting the nozzle to approximately 5°C. In the anti-icing tests, samples were sprayed for a duration of 150 s. The total ice accumulation and icing delay were compared for the coated and uncoated samples. In later electrothermal tests, the power density was varied to determine the minimum requirement for complete anti-icing of the heated area.

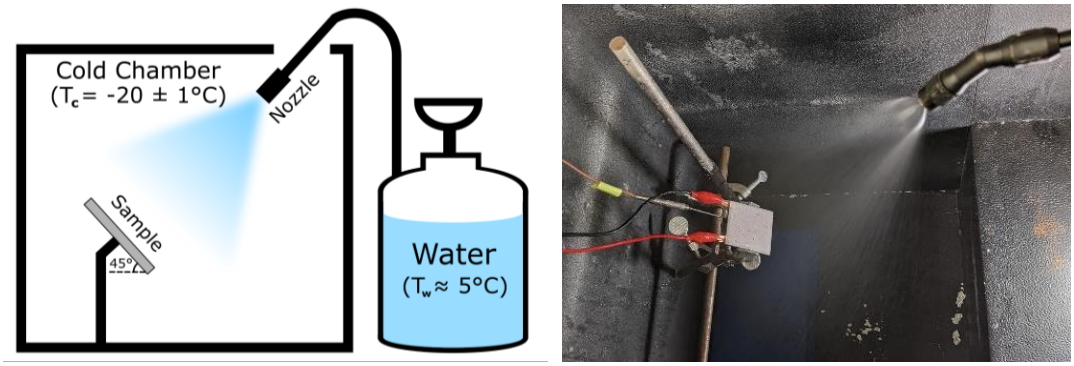

Figure 22: Schematic drawing and photograph of the spray-icing test apparatus.

Similarly, de-icing tests were conducted where a layer of ice was formed on the surface, heat was applied, and the time for de-icing was recorded. The test procedure is illustrated in Figure 23. The ice layer was formed by injecting 5 mL of deionized water into a 3 x 3 cm square 3D printed mold and allowing it to freeze inside a cold chamber at -20 ± 1°C. Once the water had completely frozen and the temperature reached equilibrium, the sample was mounted vertically in a stand and

connected to the power supply. The de-icing time was measured from the point when the power output was turned on to the moment when the ice and mold were fully released from the sample. This process was repeated several times with different surface power density values.

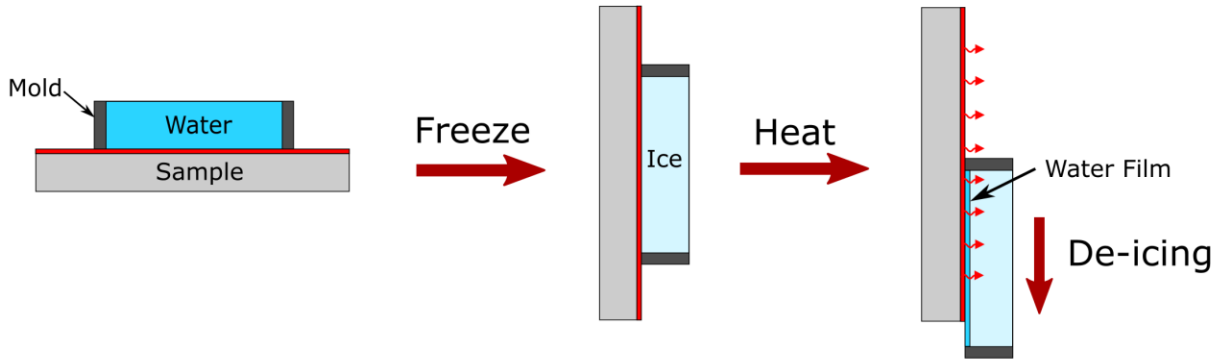

Figure 23: Schematic drawing of the de-icing test process.

3.4 Summary

In this chapter, suitable materials were identified for the fabrication of the heating film and superhydrophobic coating on stainless steel substrates. The heating film will be fabricated with a conductive Ag-Cu epoxy-based heating element. The heating element will be encapsulated between two layers of PDMS to insulate it from the metal substrate. The superhydrophobic coating is based on FAS-13 modified SiO_2 nanoparticles dispersed in PDMS. The hydrophobic surface chemistry alongside the micro-nanoscale roughness created from the aggregation of SiO_2 nanoparticles is expected to achieve the desired superhydrophobic behaviour.

The methodology and equipment used for sample preparation and application by spray coating are presented. Following fabrication, the surface wettability and electrothermal properties of the samples are characterized. The static contact angle and contact angle hysteresis are measured using a Dataphysics OCA 15EC contact angle measurement system. A Vision Research Phantom v611 high-speed camera was used to capture footage of the droplet sliding and impact processes. Scanning electron microscopy was employed to investigate the micro-nanostructure of the coating.

The temperature response, power density, and thermal stability of the heating film are measured using thermocouples affixed to the samples and verified with a thermal imaging camera.

Concluding this chapter, the methods that are used to evaluate the anti-icing performance are introduced. All of the icing tests were conducted in a cold chamber at -20°C, with the exception of the ice adhesion strength experiment which was carried out in a cold room at -10°C. The ice adhesion strength and droplet freezing time are measured to verify the expected anti-icing abilities of the superhydrophobic coating and compare the performance to the untreated surfaces. Finally, simulated spray icing tests are carried out to quantify the minimum power density required for anti-icing and de-icing on the hybrid coating.

CHAPTER 4

Sample Fabrication and Characterization

4.1 Sample Fabrication

The fabrication of the hybrid superhydrophobic heating film was performed as illustrated in Figure 24. First, the substrate was prepared by sandblasting, cleaning, and priming. Next, the electric heating film was fabricated by spraying a layer of PDMS insulation, pasting the copper foil electrodes, then spraying the Ag-Cu epoxy heating element, followed by the second layer of PDMS insulation. Finally, the SiO_2/PDMS superhydrophobic coating was sprayed over the top surface of the heating film.

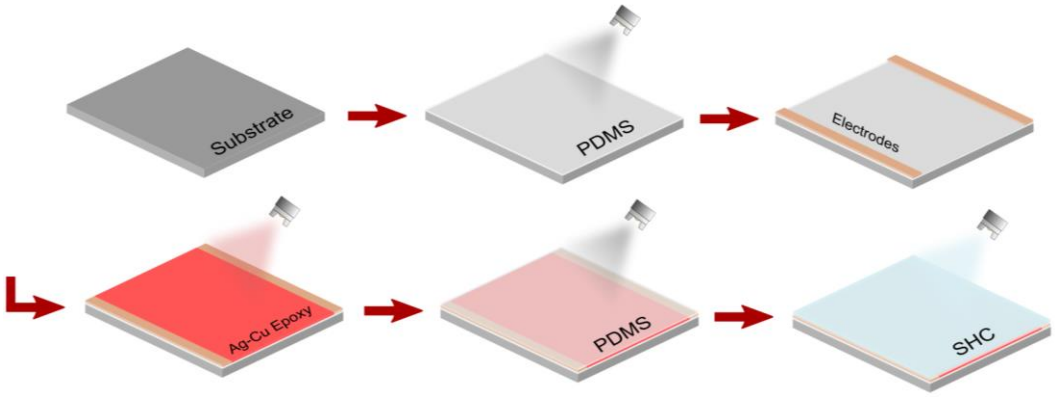

Figure 24: Schematic illustration of the fabrication process of the superhydrophobic-electrothermal coating.

4.1.1 Surface Preparation

The as-received 2.032 mm thick 17-4 PH SS sheets were cut into 50 mm x 50 mm samples using a band saw, as shown in Figure ***25*** (a). The samples were then sandblasted with #120 grit (100 µm abrasive size) Al_2O_3 abrasive media to enhance the adhesion of the coating. Samples were cleaned in an ultrasonic bath with acetone for 10 minutes, followed by cleaning in ethanol for 10 minutes to remove any debris, oils, and other residues from the surface. The sandblasted (SB) sample is shown in Figure ***25*** (b). After air-drying for 15 minutes, 2.0 g of DOWSIL 92-023 primer was

spray-coated onto the sample in a very thin layer to improve the quality and adhesion of the subsequent PDMS layer.

4.1.2 Heating Film Fabrication

First, 3.0g of the PDMS base, 3.0g of hexane, and 0.3g of PDMS curing agent were added to a flask and stirred with a magnetic stirrer for 10 minutes. The solution was then spray-coated directly onto the prepared sample. The samples were left to dry at room temperature for 15 minutes to allow any residual hexane to evaporate, preventing bubbles from remaining after curing. The sample was then cured at 125°C for 30 minutes. Copper foil was cut into 80 mm lengths and glued along opposite edges of the sample for the electrodes. The glue was allowed to dry at room temperature for 5 minutes. A multimeter was used to verify that there was no electrical continuity between the electrodes before applying the conductive coating.

To prepare the conductive coating for the heating element, 843ER parts A (silver-coated copper resin) and B (hardener) were stirred individually for 5 minutes until homogenous. 5.0 g of part A was mixed with 1.4 g of part B and stirred for another 5 minutes. The prepared 843ER solution was then sprayed onto the sample in several passes, waiting 3 minutes between passes, until complete coverage was obtained. The coating was left to dry at room temperature for 30 minutes before curing at 80°C for 2 hours. After curing, a multimeter was used to verify the electrical continuity across the coating and ensure there was no short-circuiting with the substrate.

A thin layer of DOWSIL 92-023 primer was then applied over the cured 843ER epoxy by spray-coating. The primer was allowed to dry at room temperature for 1 hour. The primer layer is essential to mitigate inhibition of the PDMS curing process by the underlying epoxy. Next 3.0 g of the PDMS base, 3.0 g of hexane, and 0.3 g of the curing agent were added to a flask and stirred with a magnetic stirrer for 10 minutes. The solution was spray-coated onto the primed sample. The

sample was left to dry at room temperature for 15 minutes before curing at 125°C for 30 minutes. The fabricated heating film (HF) sample is shown in Figure ***25*** (c).

4.1.3 Superhydrophobic Coating Fabrication

To prepare the superhydrophobic coating the SiO_2 nanoparticles were first hydrophobically modified by adding 0.1 g of FAS-13 to 9.9 g of 100% anhydrous ethanol and stirring for 1 hour to complete the hydrolysis reaction. A total of 1.0 g of SiO_2 nanoparticles (0.6 g 15-20 nm and 0.4 g 60-70 nm) were added to the solution. After adding the SiO_2, the solution was stirred and ultra-sonicated for 1 hour. The solution was then heated to 80°C under continuous stirring until the ethanol had completely evaporated, resulting in the modified hydrophobic SiO_2 nanoparticles.

In a separate beaker, 1.0 g of the PDMS base was mixed with 10 g of hexane and stirred for 5 minutes. The modified hydrophobic SiO_2 nanoparticles were then added to the PDMS solution and stirred for 15 minutes, then ultra-sonicated for 15 minutes. 0.1 g of the PDMS curing agent was then added to the solution and stirred for 5 minutes. The sample was sprayed with a thin layer of DOWSIL P5200 adhesion promoter and dried for 1 hour. The prepared SiO_2/PDMS mixture was then sprayed onto the surface, making 2-3 passes to ensure complete coverage. The sample was then immediately cured at 125°C for 30 minutes. The fabricated superhydrophobic heating film (SH-HF) sample is shown in Figure ***25*** (e).

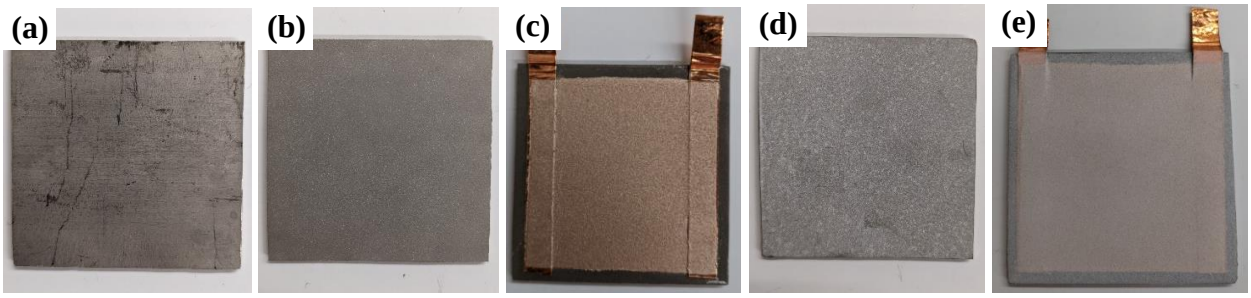

Figure 25: Images of the fabricated samples: (a) as-received stainless steel (SS), (b) sandblasted stainless steel (SB), (c) heating film (HF), (d) superhydrophobic stainless steel (SH-SS), and (e) superhydrophobic heating film (SH-HF).

The optimal ratio of nanoparticle sizes which maximized the static contact angle was determined experimentally. Samples with varying concentrations of 15-20 nm, 60-70 nm, and 200 nm SiO_2 nanoparticles were fabricated and tested. The resulting CA measurements for ten samples of different compositions are shown in Figure 26.

Sample	15-20nm [wt.%]	60-70nm [wt.%]	200nm [wt.%]
1	1.000	0.000	0.000
2	0.167	0.167	0.667
3	0.000	0.500	0.500
4	0.500	0.000	0.500
5	0.333	0.333	0.333
6	0.167	0.667	0.167
7	0.000	0.000	1.000
8	0.667	0.167	0.167
9	0.000	1.000	0.000
10	0.500	0.500	0.000

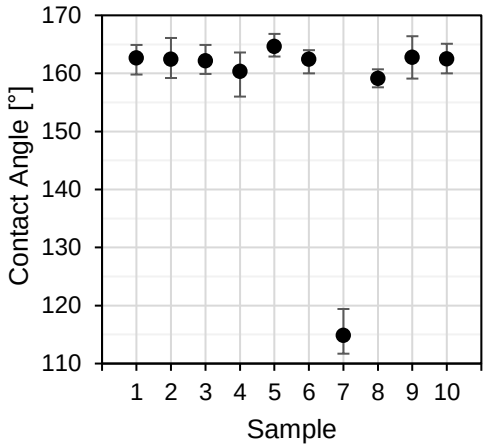

Figure 26: Test plan and the measured contact angle for samples with variable SiO_2 nanoparticle size concentration.

The results were further analyzed in DesignExpert 13 to determine the optimal weight percentage ratio of each component. A three-factor (A: 15-20 nm, B: 60-70 nm, C: 200 nm) mixture design was created with 10 runs. The initial analysis was performed using the Scheffe modelling technique with special quartic fitting, which produced a p-value of 0.0741. The response surface is shown below in Figure 27 (a). Optimization of the response surface predicted a maximum CA of 170.4º with component fractions A: 21%, B: 31%, and C: 48%. A new sample (# 11) was fabricated with the predicted optimal composition and a CA of 160.7º was measured. The CA on this sample was significantly lower than predicted by the model, so another solution was tested. Another new sample (# 12) with components A: 60%, B: 40%, and C: 0% was fabricated and recorded a CA of 165.2º. The results from both of the new samples were added to the model as validation points and the response was re-analyzed. With the inclusion of the verification points, the best fit is quadratic with a p-value of 0.0147. The new response surface including the validation

points is shown in Figure 27 (b). The quadratic response surface indicates that only the concentration of component C had a significant effect on the CA response. There is a dramatic reduction in the CA as the concentration of component C (200 nm) approaches 100%. No significant relationship was found between the concentrations of components A (15-20 nm) or B (60-70 nm) and the response. Based on the model prediction, superhydrophobic behaviour is expected provided that the weight percentage of the 200 nm component is less than 80%, regardless of the mixture of the other two components making up the remaining 20%.

Superhydrophobicity was observed for all of the fabricated samples except for sample #7 which consisted of 100% 200 nm SiO_2. Therefore, a further analysis was performed excluding sample #7 which was a notable outlier from the rest of the responses. With this outlier excluded, all of the fitting models produced a p-value >> 0.05; therefore no statistically significant trend was observed in the remaining data. The concentration of component C is only significant above 66.7% and therefore the threshold is not represented on the response surface when sample #7 is excluded. The remaining responses were all within 3º of the mean CA of 162.3º. This small variation can be attributed to noise due to external factors in the fabrication process such as the concentration of PDMS in the coating mixture and randomness in the spray-coating and sandblasting processes. Since the nanoparticle size ratio was found to have little influence on the CA above the minimum concentration of components A and B, the composition with the highest measured CA was selected to fabricate all further samples (Sample # 12; A: 60%, B: 40%, and C: 0%).

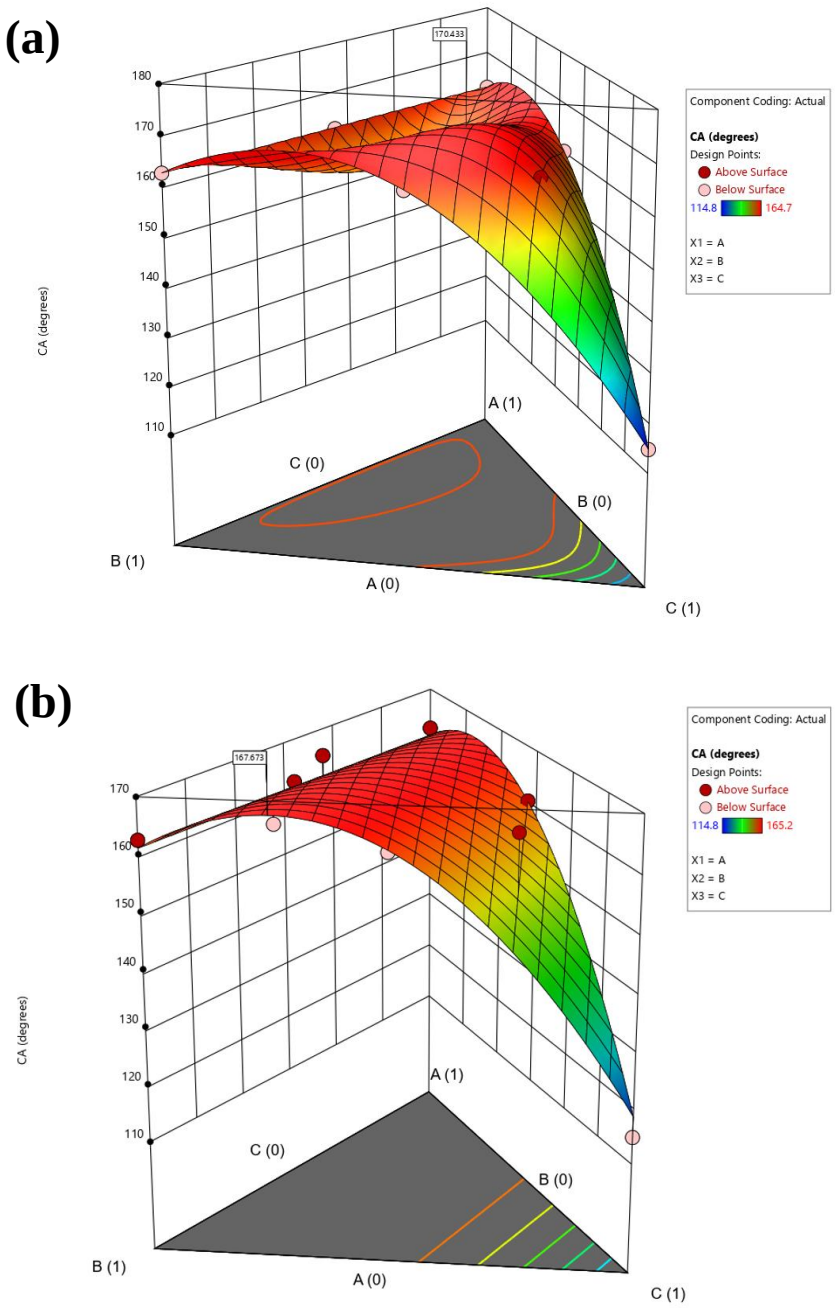

Figure 27: Response surfaces for optimization of contact angle with varying concentrations of SiO_2 nanoparticle sizes (Component A: 15-20 nm wt. %, Component B: 60-70 nm wt. %, Component C: 200 nm wt. %). (a) Special quartic response surface for the initial 10 runs. (b) Quadratic response surface including the two additional validation points.

4.2 Surface Wettability

The surface wettability of the samples was quantified by measuring the CA of de-ionized water on the coated and uncoated surfaces. To obtain accurate CA measurements, three droplet contour fitting methods were compared: ellipse, tangent, and polynomial fitting. The three methods are shown in Figure 28, each applied to the same droplet on the same sample.

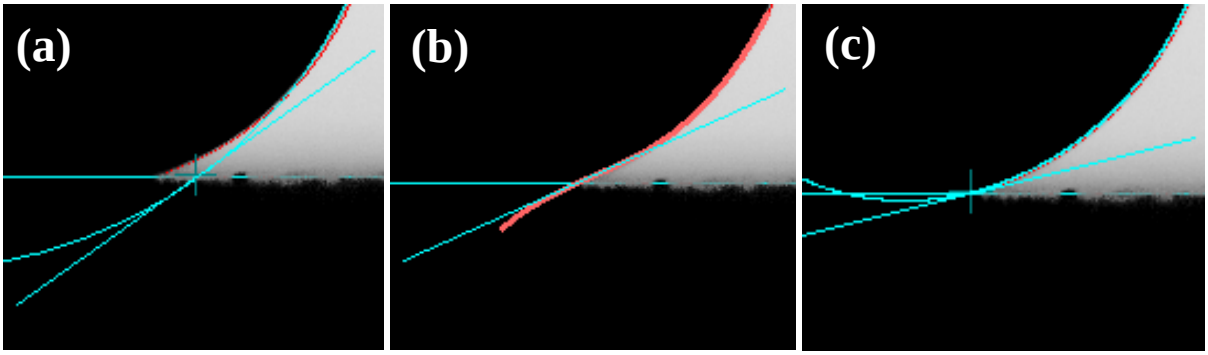

Figure 28: Comparison of (a) ellipse fitting, (b) tangent fitting, and (c) polynomial fitting methods for the droplet contour.

Ellipse fitting provided a good fit to the droplet contour for CA < 120°, however, for CA > 120° the fit started to deviate significantly from the visible contour at the three-phase contact point. This deviation resulted in the ellipse fitting model producing a contact angle of 144.6° which is shown to underestimate the actual contact angle. Tangent and polynomial fitting each aligned more closely with the droplet contour, giving contact angles of 156.4° and 166.1° respectively. The tangent fitting method uses edge detection image processing techniques to directly draw a tangent at the contact point. Therefore this method is more sensitive to the lighting conditions, viewing angle, and placement of the baseline. Subjective placement of the baseline resulted in a larger variance in the experimental data, especially for surfaces with high roughness. The polynomial fitting method extracts the drop profile using image processing techniques and fits a polynomial equation to the observed drop profile. The contact angle is calculated from the slope of the polynomial where it intersects the baseline [78]. The polynomial fitting model provided the most

accurate placement of the three-phase contact point and resulted in the most consistent measurements. Therefore, polynomial fitting was selected as the default method for all subsequent CA measurements.

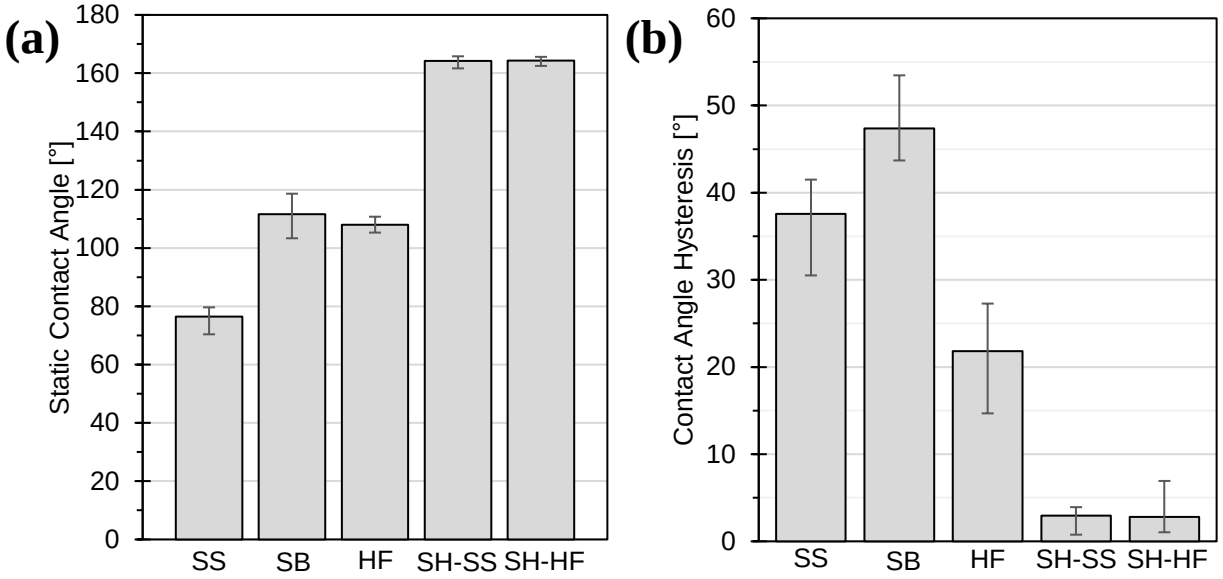

Figure 29: Measured (a) static contact angle and (b) contact angle hysteresis on the untreated stainless steel (SS), sandblasted stainless steel (SB), heating film (HF), superhydrophobic-coated stainless steel (SH-SS), and superhydrophobic-coated heating film (SH-HF) samples.

The measured static contact angle data is presented in Figure 29 (a). A contact angle of 76.5° ± 6° was measured on the as-received stainless steel. The contact angle increased to 111.6° ± 8° after the base metal was roughened by sandblasting. The protective top layer of the heating film comprised of smooth PDMS recorded a contact angle of 108.0° ± 3°. The wetting behaviour of the SiO_2/PDMS coating was investigated when applied to both sandblasted stainless steel and heating film samples. On the superhydrophobic stainless steel (SH-SS) sample the contact angle was measured as 164.2° ± 3°. Similarly, a CA of 164.3° ± 2° was recorded on the superhydrophobic heating film (SH-HF). The combination of surface roughness and low surface energy caused the contact angle on the SiO_2/PDMS coating to exceed the 150° threshold required for superhydrophobicity. As predicted by the Cassie-Baxter model, the static contact angle was found

to be strongly influenced by the roughness and chemical composition of each sample. The validity of the Cassie-Baxter model is confirmed by the data presented in this study, as it has been demonstrated that sufficient surface roughness increased the measured contact angles on both hydrophilic and hydrophobic surfaces.

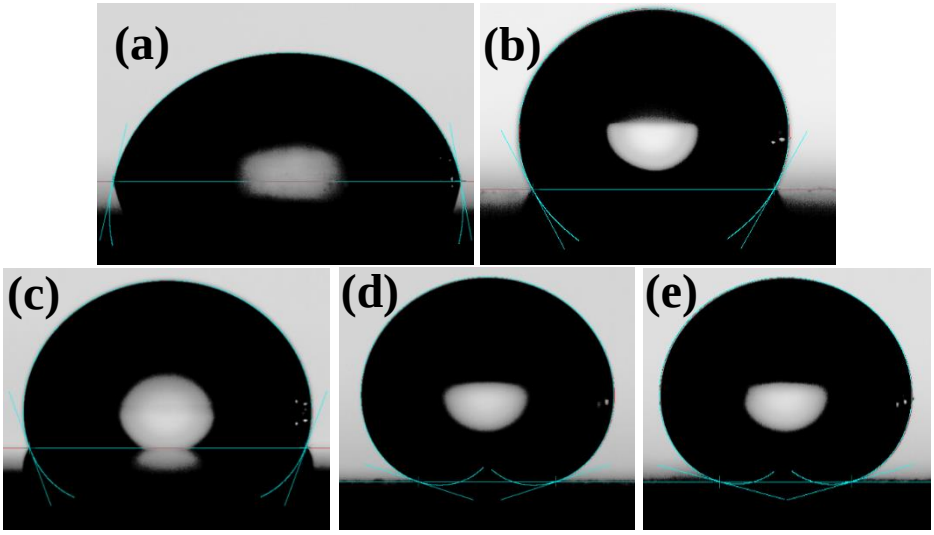

Figure 30: Static contact angle measurements: (a) SS (78.2°), (b) SB (118.6°), (c) HF (110.2°), (d) SH-SS (162.0°), (e) SH-HF (164.5°).

The CAH and SA were then measured to characterize the dynamic wetting behaviour of the samples. Equation (5) was used to calculate the CAH using the measured ACA and RCA data shown in Figure 31. The results for each sample are presented in Figure 29 (b). The CAH on the base metal substrate was measured as 37.6° ± 7°. The CAH increased to 47.4° ± 6° on the SB sample which is attributed to the additional pinning points created by the greater surface roughness. On the smooth PDMS surface of the HF, the CAH decreased to 21.8° ± 7°. The CAH substantially decreased to just 2.9° ± 2° and 2.8° ± 4° on the SH-SS and SH-HF samples respectively.

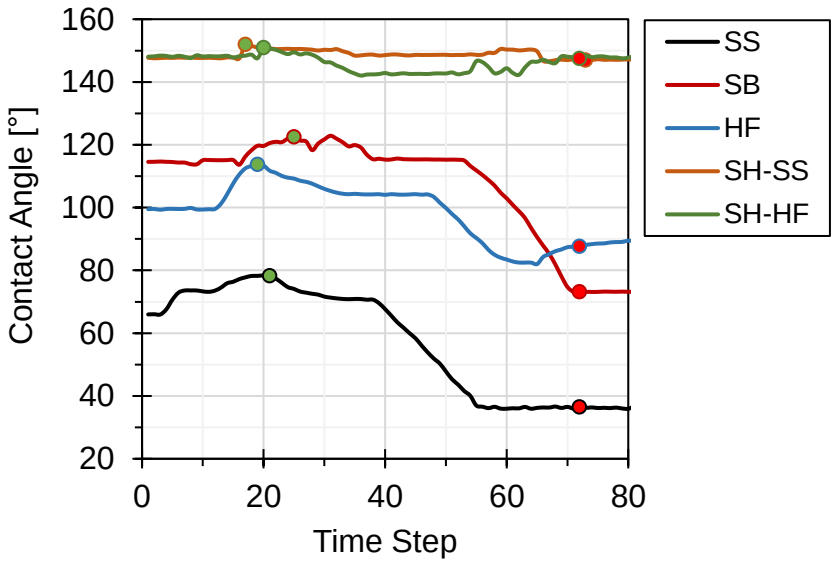

Figure 31: Plot showing the change in contact angle as liquid is added, then removed from a sessile droplet. One run is shown for each of the fabricated samples. The ACA and RCA for each sample are indicated by the green and red markers respectively.

A high-speed camera was used to capture images of water droplets sliding off of the sample surfaces. A 20 µL droplet of de-ionized water was placed onto the horizontal surface with a syringe and the surface was gradually tilted until the droplet started to slide. No droplet sliding was observed on the SS, SB, or HF samples, even when inclined at 90° or fully inverted. A SA of 3° was recorded for both the SH-SS and SH-HF samples. As shown in Figure 32, a droplet was captured sliding off of the surface when the sample was inclined at an angle of 3° from the horizontal. The results presented in this section confirm the superhydrophobic property of the SiO_2/PDMS coating. The SH-SS and SH-HF samples each possessed CA > 150°, CAH < 10°, and SA < 10°; thereby meeting each of the criteria for superhydrophobicity.

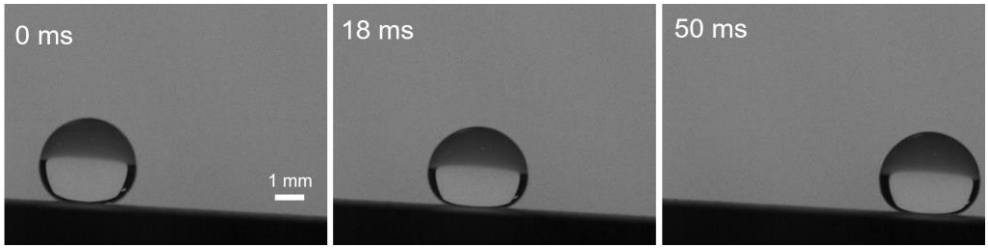

Figure 32: High-speed capture of a droplet sliding on SH-SS when the sample is tilted slightly by 3°.

Additional high-speed video footage was captured to investigate the droplet dynamics during impact on the superhydrophobic coating. The droplet impact tests were conducted at room temperature. A stainless steel dispensing needle with an inner diameter of 0.5 mm was used throughout all tests to maintain a consistent droplet volume of 20 μL. The syringe was held in a stand and centered over the sample with the needle tip positioned approximately 1 cm above the sample surface. A series of images of the impact process on SS and SH-SS were extracted from the high-speed footage and are presented in Figure 33.

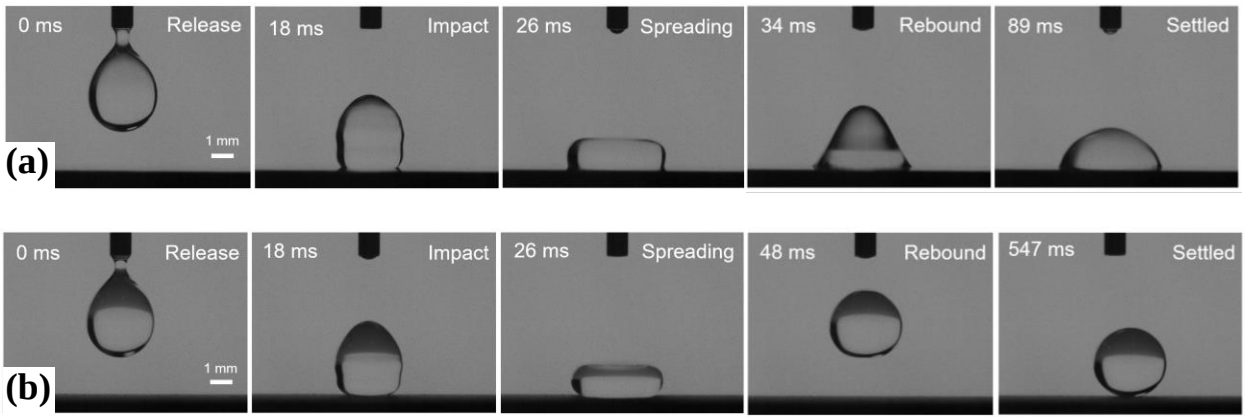

Figure 33: High-speed captures of a droplet impacting on (a) SS and (b) SH-SS. The moment of release, initial impact, maximum spread, maximum rebound, and settled state are shown for each surface.

When the droplet impacted the horizontal untreated substrate at a velocity of approximately 110 mm/s the droplet spread to a maximum diameter of 4.6 mm. There was no rebound, though the droplet is observed briefly oscillating until the vertical momentum has dissipated within the droplet. After 89 ms the droplet had come to rest on the untreated surface. On SH-SS the droplet spreads to a maximum diameter of 4.4 mm and then completely rebounds from the surface after the initial impact. The droplet continued bouncing on the surface, fully rebounding from the surface eleven times over a period of 450 ms, then oscillated on the surface for a further 80 ms. The oscillations gradually slowed and the droplet settled to rest after 547 ms. The diameter of the droplet at rest is 3.4 mm. Since the impact velocity was relatively low there was no splashing or

breakup of the drop observed. The longer droplet settling time and reduced contact time on the superhydrophobic coating contribute to delaying the onset of freezing in anti-icing applications. Figure 34 shows a droplet impact on SH-SS when tilted at an angle of 3° from the horizontal. Due to the low sliding angle and rebounding behaviour, the droplet quickly bounces out of the view of the camera and slides off of the surface before settling. Therefore, it is likely that water droplets will roll or bounce off of the surface before freezing which is expected to reduce the rate of ice accretion.

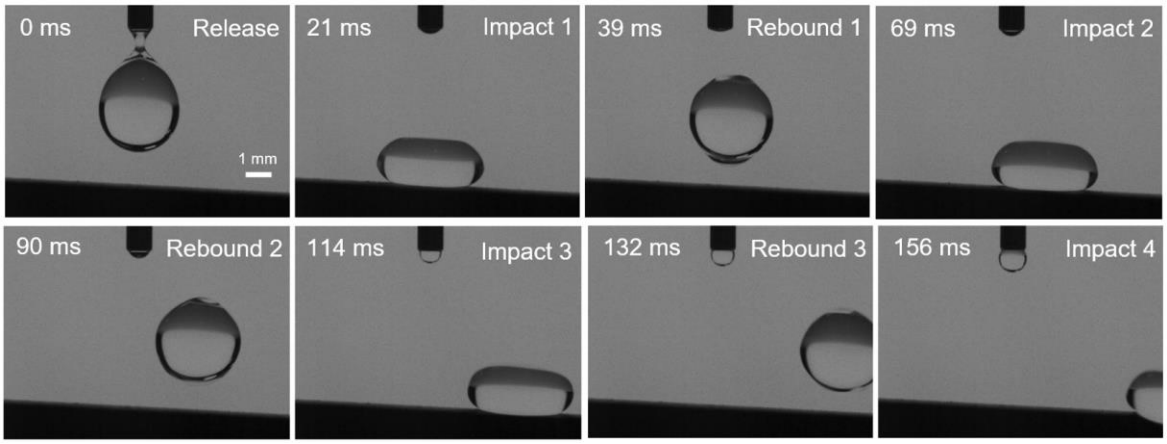

Figure 34: High-speed capture of a droplet impacting on SH-SS inclined at 3°.

4.3 Microstructure Characterization

The SEM micrographs shown in Figure 35 were captured to investigate and characterize the microstructure of the fabricated samples. The smooth surface of the untreated stainless steel is shown in Figure 35 (a) and the roughened sandblasted sample is shown in Figure 35 (b). Sandblasting is shown to create irregular micro-scale roughness across the entire surface. Naturally, the microstructure produced by sandblasting is random but can be affected by changing the blasting parameters including the standoff distance and size of the abrasive media [79].

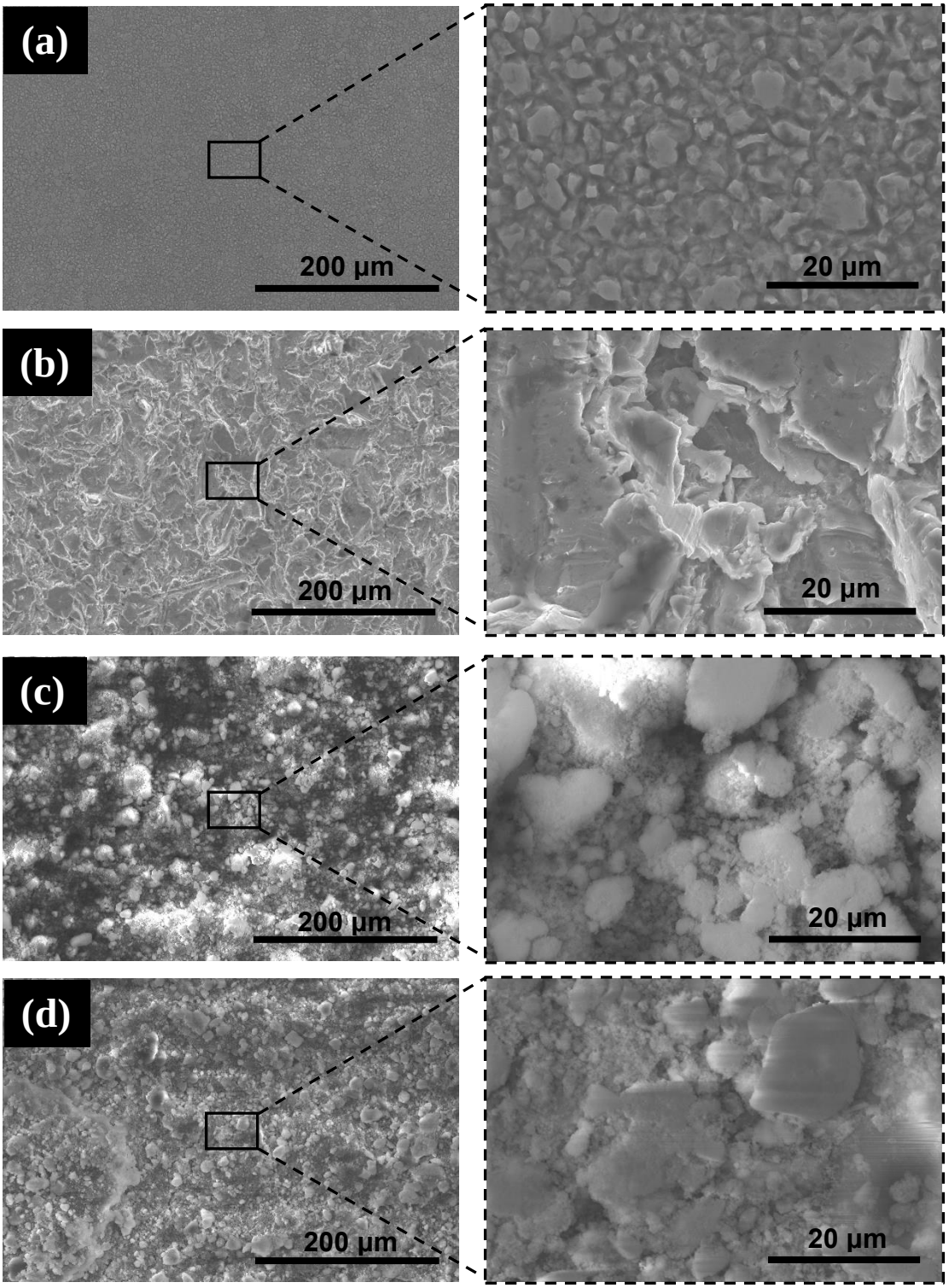

Figure 35: SEM images of the surface topography of various samples at 600x magnification (left), with the highlighted area magnified to 5000x (right). (a) Stainless steel (SS), (b) sandblasted stainless steel (SB), (c) superhydrophobic-coated stainless steel (SH-SS), and (d) superhydrophobic-coated heating film (SH-HF).

The SEM images in Figure 35 (c) and (d) reveal the rough surface morphology of the SiO_2/PDMS superhydrophobic coating. The micro-nanostructure of the coating was composed of hierarchical agglomerations of SiO_2 nanoparticles that are bound together by the PDMS adhesive. The rough surface morphology allows a high fraction of air to be trapped in the valleys and gaps between the embedded nanoparticles. Alongside the hydrophobic surface chemistry, the dual-scale surface roughness of the coating is responsible for the superhydrophobic behaviour, which is consistent with the expectations from the Cassie-Baxter model.

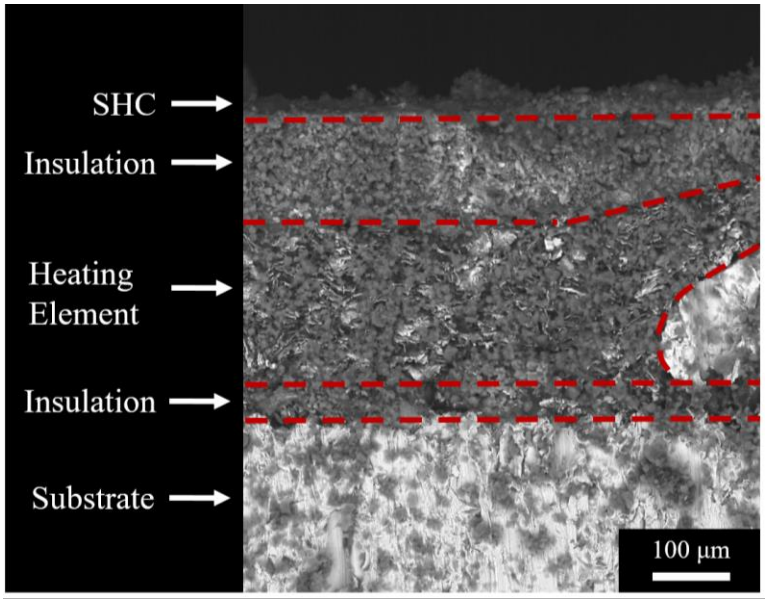

Figure 36: Cross-sectional backscattered electron SEM image of the SH-HF sample which shows each layer of the hybrid coating.

A cross-sectional image of the sample is shown in Figure 36. The relative layer thicknesses can be approximated using the image scale. The PDMS layers have a thickness of 60 µm and 140 µm for the bottom and top layers respectively. The Ag/Cu epoxy heating element had a thickness of 190 µm and the SiO_2/PDMS superhydrophobic coating had a thickness of 3 µm. The total thickness of the coating was estimated as 390 µm which agrees with the probe-measured values obtained in Section 4.4. In future work, further optimizations can be made to improve the heating efficiency based on the layer thicknesses. Increasing the thickness of the inner layer of PDMS would better

insulate the substrate to reduce unnecessary heating of the substrate. Similarly, reducing the thickness of the outer layer of PDMS would be expected to improve conductive heat transfer to accumulated ice or water on the outer surface.

4.4 Coating Thickness Measurement

The dry-film thickness of the coating was measured for three HF samples and three SH-HF samples with a digital coating thickness gauge following the procedure outlined in Section 3.3.3. Measuring the thickness at various locations on the surface of multiple samples provided insight into the homogeneity of the coating and the consistency of the fabrication process between samples. The measured data for the nine sampling points on the six different samples is presented in Figure 37.

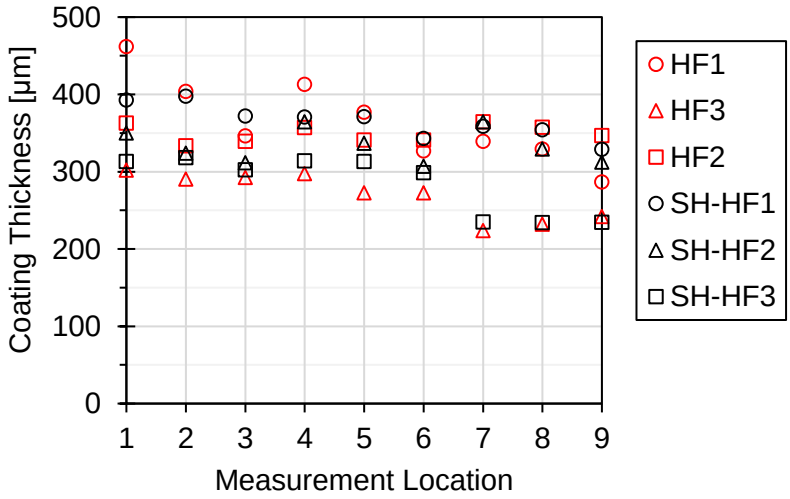

Figure 37: Coating thickness measured at nine locations on six unique HF and SH-HF samples to verify the coating uniformity.

The data shows that the minimum thickness variation from the mean thickness for an individual sample was 16 µm (HF2) and the maximum was 88 µm (HF1). The average deviation from the mean thickness across all six of the samples was ± 41 µm. This is attributed to the inconsistency that is inherent in the manual spray coating process, however, the variation was not significant

enough to have any noticeable adverse effects on the properties of the coating measured in the other experiments. It was also observed that there was a slight bias for the coating to be thicker along the left edge (Location 1, 4, 7) of the sample. This may have been caused by placing the samples on a surface that was not perfectly level before the coating had dried, causing the liquid coating to run slightly thicker to one side.

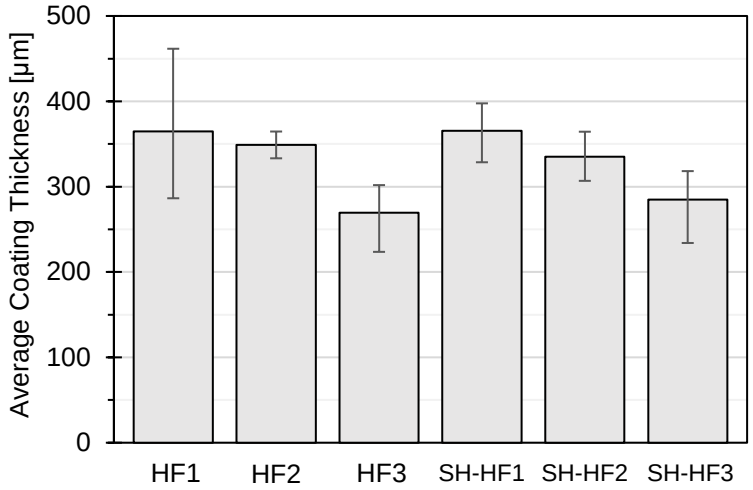

Figure 38: Average coating thickness for the six unique HF and SH-HF samples.

Figure 38 shows the average dry-film thickness from the nine measurement points for each of the six samples. Comparing the results between samples, the average thickness is relatively consistent ranging from 269 µm to 365 µm, although there is a noticeable difference between the thickness of samples HF3 and SH-HF3 and the other four samples. The samples were fabricated in batches of two (i.e. HF1 and SH-HF1, HF2 and SH-HF2, HF3 and SH-HF3) which is likely the reason for the similar thickness measurements for both samples in each batch. It was possible to control the thickness to some degree within each batch, however, precise consistency between batches was a challenge to achieve with the manual spray coating process. The homogeneity and replicability of the coating could be increased with higher quality manual spraying equipment or through automation of the spray-coating process.

4.5 Electrothermal Properties

Experiments were carried out to investigate the electrothermal properties of the fabricated electric heating film samples. The key performance indicators of the heater were measured, including the thermal response behaviour, power density, cycling stability, and heating uniformity. The coated area of the heating film sample (excluding the area covered by the electrodes) was measured as 14.52 cm². The nominal resistance of the heating film was recorded as 0.34 ± 0.01 Ω at the initial temperature of -20°C. The sheet resistance of 0.1 Ω/sq was determined by dividing the manufacturer-defined resistivity of the Ag-Cu epoxy (1.8×10^{-3} Ω·cm) by the average probe-measured film thickness of 176 μm. The electrothermal properties of the heating film across the full range of tested input parameters are summarized in Table 5.

Table 5: Summary of the measured electrothermal properties of the electric heating film. [1] The maximum temperature was limited to 100°C to preserve the integrity of the heating element during the 10 A and 12 A tests.

Current [A]	Voltage [V]	Power [W]	ΔT_{max} [°C]	Heating Rate [°C/s]	Power Density [W/cm²]
2	0.68	1.36	7	0.016	0.09
4	1.36	5.43	23	0.056	0.37
6	2.04	12.2	48	0.113	0.84
8	2.69	21.5	90	0.219	1.48
10	3.42	34.2	120 [1]	0.318	2.36
12	4.18	50.2	120 [1]	0.556	3.46

The thermal response of the heating film at room temperature was investigated by applying a constant input current to produce a temperature rise. Power was supplied continuously for 15 minutes or until the temperature exceeded the maximum working temperature of 100°C. The maximum temperature was limited to 100°C for safety and to prevent the heating element from burning out in the 10 A and 12 A tests. The resulting temperature-time curves for 2 A to 12 A input current are presented in Figure 39. Increasing the input power was shown to increase both

the heating rate and the maximum steady-state temperature. The maximum 12 A current corresponded to a total power draw of 50.2 W and a surface power density of 3.46 W/cm^2. With the maximum input power, the surface temperature could be increased from -20°C to 10°C, sufficient for anti-icing, in just 45 seconds. The maximum temperature rise of 120°C was achieved in less than 4 minutes.

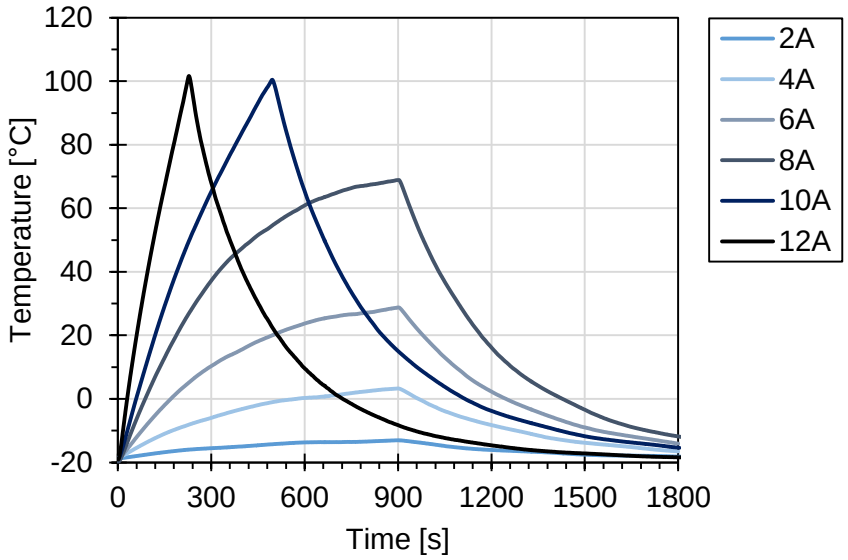

Figure 39: Temperature-time curves for 2 A to 12 A input current measured at an environmental temperature of -20°C.

The temperature rise, ΔT, is calculated as the difference between the measured surface temperature and ambient air temperature. As shown in Figure 40, a clear linear trend is observed when the power density is plotted against the corresponding maximum ΔT for each test. The slope corresponds to the heat performance, which is a measure of the temperature increase per unit of input power. For the Ag-Cu epoxy heating element, a heat performance of 51.4°C·cm²/W was obtained at -20°C. This result is comparable to published values for indium tin oxide (ITO) heaters (88°C·cm²/W) when considering the difference in the environmental temperature [56].

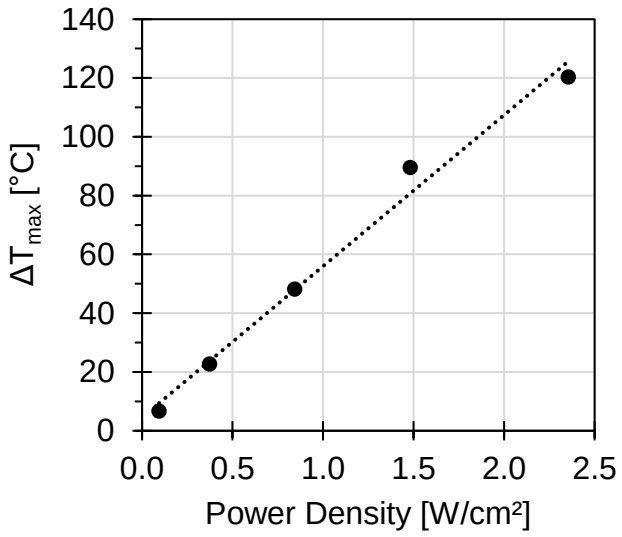

Figure 40: Power density versus the maximum temperature rise from the thermal response tests at -20°C. The heat performance of the Ag-Cu epoxy heating element is given by the slope of the linear trend line.

The input power and heating scheme will depend on whether anti-icing or de-icing is desired. Achieving a high maximum ΔT is desirable for anti-icing, where the surface temperature must be maintained above the freezing point of water. The maximum temperature rise effectively limits the minimum operating temperature for anti-icing. Therefore, low input power supplied continuously, depending on the ambient temperature, is most suitable for anti-icing. Conversely, fast thermal response time and high power density are essential for de-icing such that the interfacial layer of ice is melted as fast as possible. Thus, efficient de-icing requires high input power that is supplied over a short time to minimize energy consumption.

A thermal cycling test was carried out to verify the thermal stability and ensure that the maximum achievable temperature does not degrade over time. An input current of 8 A was supplied for 15 minutes, after which the power was turned off and the sample was allowed to cool at room temperature for 15 minutes. This process was repeated for a total of 6 cycles. The results of the cycling test in Figure 41 show that the thermal performance of the heating element was very

consistent, with no significant degradation in the maximum attainable temperature over the 3-hour testing period.

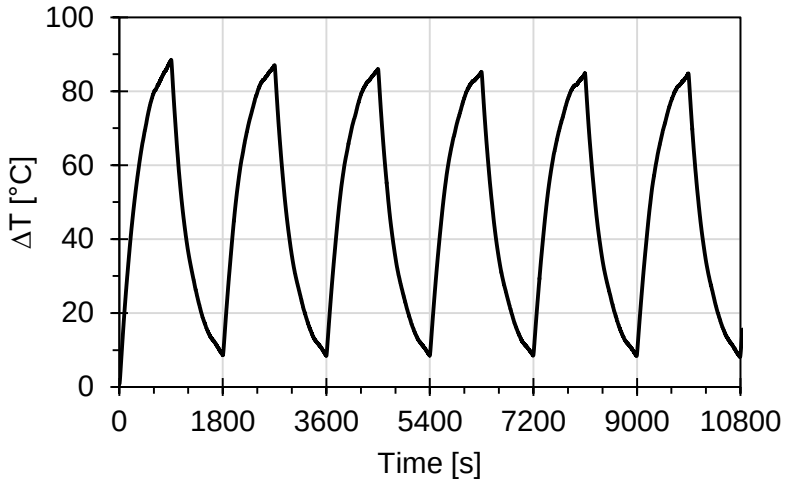

Figure 41: Result of the thermal cycling test performed over a 3-hour time period from an initial temperature of -20°C with an input current of 8 A.

To investigate the uniformity of the heat generation, infrared images of the heating film sample in Figure 42 were captured with a thermal imaging camera inside a cold chamber at -20°C while the heating film was supplied with a constant current of 8 A. For an input of 8 A, the corresponding power density was 1.48 W/cm^2. The images show the rapid increase in the average surface temperature from -20.0°C to 4.4°C within the first 60 seconds of heating. A maximum surface temperature of 84.6°C was reached after 15 minutes. The maximum temperature variation within the heated region was approximately ± 5°C from the average, suggesting that the heating distribution was quite uniform. No areas of highly concentrated heating were observed which could be caused due to significant damage or defects in the coating. Marginally higher surface temperatures are seen in the left-middle region of the sample. From the data for sample HF3 in Figure 37, it is apparent that the thickness of the coating is an average of 15 µm greater in this region. The slightly higher thickness would correspond to lower electrical resistance and is likely responsible for the minor temperature variation in the heated region.

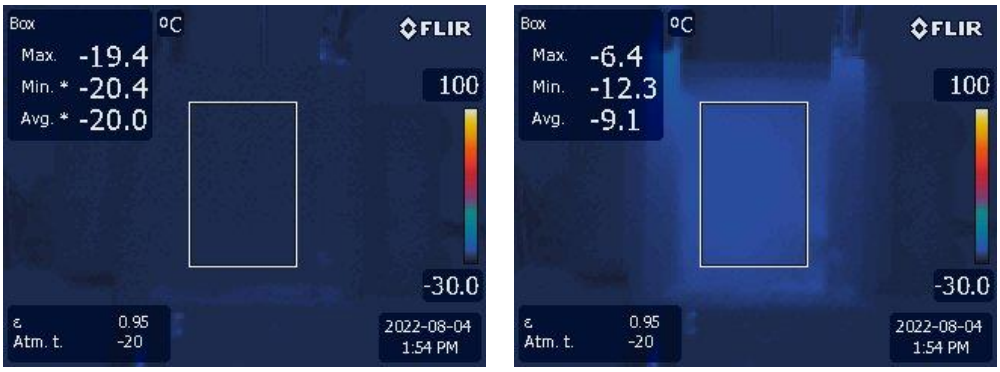

(a) Initial

(b) After 15 seconds

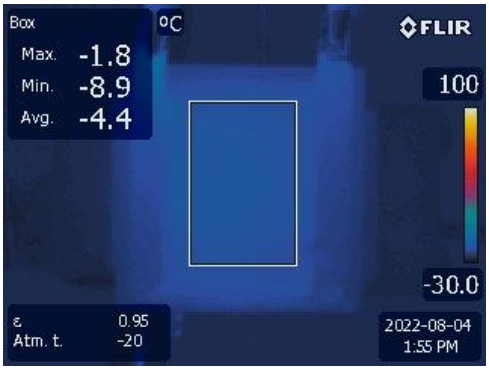

(c) After 30 seconds

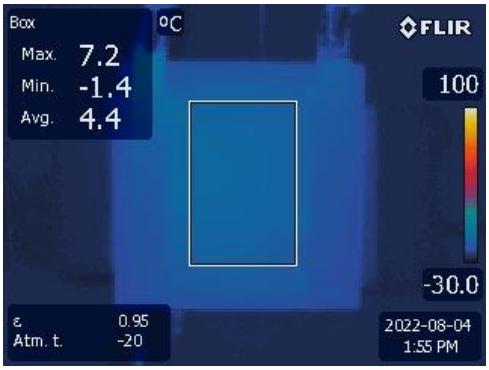

(d) After 1 minute

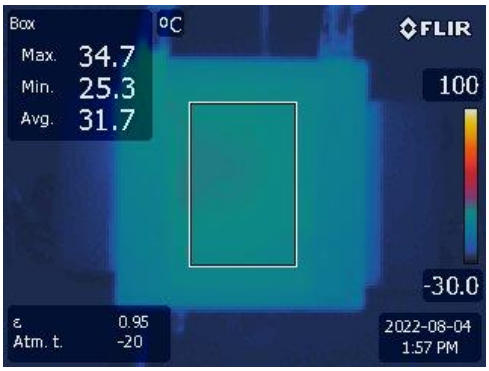

(e) After 3 minutes

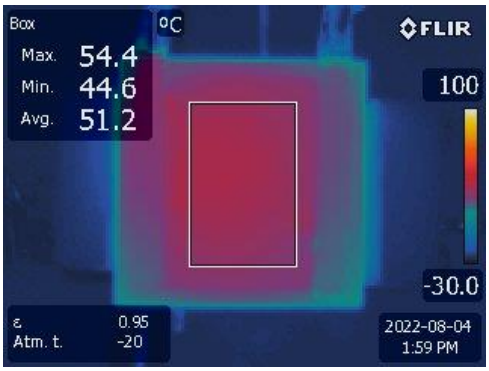

(f) After 5 minutes

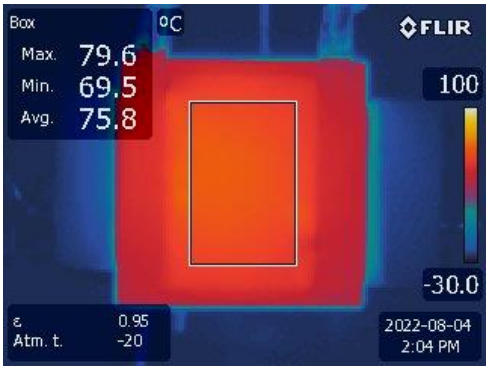

(g) After 10 minutes

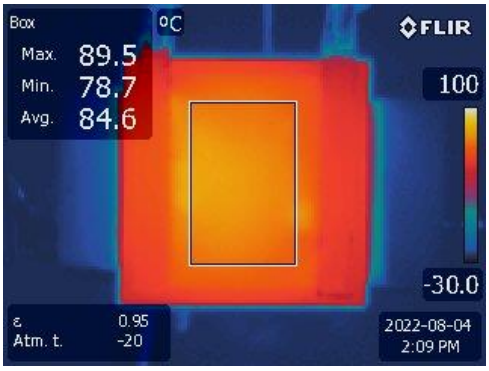

(h) After 15 minutes

Figure 42: Thermal images of the heating film when tested at an ambient temperature of -20°C with a constant current of 8 A.

Outside of the thermal camera measurement box, the temperature around the edges of the sample is lower than in the central heated region due to the rapid dissipation of heat from the edges by convection. The higher temperatures observed closer to the top of the sample are due to the closer proximity to the point of connection to the power supply [7]. Other researchers have found that the Peltier effect can affect the temperature near the electrode contacts as heat is transported parallel to the electric current due to thermoelectric interactions. The Peltier effect can cause the temperature to increase at the positive electrode and decrease at the negative electrode, although the contribution is likely small relative to the other factors mentioned [63].

4.6 Thermal Response Analysis

An analytical model of the heating and cooling processes was developed to predict the thermal response of the heating film over a wider range of environmental conditions. Similar models for thin-film heaters have been previously developed by Ji et al. (2014) and Bae et al. (2012) [56, 80]. The net heat transfer is equivalent to the energy stored in the sample and is expressed by Equation (13) as a function of the density (ρ), heat capacity (c_p), and volume (V) of the sample. The heat capacity of the coating was neglected, therefore the heat capacity of the 5 cm x 5 cm x 0.2032 cm 17-4 PH SS substrate (ρ = 7800 kg/m^3, c_p = 500 J/kg·K) dictated the transient process [81].

$$\dot{Q}_{net} = \rho c_p V \frac{dT}{dt} \tag{13}$$

The convection heat transfer rate, $\dot{Q}_{conv}$, is a function of the convection heat transfer coefficient (h_C), the surface area of the sample (A), and the environmental temperature (T_o) as shown in Equation (14). Similarly, the radiation heat transfer rate, $\dot{Q}_{rad}$, is obtained from Equation (15), where h_R is the radiation heat transfer coefficient.

$$\dot{Q}_{conv} = h_C A(T - T_o) \tag{14}$$

$$\dot{Q}_{rad} = \varepsilon\sigma A(T^4 - T_o^4) = \varepsilon\sigma A(T^2 + T_o^2)(T + T_o)(T - T_o) = h_R A(T - T_o) \tag{15}$$

The electrical heating power, convection, and radiation components are substituted into the previously shown energy balance, Equation (11), resulting in Equation (16). Since the sample is held in a stand with insulated grips during the measurement process, conductive heat transfer is neglected in this analysis.

$$\rho c_p V \frac{dT}{dt} = P_{el} - h_C A(T - T_o) - h_R A(T - T_o) \tag{16}$$

The input heating power is defined by Equation (17), which combines Equations (8) and (9) to account for the temperature dependency of the electrical resistance. An initial resistance, R_o, of 0.34 Ω was measured at the reference temperature of -20°C. As shown in Figure 43, the value for the temperature coefficient of resistance, $\alpha = 0.001\ K^{-1}$, was obtained from a linear fit of the measured resistance data for temperatures up to 100°C.

$$P_{el} = I^2 R_o(1 + \alpha(T - T_o)) \tag{17}$$

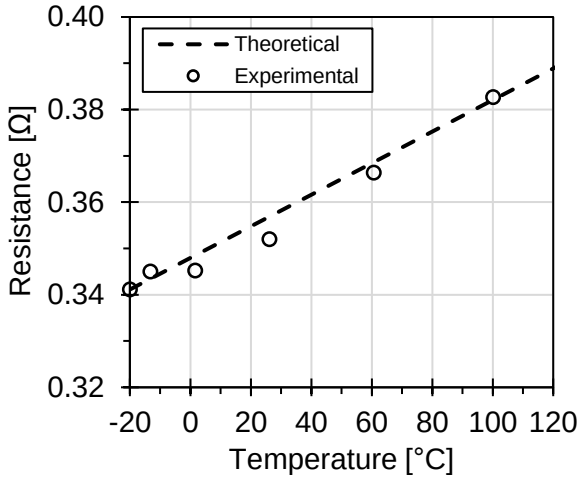

Figure 43: Experimental data showing the increase in the electrical resistance as the temperature increases. Equation (17) with $R_o = 0.34\ \Omega$ and $\alpha = 0.001\ K^{-1}$ provides a good linear fit with the experimental data.

Equation (18) combines the previous equations to define the temperature variation of the heater in the form of a first-order differential equation. Rearranging gives Equation (19), where the coefficients C_1 and C_2 are introduced to simplify solving the differential equation. The steady-state temperature, T_{ss}, can be obtained from the ratio of the coefficients C_1 and C_2 as shown in Equation (20). Solving Equation (19) results in Equation (21), the general solution for the bulk temperature, T, of the sample as a function of the heating time. Equation (22) is then obtained by substituting the expressions for T_{ss} and C_2 and simplifying. The time constant, τ_c, is given by Equation (23).

$$\rho c_p V \frac{dT}{dt} = I^2 R_o(1 - \alpha(T - T_o)) - hA(T - T_o) \tag{18}$$

$$\frac{dT}{dt} = \frac{I^2 R_o + (hA + I^2 R_o \alpha) T_o}{\rho c_p V} - \frac{hA + I^2 R_o \alpha}{\rho c_p V} T \tag{19}$$

$$where \quad C_1 = \frac{I^2 R_o + (hA + I^2 R_o \alpha) T_o}{\rho c_p V}, \qquad C_2 = \frac{hA + I^2 R_o \alpha}{\rho c_p V}$$

$$T_{ss} = \frac{C_1}{C_2} = T_o + \frac{I^2 R_o}{hA_s - I^2 R_o \alpha} \tag{20}$$

$$T = T_{ss} - (T_{ss} - T_o) e^{-C_2 t} \tag{21}$$

$$T = T_o + \frac{I^2}{hA/R_o + I^2 \alpha}\left(1 - e^{-\frac{t}{\tau_c}}\right) \tag{22}$$

$$\tau_c = \frac{\rho c_p V}{hA_s + I^2 R_o \alpha} = \frac{\rho c_p t}{h + \alpha I^2 R_o / A} \tag{23}$$

The total heat transfer coefficient, h, is expressed as the sum of the convection and radiation heat transfer coefficients ($h = h_C + h_R$). For simplicity of solving the differential equations, h was assumed to be temperature independent and was calculated at the maximum temperature for each thermal response curve [56]. For surface emissivity, ε = 1, and an ambient temperature of -20°C,

values of h_R were calculated ranging from 3.9 - 7.2 W/m^2·K depending on the input power and corresponding maximum temperature. The radiation component was found to be significant relative to the convection component, thus it was included in the analysis.

The convection heat transfer coefficient was estimated from Equation (24), considering free convection for a horizontal flat plate, where k is the thermal conductivity of air and L is the characteristic length. The correlations for the Nusselt number, $\overline{Nu}_L$, for the upper and lower surfaces of the hot plate are given by Equations (25) and (26) respectively [82]. The Rayleigh number, Ra, is calculated by Equation (27), where g is the acceleration due to gravity and the properties of the fluid include the volumetric thermal expansion coefficient (β), thermal diffusivity (κ), and kinematic viscosity (ν). The calculated values of h_C ranged from 7.5 - 14.4 W/m^2·K, again depending on the maximum temperature for each test. Adding the radiation and convection components yielded total heat transfer coefficients ranging from 19 – 36 W/m^2·K.

$$h_c = \frac{\overline{Nu}_L k}{L} \tag{24}$$

$$\overline{Nu}_L = 0.54 Ra_L^{1/4} \tag{25}$$

$$\overline{Nu}_L = 0.52 Ra_L^{1/5} \tag{26}$$

$$Ra = \frac{g\beta(T - T_o)L^3}{\kappa\nu} \tag{27}$$

As shown in Figure 44, the calculated values of h agreed well with the cooling process, but consistently underestimated the heat loss during the heating process. The difference between the values of h during the heating and cooling processes can be attributed to the effect of the temperature-dependent resistance [56]. For the heating process, the values of h were instead estimated by fitting the model curves to the experimental data. From this process, values of h

ranging from 33 – 41 W/m^2·K were extracted for the heating process, while the previously calculated values of 19 – 36 W/m^2·K still agreed with the cooling data. As shown in Figure 45, the resulting model now provides a good fit with the experimental data for both the heating and cooling processes. The values of h extracted in this work align well with the values of 32 W/m^2·K obtained by Ji et al. (2014) and 53 W/m^2·K reported by Bae et al. (2012) for silver-based heating films on glass substrates when considering the difference in substrate material and thickness, and the environmental conditions during testing [56, 80].

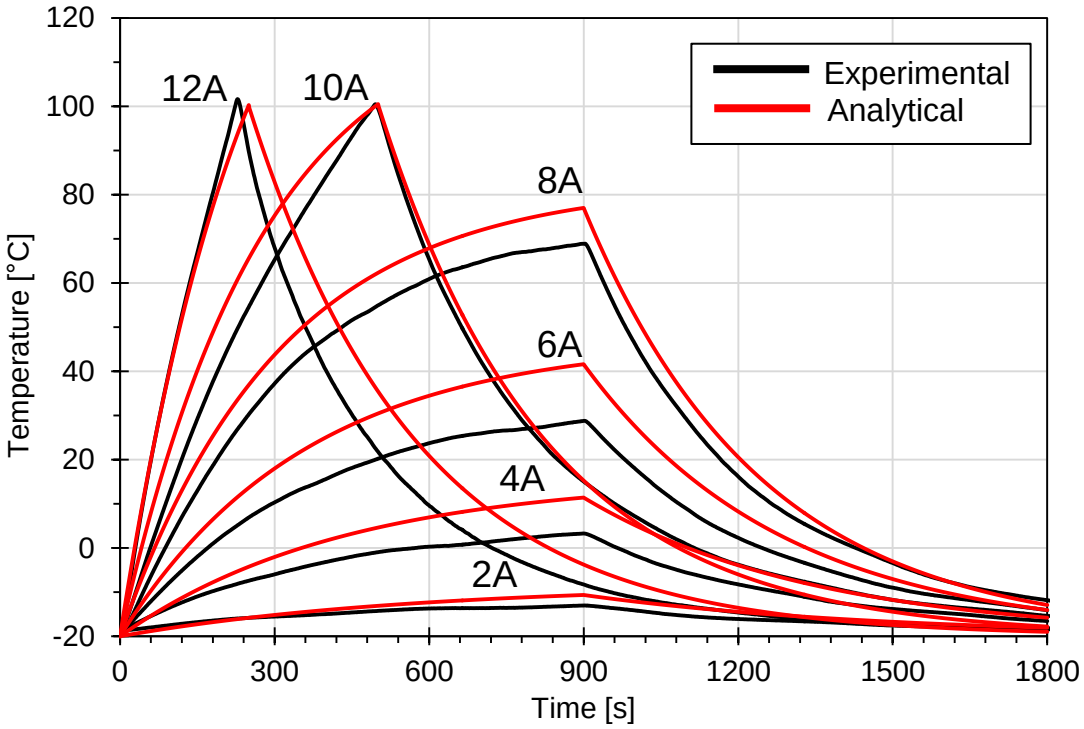

Figure 44: Comparison between the experimental thermal response data and the response predicted by the analytical model for 2-12A input current where h = 19 – 36 W/m^2·K was calculated by estimating the radiative and convective heat loss.

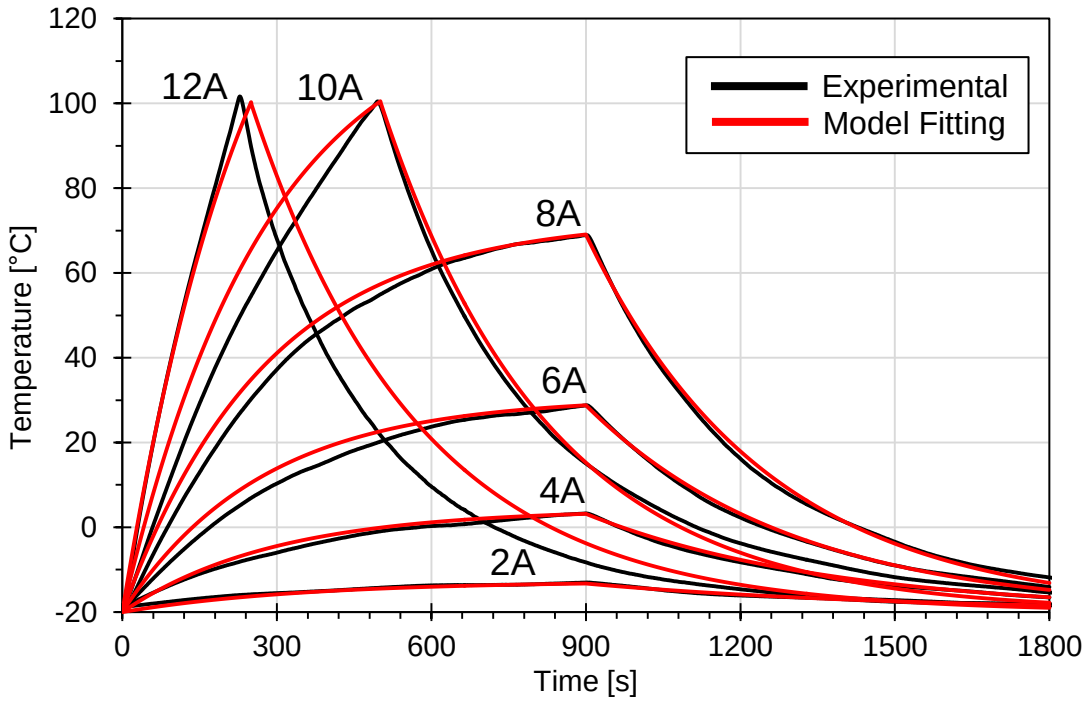

Figure 45: Comparison between the experimental and analytical thermal response data after fitting the model values of h to the experimental curves for heating process. For input current from 2 – 12 A, values of h from 33 – 41 W/m^2·K provided a good fit for the heating process. The previously calculated values of h = 19 – 36 W/m^2·K still aligned well with the cooling process.

4.7 Summary

In this chapter, each step of the fabrication process of the hybrid coating was explained in detail. A static contact angle of 164.3° and CAH of 2.8° were measured on the SiO_2/PDMS coating, which confirmed its superhydrophobicity. Further investigation with high-speed imaging found that the superhydrophobic coating had a sliding angle of 3°. Droplets were also observed completely rebounding after impact and easily rolled off of the superhydrophobic surface when placed at a small incline. SEM micrographs confirmed the presence of the hierarchical micro-nanostructure that was composed of stacked agglomerations of SiO_2 nanoparticles bound together by the PDMS adhesive.

The key electrothermal properties of the heating film were quantified. The heating film was shown to possess a fast thermal response time and good thermal stability. The heating element had a

nominal resistance of 0.34 Ω. The thermal response was recorded with a constant input current ranging from 2 – 12 A. The maximum input current corresponded to a power density of 4.28 W/cm^2, which produced a 60°C temperature rise in just 52 seconds. Thermal cycling tests showed no degradation in the maximum attainable temperature with an 8 A input over 3-hours and the infrared images verified the uniformity of the temperature distribution throughout the heating process. Finally, the heating and cooling processes were modelled to fit the experimental data and predict the thermal response behaviour over a wider range of environmental conditions. The analytical model aligned well with the experimental data for 2 – 12 A, with values of h ranging from 33 – 41 W/m^2·K for the heating process and 19 – 36 W/m^2·K for the cooling process.

CHAPTER 5

Icing Experimental Results

5.1 Ice Adhesion Strength

The ice adhesion strength (IAS) was measured following the procedure described in Section 3.3.4 and the resulting data is presented in Figure 46.

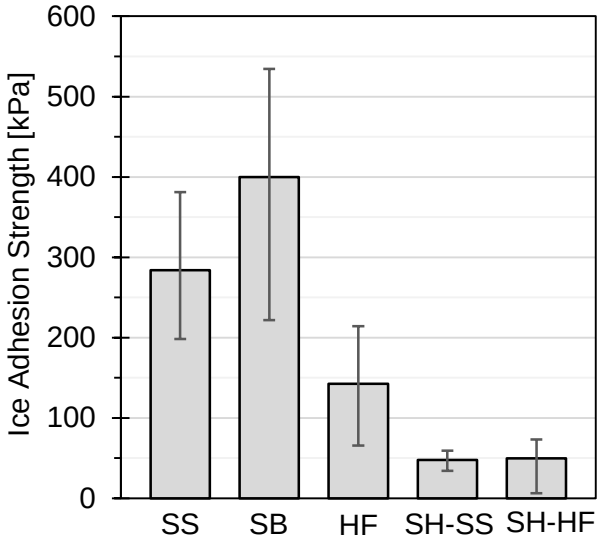

Figure 46: Measured ice adhesion strength on each of the sample surfaces.

The IAS on the untreated SS sample was measured as 284 ± 91 kPa. The IAS increased to 400 ± 156 kPa on the sandblasted SS sample due to mechanical interlocking between the ice and the surface roughness. The IAS decreased to 143 ± 71 kPa on the HF sample (without power input). In this case, the smooth surface finish, low surface energy, and high elasticity of the PDMS topcoat are responsible for the reduction in the IAS. The model proposed by Wang et al. shows that ice can be removed under less force from an elastomer than a rigid material [71]. Ice has a high elastic modulus (~ 10 GPa) that is several orders of magnitude higher than that of the PDMS elastomer (7.3 MPa). This difference in moduli results in an uneven concentration of stress along the ice-solid interface plane when the ice is subjected to a removal force. The stress concentration caused by the elastic deformation of the soft coating material allows for easier ice removal. On the SH-

SS and SH-HF samples, the IAS was measured as 48 ± 12 kPa and 50 ± 34 kPa respectively. In static de-icing conditions, the superhydrophobic coating effectively reduced the IAS by 83% compared to the base metal substrate. Icephobic surfaces are typically defined by an ice adhesion strength of less than 100 kPa, therefore, both of the superhydrophobic-coated samples can be considered icephobic [52].

There is a relatively large variance in the measured IAS values across due to several difficult-to-control factors which can significantly influence the results, including cooling rate, probe impact speed, and surface roughness at the location of measurement. Randomness in the crystallization process can also produce flaws and stress concentrations which make it challenging to produce repeatable results. Results in the literature show that measured IAS values are expected to vary by ± 25 % even when all experimental parameters are held constant [52]. A one-sample t-test was used to determine if the increase in the IAS on the sandblasted sample due to the increased surface roughness was significant when compared to the untreated substrate. A p-value of 0.02 was calculated from the measured data. Therefore, it can be concluded that the increase in the ice adhesion strength due to the increase in surface roughness was significant. The same analysis was performed for the coated samples to confirm the significance of the decrease in the IAS. For the HF, SH-SS, and SH-HF samples, $p << 0.01$, therefore the decrease in the IAS due to the coating process is determined to be highly significant.

Figure 47 (a) plots the IAS against the static contact angle, in which no clear correlation is observed. If the IAS is instead plotted against the CAH, as shown in Figure 47 (b), a linear trend becomes apparent. This result is consistent with published observations that the IAS tends to decrease for surfaces with low CAH [83]. The relationship between ice adhesion and CAH can be explained by the effect of surface roughness on the contact area. As previously discussed in Section

2.2, high CAH is typically associated with wetting in the Wenzel state and low CAH in the Cassie-Baxter state. In the Wenzel state, the liquid that has penetrated the surface roughness increases the ice-solid contact area after freezing. Hence, the ice-solid contact area becomes larger than the projected area and results in higher IAS on the rough surface than for an equivalent smooth surface. Moreover, in the Wenzel state mechanical interlocking can occur between the ice and surface roughness which adds to the force required to break the ice away from the surface. In the Cassie-Baxter state, the air pockets persist through the freezing process and reduce the ice-solid contact area, resulting in a lower IAS, as evidenced by the results on the superhydrophobic samples.

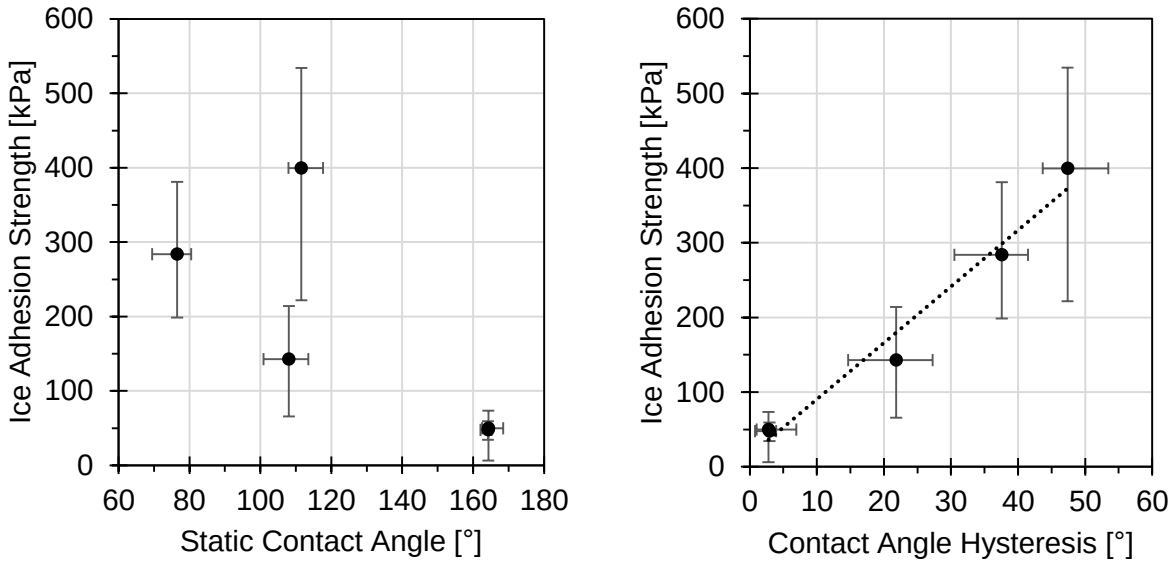

Figure 47: Relationships between the ice adhesion strength and the static contact angle and contact angle hysteresis.

When power was supplied to the heating element the removal force was too low to be measured by the probe (< 0.1 N) after the interfacial layer of ice had been melted. The thin layer of liquid water that was generated from the melting ice resulted in ultra-low ice adhesion strength, allowing ice to be removed by a small external force, such as gravity, wind, or vibration [52]. De-icing tests with electro-thermal heating are investigated further in Section 5.4.

5.2 Droplet Freezing Time

The anti-icing properties were investigated experimentally by measuring the freezing time on each of the sample surfaces. The experiments were performed in a cold chamber at -20 ± 1°C and a syringe pump was used to control the dosing of chilled de-ionized water. Sessile droplets (15 μL) were placed onto the sample surfaces and the freezing time was measured from the point of impact until the droplet had completely frozen. The freezing time was averaged across results for 25 droplets on each sample. As shown in Figure 48, on untreated stainless steel the freezing process initiates approximately 3 seconds after the droplet impact and freezing was complete in 8 seconds. On the sandblasted sample the freezing time was slightly longer, starting at 6 s and completing after 16 s. On HF (without heating power), freezing started at 18 s and concluded at 32 s. The freezing time was similar on SH-SS, where freezing began after 12 s and completed after 31 s. A large increase in the freezing time was observed on SH-HF. Freezing started after 50 seconds and finished after 76 seconds on the hybrid coating. Comparing the results, a maximum freezing delay of 68 seconds was achieved and the freezing time was over 9 times longer on SH-HF than on the untreated substrate. As discussed in Section 2.4, the extended freezing time on HF is mainly due to the low thermal conductivity of PDMS, while the low thermal resistance of the superhydrophobic coating is responsible for delaying the freezing process on SH-SS. On the hybrid coating, the thermal resistances of HF and SH-SS are effectively added together which results in the freezing process taking approximately twice as long on SH-HF.

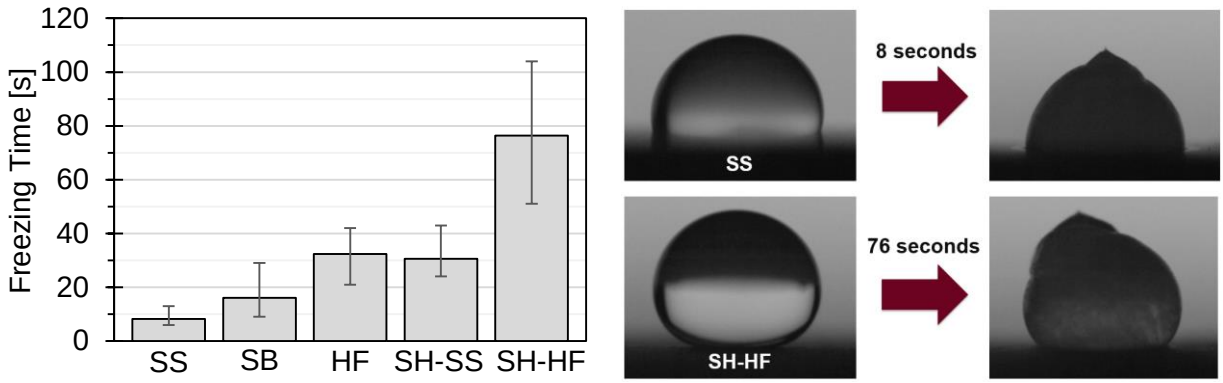

Figure 48: Freezing time measurements on each sample and photographs of droplets before and after freezing.

During the experiments, it was noticed that two different freezing mechanisms occurred for droplets on the superhydrophobic samples. While most droplets froze within approximately 90 seconds as expected, a few droplets were observed to remain on the surface for over 20 minutes without freezing. These droplets were considered outliers and thus were excluded from the data presented in Figure 48. However, the outlier behaviour can be explained by the mechanism which drives the ice nucleation process. Contact freezing is a type of heterogeneous nucleation which occurs at the liquid-solid interface. The presence of the surface lowers the ice nucleation barrier by providing nucleation sites for ice crystals to form. Therefore, the heterogeneous freezing temperature is relatively high for contact freezing. For static droplets with a high contact angle, the solid-liquid contact area may be small enough that no viable nucleation site exists at the interface. In this case, homogenous nucleation can occur within the volume of the droplet. Homogenous nucleation has a higher ice nucleation barrier and therefore water may remain in the liquid state at temperatures below the freezing point. In laboratory conditions, highly pure water can be supercooled by more than 35°C before freezing spontaneously. When the temperature is low enough the droplet will nucleate and freeze nearly simultaneously [84, 85, 86]. Therefore, heterogeneous nucleation is likely the mechanism responsible for the droplets freezing within 60 seconds, while the droplets that remained on the surface for several minutes were supercooled until

the threshold for homogenous nucleation was reached. The distinct nucleation processes present a likely explanation for the two different freezing behaviours observed on the same superhydrophobic surface. The minimal droplet-surface interactions due to the high water contact angle promote homogenous nucleation. Homogenous nucleation is also more likely to occur due to the low concentration of impurities in the de-ionized water used in the experiment. It was also observed that disturbing the supercooled droplet or tilting the surface would initiate the nucleation process and freezing would occur nearly instantly.

A limitation of this experiment was that the cold chamber used did not have an adequate viewing window to capture the freezing process with a high-speed camera. Since the freezing process could only be observed with the naked eye, the onset of freezing, formation of initial ice nuclei, and end of propagation could only be estimated. Without high-speed footage, it was not possible to accurately determine the freezing propagation velocity or confirm the predicted nucleation behaviour. However, as others have stated, the freezing time of a single static drop is not a good measure of the anti-icing performance of a surface in practice [85]. In a real environment, there is continual impingement of droplets which tend to roll, collide, and merge. Since these dynamic factors can influence the freezing time, the continuous water spray method is expected to provide a more realistic indicator of the anti-icing ability of the coating.

5.3 Anti-icing Experimental Results

The results of the spray icing tests on the SS and SH-SS samples are shown in Figure 49. The spray icing test on the untreated SS sample resulted in the rapid accumulation of a 5 mm-thick layer of ice. During the experiment, ice accumulation was observed to be delayed by about 1 minute on SH-SS. Instead of accumulating in a uniform layer, the ice formed from the pinning points where very small droplets stuck to the surface and froze. After the first ice had formed on the SH-SS

surface, ice quickly accumulated around the initial freezing sites for the remainder of the test. The superhydrophobic coating could not stop icing completely, however, the total ice accumulation was less than on the untreated substrate. The partial coverage and preservation of the spherical droplet shape were qualitatively observed to facilitate ice removal from SH-SS, consistent with the ice adhesion strength results presented in Section 5.1.

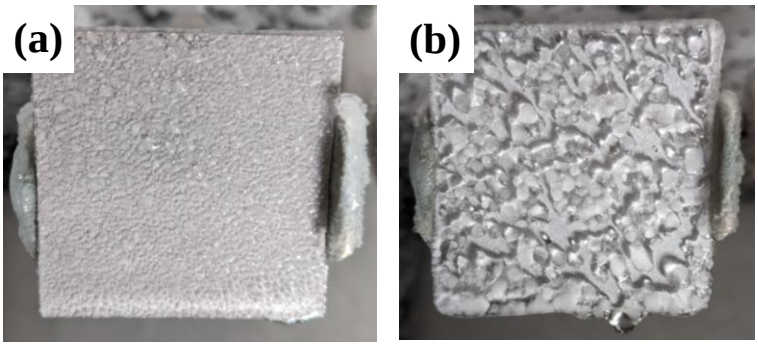

Figure 49: Ice accumulation on (a) SS and (b) SH-SS after being sprayed with a water mist for 150 s at -20°C.

The results of the active anti-icing tests with electrothermal heating are presented in Figure 50 with the heated area denoted by the red outline. The input power was varied to determine the minimum surface power density required for complete anti-icing of the heated area. Ice readily accumulated on both samples with no electrothermal heating. With a power density of 0.19 W/cm^2, the iced area was significantly lesser on SH-HF, while the same power density had minimal effect on the iced area of HF. Increasing the power density to 0.26 W/cm^2 was sufficient for the anti-icing of the heated area on SH-HF. Minor ice accumulation was still observed on the electrodes and edges of the sample. Significant droplet pinning was also observed within the heated area, although the heating power was sufficient to keep the pinned droplets from freezing. Anti-icing of the heated area on HF was achieved with a power density of 0.44 W/cm^2. At the same power density, SH-HF demonstrated complete anti-icing with no ice accumulation around the edges and minimal droplet pinning.

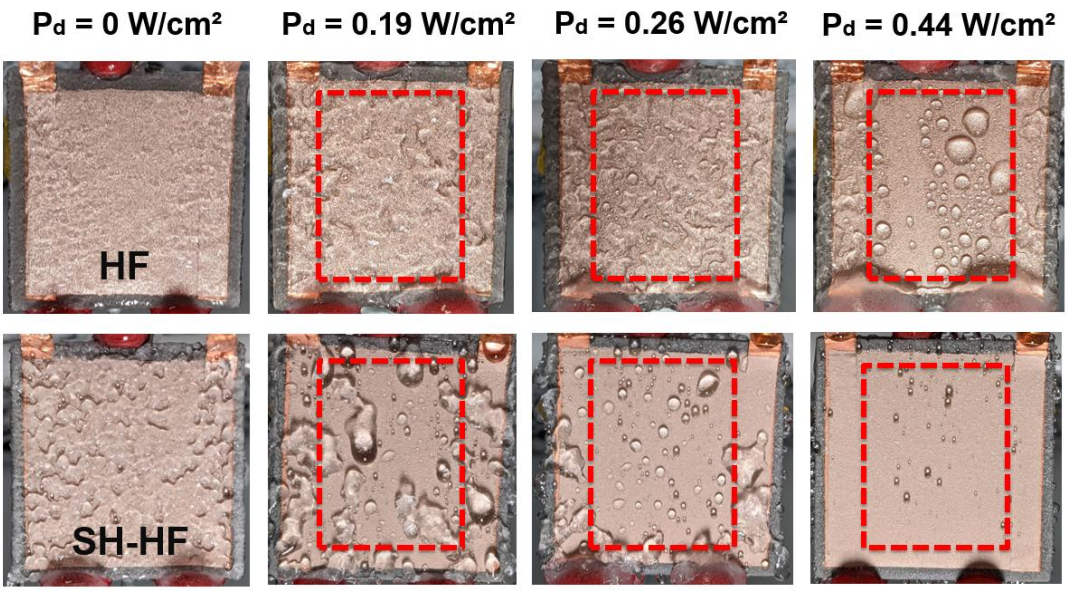

Figure 50: Results of the anti-icing tests comparing HF and SH-HF samples under spray-icing conditions. The heated area is denoted by the dashed red outline. SH-HF required 0.26 W/cm² for complete anti-icing of the heated area, while HF required 0.44 W/cm² to achieve the same result.

Comparing the minimum surface power densities for anti-icing of 0.44 W/cm^2 for HF and 0.26 W/cm^2 for SH-HF, it can be concluded that the energy consumption is reduced by 41% on SH-HF. The passive superhydrophobic coating contributes a significant energy reduction which is attributed to a portion of water running off of the surface before freezing. This reduces the amount of energy that is conducted into standing water on the surface, as well as the energy expended overcoming the latent heat of fusion to melt accumulated ice. The results show that SH-HF is capable of energy-efficient anti-icing and demonstrates the effectiveness of the hybrid superhydrophobic – electrothermal method for ice protection.

5.4 De-icing Experimental Results

The results of the de-icing tests with electrothermal heating are presented in Figure 52 for the HF and SH-HF samples. Tests were carried out with surface power density ranging from 0.3 W/cm^2 to 2.9 W/cm^2. At an initial temperature of -20 ± 1°C, the minimum de-icing power density was 0.7 W/cm^2 for HF and 0.9 W/cm^2 for SH-HF. The results showed a continual reduction in the de-icing

time as the power density was increased. With the maximum power density of 2.9 W/cm^2, the de-icing time was 92 seconds and 114 seconds for the HF and SH-HF respectively. The average surface temperature at the point of de-icing was 6°C. Images showing the experimental setup and the samples before and after de-icing are presented in Figure 51.

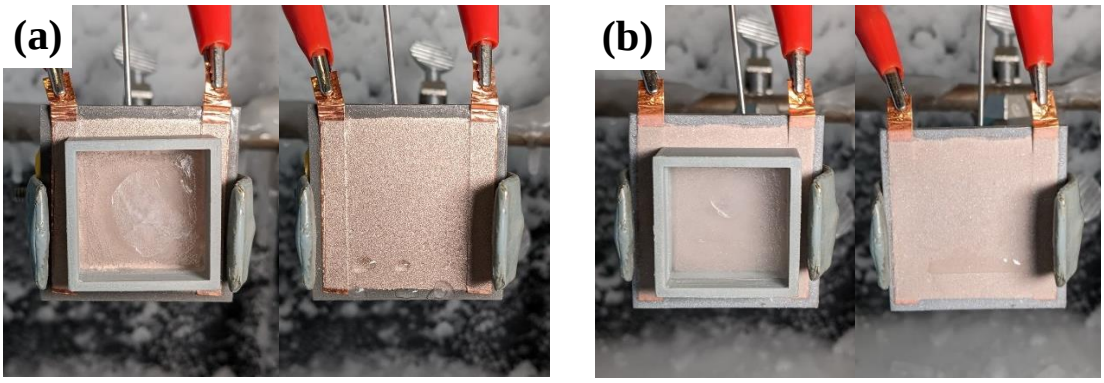

Figure 51: (a) HF and (b) SH-HF before and after de-icing.

For ice to be released from the surface by gravity, the ice adhesion strength must be exceeded. The combined weight of the ice and the 3 cm x 3 cm mold corresponds to a critical ice adhesion strength of 1.0 kPa. This is significantly lower than the previously recorded ice adhesion strength values for either sample, therefore, the interfacial layer of ice must be melted for de-icing to be realized. The de-icing time is highly dependent on the efficiency of the heat transfer between the heating element and the ice. Comparing the thermal resistance of the coatings on each of the two samples, HF has a lower thermal resistance than SH-HF and therefore is expected to have a shorter de-icing time. The additional thickness of the superhydrophobic coating layer and interfacial air pockets cause SH-HF to have a higher thermal resistance and a longer de-icing time. As previously discussed, the insulating effect of the air cushion is beneficial to extend the freezing time. However, the same phenomenon hinders the de-icing performance after ice has collected on the surface. The effect of the thermal resistance of the coating becomes especially noticeable with low

power density. As the power density increases, the difference in the freezing time between the two samples becomes less noticeable.

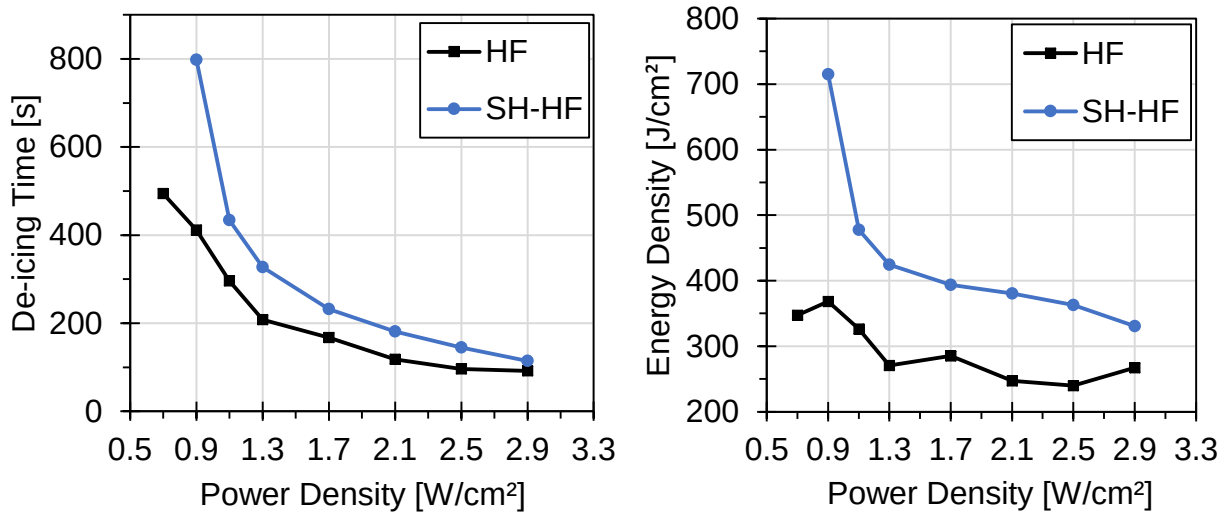

Figure 52: Results of de-icing experiments showing the de-icing time (left) and energy density (right) for varying power density for both HF and SH-HF.

When compared with the previous anti-icing results, it is clear that higher power density is necessary for de-icing than for anti-icing. However, since power is only supplied intermittently for de-icing, the total energy consumption is comparable. The energy density, Q_d, can be obtained by Equation (28), where the surface power density (P_d) is multiplied by the time (t) that the power must be sustained for de-icing [57].

$$Q_d = P_d \cdot t \tag{28}$$

The energy density is an indicator of the heating efficiency at each operating point. As shown in Figure 52, for low power density the energy density is high because more heat energy is wasted as it diffuses into the ice and substrate. Increasing the power density concentrates heating at the ice-solid interface and reduces the heat loss to the environment, as shown by the reduction in energy density as power density increases.

De-icing with a pulse heating scheme was tested to determine if the efficiency could be improved further as described by Petrenko et al. [57]. Power was supplied to the heating film in short 0.3s pulses. Since power is only applied 50% of the time, the power density is effectively halved. Pulse heating is expected to limit the thermal penetration depth to achieve a greater concentration of heat at the ice-solid interface. Therefore, it should be expected that the de-icing time and energy density will be less than twice that of continuous heating with the same power density. In the initial tests, a minor decrease in the de-icing temperature was observed, suggesting that less energy was wasted heating the substrate. However, no significant reduction in the de-icing time with pulse heating was observed when compared to de-icing time with continuous heating at half the power density. The energy-saving benefit of pulse heating was not as pronounced as expected in this case. This is attributed to the low thermal conductivity of the outer PDMS and superhydrophobic coating layers which reduced the thermal penetration depth and prevented the desired concentrated heating at the ice-solid interface. From the results presented, it can be concluded that SH-HF performs better when operating in an anti-icing mode than in a de-icing mode. Therefore, it is more efficient to prevent ice accretion altogether than to allow ice to build up and de-ice the surface intermittently.

5.5 Coating Durability

Although the anti-icing capabilities of the hybrid coating have been demonstrated, durability is also a critical factor to consider for practical applications. The durability of the fabricated coatings was investigated experimentally by testing its ability to withstand light abrasion and repeated icing and de-icing cycles. The change in the static contact angle was recorded between cycles to evaluate the ability of the coating to withstand harsh environmental conditions.

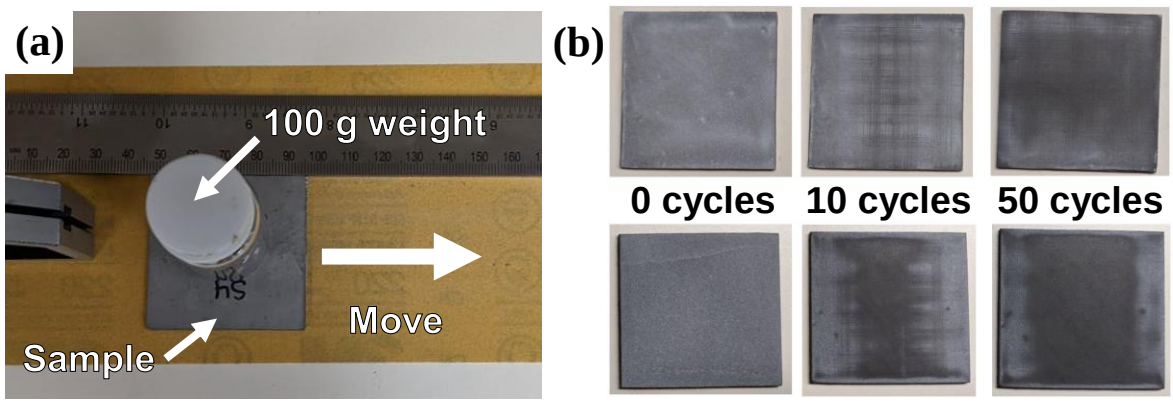

Figure 53: (a) Sandpaper abrasion test setup with the SH-SS sample under a 100 g weight; (b) The SH-SS (top) and SH-HF (bottom) samples before and after 10 and 50 abrasion cycles.

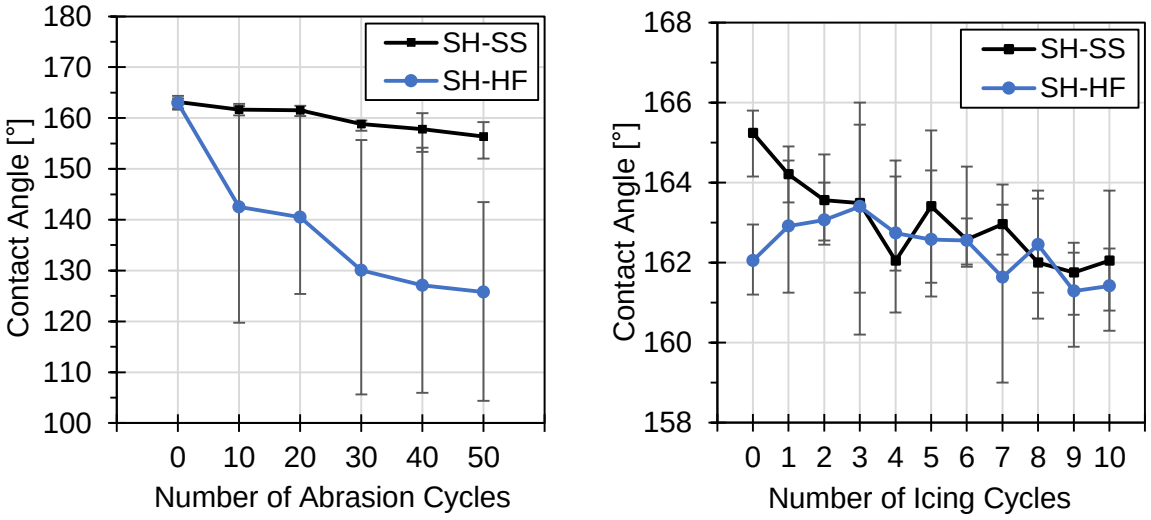

Figure 54: Change in static contact angle on the SH-SS and SH-HF samples across abrasion and freeze/thaw cycles.

The sandpaper abrasion test is the most widely used method to assess mechanical durability and wear resistance [6, 27]. The abrasion distance, applied normal pressure, and sandpaper grit are key factors influencing the harshness of the abrasion [6]. In this work, each sample was placed under a 100 g weight and pushed a distance of 10 cm over #220 grit sandpaper. The sample was rotated 90° after each cycle to evenly abrade the whole surface. The static contact angle was measured every 10 cycles up to a total of 50 cycles. The test setup and images of the samples before and after abrasion are shown in Figure 53.

The results of the sandpaper abrasion test are displayed in Figure 54. The contact angle on the SH-SS sample gradually decreased from 163° to 156° after 50 abrasion cycles. The coating retained its superhydrophobicity after 50 abrasion cycles, demonstrating excellent mechanical durability. The high durability can be attributed to the strong bond between the PDMS adhesive and stainless steel substrate, as well as the retention of superhydrophobic material within the surface roughness features created by sandblasting. SEM images of the SH-SS sample after 50 abrasion cycles are shown in Figure 55. Compared with the original microstructure in Figure 35 (c), it is clear that the microstructure was degraded and significantly altered by the abrasion process. However, a significant amount of the superhydrophobic material remained on the surface within the valleys created by the sandblasting process. The coating was completely removed from the sandblasted peaks and the underlying stainless steel was exposed in these areas. The delicate SiO_2 nanoparticle agglomerations that made up the original surface structure were largely destroyed. The remaining microstructure consisted of SiO_2-embedded PDMS with porous features resulting from the voids that remained after the larger agglomerations were broken off by the abrasion process.

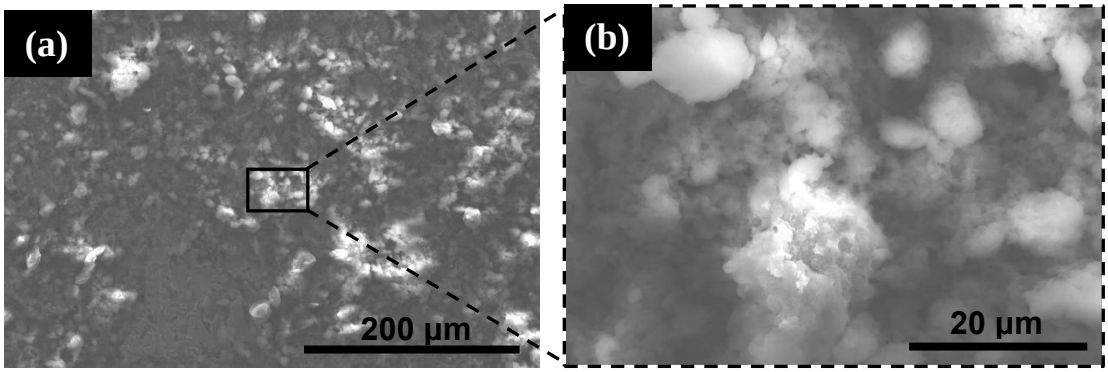

Figure 55: SEM images of the SH-SS sample after 50 abrasion cycles; (a) 600x magnification, (b) 5000x magnification.

Conversely, the mechanical durability of the SH-HF sample was revealed to be poor in comparison. After 50 abrasion cycles, the average contact angle on the SH-HF sample decreased from 163° to 126°. Furthermore, the SH-HF surface had large variations in the measured contact

angle depending on the area on the sample where the liquid droplet was placed. The contact angle was lowest in the center of the sample which was most heavily abraded. Here, the contact angle was reduced to less than 150° after just 10 cycles and approached the contact angle of the underlying smooth PDMS (~108°) after 30 cycles. The edges of the sample were not as heavily abraded and thus demonstrated higher contact angles throughout the test. The PDMS–PDMS adhesion was observed to be noticeably weaker than the adhesion to the stainless steel substrate. In addition, the smooth surface of the heating film allowed the coating to be scraped off relatively easily compared to the rough, sandblasted surface of SH-SS. It should also be noted that the top layer of PDMS completely protected the heating element and the performance of the heater was completely unaffected by the abrasion. Furthermore, the superhydrophobic top-coating was found to be easily repairable after it was damaged by abrasion. Since the underlying PDMS layer remained fully intact, the sample was wiped clean with ethanol to remove any debris and then the superhydrophobic coating was able to be easily reapplied using the same process as before.

The durability of the coating was further investigated by subjecting both samples to repeated icing and de-icing cycles. For each cycle, a 3 cm x 3 cm mold was placed in the center of the sample and then filled with 5 mL of pre-cooled de-ionized water. The sample and mold were placed in a cold chamber at -6°C for 2 hours until the water had completely frozen. The sample was removed from the cold chamber and thawed at room temperature until the ice melted. The process was repeated for 10 cycles and the static contact angle was measured between each cycle.

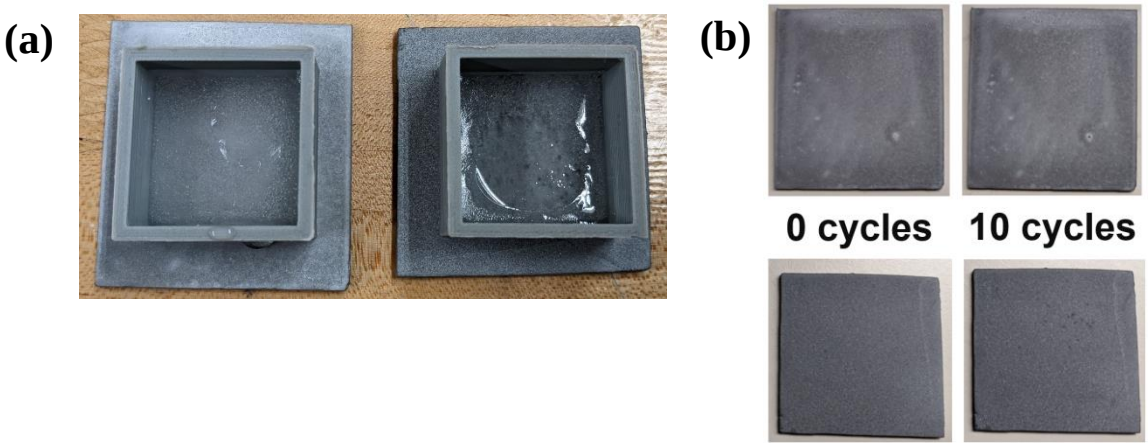

Figure 56: (a) Ice frozen in 3 x 3 cm mold on each of the sample surfaces. (b) Images of SH-SS (top) and SH-HF (bottom) before and after being subjected to 10 icing cycles.

Images of the samples before and after 10 icing cycles are shown in Figure 56. The change in contact angle after each icing/de-icing cycle throughout the test is shown in Figure 54. No substantial change was recorded in the contact angle after 10 cycles, with both samples retaining their superhydrophobicity. The contact angle gradually decreased from approximately 165° to 162° and 162° to 161° on the SH-SS and SH-HF samples respectively. This suggests that the icing/de-icing process did not cause significant damage to the surface structure of the SiO_2/PDMS superhydrophobic coating.

5.6 Summary

The icing tests carried out in this chapter effectively demonstrated the anti-icing and de-icing capabilities of the fabricated samples and exemplified the high efficiency of the hybrid superhydrophobic-electrothermal method.

When compared with the untreated substrate, the ice adhesion strength was reduced by 83% to only 50 kPa on SH-HF. The superhydrophobic coating also contributed to a significant delay in the droplet freezing process, increasing the freezing time from 8 seconds to 76 seconds. Under a continuous water spray, anti-icing was achieved with a minimum power density of 0.26 W/cm^2 on

SH-HF. When compared with HF alone, the superhydrophobic coating reduced the energy consumption for anti-icing by 41%. With a power density of 2.9 W/cm^2, a 5 mm thick layer of ice was removed from the surface of SH-HF in 114 seconds. However, the high thermal resistance of the superhydrophobic coating was found to negatively affect the de-icing performance. Therefore, anti-icing should be the primary purpose of the hybrid coating such that energy efficiency is maximized.

The durability of the superhydrophobic coating was evaluated under sandpaper abrasion and repeated icing/de-icing tests. SH-SS possessed excellent abrasion resistance, with the contact angle only decreasing from 163° to 156° after 50 abrasion cycles. However, the abrasion resistance of SH-HF was comparatively poor since the contact angle fell below 150° after 10 cycles and dropped to 126° after 50 cycles. SH-SS and SH-HF both showed good durability to repeated icing and de-icing cycles. The contact angle remained above 160° on both samples after being subjected to 10 icing cycles.

CHAPTER 6

Conclusions and Recommendations for Future Work

6.1 Conclusions

Icing presents serious safety and operational hazards to marine vessels and offshore structures in cold environments. Consequently, a growing need was identified for robust and energy-efficient ice protection methods as vessel traffic continues to increase in arctic and sub-arctic regions.

In this thesis, a hybrid anti-icing coating with superhydrophobic and electrothermal properties was successfully developed. The coating was applied to 17-4 PH SS substrates using a simple multi-layered spray-coating process. The heating film was effectually applied to the metallic substrate by insulating the Ag-Cu epoxy-based heating element between two layers of PDMS. The superhydrophobic coating was fabricated from hydrophobically-modified SiO_2 nanoparticles dispersed in a PDMS matrix. Combining a thin film heater with a superhydrophobic top-coating resulted in an effective and energy-efficient hybrid anti-icing solution.

Characterization of the heating film's electrothermal properties revealed a fast thermal response time and stable, uniform heating performance over time. The results showed that a temperature rise of 30°C could be generated in just 45 seconds with an input current of 12 A. An investigation of the surface wettability confirmed the superhydrophobic properties of the SiO_2/PDMS coating which possessed a static contact angle of 164.3° and contact angle hysteresis of 2.8°. High-speed video footage captured droplets completely rebounding from the superhydrophobic surface after impact and sliding when the sample was tilted at an angle of 3°. SEM micrographs were taken to characterize the micro-nanoscale roughness that is responsible for the observed superhydrophobic behaviour. The micro-nanostructure was composed of hierarchical agglomerations of SiO_2 nanoparticles cohered by PDMS.

The anti-icing properties of the hybrid coating were shown experimentally through the reduction in the ice adhesion strength, delayed droplet freezing time, and high energy efficiency in dynamic icing tests. Due to the reduced contact area at the ice-solid interface, the ice adhesion strength was decreased from 284 kPa on the untreated substrate to 50 kPa on SH-HF, corresponding to an 83% reduction. The high thermal resistance of SH-HF was found to be responsible for delaying the freezing process. The droplet freezing time was delayed from 8 seconds to 76 seconds on SH-HF when compared with the untreated stainless steel. Dynamic anti-icing tests in a simulated spray icing environment showed that SH-HF was able to achieve complete anti-icing with a power density of 0.26 W/cm^2. Since a portion of the water droplets were able to roll off of the surface before freezing, the superhydrophobic coating reduced the energy consumption of the heating film by 41% when compared to the untreated HF.

Finally, the durability of the superhydrophobic coating was evaluated under sandpaper abrasion and repeated icing/de-icing tests. SH-HF showed relatively weak abrasion resistance but the superhydrophobicity was easily restored by simply reapplying the superhydrophobic top-coating. SH-HF demonstrated strong durability under repeated icing and de-icing cycles where the contact angle was maintained above 160° after 10 icing/deicing cycles.

In conclusion, the energy-efficient anti-icing capabilities of the hybrid superhydrophobic-electrothermal coating have been demonstrated. The results, along with the simple and versatile fabrication process, make SH-HF a promising option for potential future applications in the marine and offshore industries.

6.2 Recommendations for Future Work

The hybrid anti-icing coating has shown promising results in the tests conducted thus far, however further studies are necessary for implementation in practical applications. Several suggestions for future research related to the work presented in this thesis are listed as follows:

- For marine applications, the corrosion resistance of the coating will require thorough investigation and testing in the future.
- The scalability of the heating film to large surface areas or complex geometry is of interest for future investigation. For large surface areas, the heating film may need to be divided into several distinct elements for better control over the thermal properties.
- Application to other substrate materials such as aluminum, carbon steel, glass, plastics and composites may also be of interest for future investigation.
- The Ag/Cu epoxy heating element could be substituted with an optically transparent and conductive material such as indium tin oxide (ITO) for application to glass surfaces such as windows and windshields.
- The abrasion resistance of the SH-HF may be improved by texturing the underlying PDMS surface through processes such as chemical etching [87]. The surface roughness created by these processes could potentially improve the retention of the SiO_2 nanoparticles in the surface structure, similar to the retention of superhydrophobic material within the sandblasted valleys observed for the SH-SS sample.
- Due to the nature of the manual spray-coating process, it is challenging to produce the specified layer thicknesses and a consistent surface finish. Employing an automated spray-coating system would greatly improve the consistency and repeatability of the fabrication process and give precise control over the layer thickness.

- Reducing the thermal resistance may improve the effectiveness of pulse heating for de-icing. This can be achieved by minimizing the thickness of the top layer of PDMS insulation or investigating alternative materials with higher thermal conductivity.
- Larger scale anti-icing tests can be conducted in the future using the cold room facility. Since the cold chamber used in this study was relatively small, the water spray could only be sustained for a short time before the chamber temperature started to approach 0°C.

REFERENCES

[1] Protection of the Arctic Marine Environment (PAME), "Arctic Shipping Status Report #1," 31 March 2020. [Online]. Available: https://www.pame.is/document-library/pame-reports-new/pame-ministerial-deliverables/2021-12th-arctic-council-ministerial-meeting-reykjavik-iceland/793-assr-1-the-increase-in-arctic-shipping-2013-2019/file.

[2] C. C. Ryerson, "Ice Protection of Offshore Platforms," *Cold Regions Science and Technology,* vol. 65, pp. 97-110, 2011.

[3] K. Shi and X. Duan, "A Review of Ice Protection Techniques for Structures in the Arctic and Offshore Harsh Environments," Memorial University of Newfoundland, St. John's, NL, 2021.

[4] C. Antonini, M. Innocenti, T. Horn, M. Marengo and A. Amirfazli, "Understanding the effect of superhydrophobic coatings on energy reduction in anti-icing systems," *Cold Regions Science and Technology,* vol. 67, pp. 58-67, 2011.

[5] Z. Zhao, H. Chen, X. Liu, H. Liu and D. Zhang, "Development of a high-efficient synthetic electric heating coating for anti-icing/de-icing," *Surface & Coatings Technology,* vol. 349, pp. 340-346, 2018.

[6] Y. Peng, J. Hu, Z. Fan, P. Xie, J. Wang and P. Wang, "A stretchable superhydrophobic coating with electrothermal ability for anti-icing application," *Materials Research Express,* vol. 8, no. 045009, 2021.

[7] Z. Zhao, H. Chen, X. Liu, Z. Wang, Y. Zhu and Y. Zhou, "Novel sandwich structural electric heating coating for anti-icing/de-icing on complex surfaces," *Surface & Coatings Technology,* vol. 404, no. 126489, 202.

[8] X. Liu, H. Chen, Z. Zhao, Y. Yan and D. Zhang, "Slippery liquid-infused porous electric heating coating for anti-icing and de-icing applications," *Surface & Coatings Technology,* vol. 374, pp. 889-896, 2019.

[9] L. Makkonen, "Atmospheric Icing on Sea Structures," US Army Corps of Engineers Cold Regions Research & Engineering Laboratory, 1984.

[10] C. Ryerson, "Assessment of Superstructure Ice Protection as Applied to Offshore Oil Operations Safety," US Army Corps of Engineers, Hanover, New Hampshire, USA, 2008.

[11] A. R. Dehghani-Sanij, S. R. Dehghani, G. F. Naterer and Y. S. Muzychka, "Sea spray icing phenomena on marine vessels and offshore structures: Review and Formulation," *Ocean Engineering,* vol. 132, pp. 25-39, 2017.

[12] Fisheries and Oceans Canada, "Ice Navigation in Canadian Waters," Icebreaking Program, Maritime Services Canadian Coast Guard, Ottawa, Ontario, 2012.

[13] H. Brazil, R. Conachey, G. Savage and P. Baen, "Electrical Heat Tracing for Surface Heating on Arctic Vessels and Structures to Prevent Snow and Ice Accumulation," *IEEE Transactions of Industry Applications,* vol. 49, no. 6, 2013.

[14] G. G. Koenig and C. C. Ryerson, "An investigation of infrared deicing through experimentation," *Cold Regions Science and Technology,* vol. 65, pp. 79-87, 2011.

[15] T. Rashid, H. A. Khawaja and K. Edvardsen, "Review of marine icing and anti-/de-icing systems," *Journal of Marine Engineering & Technology,* vol. 15, no. 2, pp. 79-87, 2016.

[16] R. Zaki and A. Barabadi, "Application of de-icing techniques for arctic offshore production facilities," in *International Conference on Ocean, Offshore and Arctic Engineering*, San Francisco, California, USA, 2014.

[17] V. Hejazi, K. Sobolev and M. Nosonovsky, "From superhydrophobicity to icephobicity: forces and interation analysis," *Scientific Reports,* vol. 3, p. 2194, 2013.

[18] B. Liu, K. Zhang, C. Tao, Y. Zhao, X. Li, K. Zhu and X. Yuan, "Strategies for anti-icing: low surface energy or liquid-infused?," *RSC Advances,* vol. 6, pp. 70251-70260, 2016.

[19] P. Kim, T.-S. Wong, J. Alvarenga, M. Kreder, W. E. Adorno-Martinez and J. Aizenberg, "Liquid-Infused Nanostructured Surfaces with Extreme Anti-Ice and Anti-Frost Performance," *ACS Nano,* vol. 6, no. 8, pp. 6569-6577, 2012.

[20] A. A. Yancheshme, A. Allahdini, K. Maghsoudi, R. Jafari and G. Momen, "Potential anti-icing applications of encapsulated phase change material–embedded coatings; a review," *Journal of Energy Storage,* vol. 31, 2020.

[21] S. H. Kim, "Fabrication of Superhydrophobic Surfaces," *Journal of Adhesion Science and Technology,* vol. 22, pp. 235-250, 2008.

[22] Ç. K. Söz, E. Yılgör and İ. Yılgör, Superhydrophobic Polymer Surfaces: Preparation, Properties, and Applications, Istanbul, Turkey: Smithers Rapra Technology Ltd, 2016.

[23] D. Y. Kwok and A. W. Neumann, "Contact angle measurement and contact angle interpretation," *Advances in Colloid and Interface Science,* vol. 81, pp. 167 - 249, 1999.

[24] Y. Si and Z. Guo, "Superhydrophobic nanocoatings: from materials to fabrications and to applications," *Nanoscale,* vol. 7, pp. 5922-5946, 2015.

[25] A. Hooda, M. S. Goyat, J. K. Pandey, A. Kumar and R. Gupta, "A review on fundamentals, constraints and fabrication techniques of superhydrophobic coatings," *Progress in Organic Coatings,* vol. 142, 202.

[26] S. Peng, W. Meng, J. Guo, B. Wang, Z. Wang, N. Xu, X. Li, J. Wang and J. Xu, "Photocatalytically Stable Superhydrophobic and Translucent Coatings Generated from PDMS-Grafted-SiO2/TiO2@PDMS with Multiple Applications," *Langmuir,* vol. 35, pp. 2760-2771, 2019.

[27] J. Xie, J. Hu, X. Lin, L. Fang, F. Wu, X. Liao, H. Luo and L. Shi, "Robust and anti-corrosive PDMS/SiO2 superhydrophobic coatings fabricated on magnesium alloys with different-sized SiO2 nanoparticles," *Applied Surface Science,* vol. 457, pp. 870-880, 2018.

[28] X. Zhao, Y. Li, B. Li, T. Hu, Y. Yang, L. Li and J. Zhang, "Environmentally benign and durable superhydrophobic coatings based on SiO2 nanoparticles and silanes," *Journal of Colloid and Interface Science,* vol. 542, pp. 8-14, 2019.

[29] A. Hooda, M. S. Goyat, A. Kumar and R. Gupta, "A facile approach to develop modified nano-silica embedded polystyrene based transparent superhydrophobic coating," *Materials Letters,* vol. 233, pp. 340-343, 2018.

[30] X. Gong and S. He, "Highly Durable Superhydrophobic Polydimethylsiloxane/Silica Nanocomposite Surfaces with Good Self-Cleaning Ability," *ACS Omega,* vol. 5, pp. 4100-4108, 2020.

[31] H. Liu, X. Li, L. Lv, Z. Liu and J. Chen, "Fast fabrication of silicone-modified polyurethane/SiO2 composite superhydrophobic coating with excellent anti-icing and self-cleaning behaviour," *Materials Research Express,* vol. 7, 2020.

[32] J. Liu, Z. A. Janjua, M. Roe, F. Xu, B. Turnbull, K. S. Choi and X. Hou, "Super-Hydrophobic/Icephobic Coatings Based on Silica Nanoparticles Modified by Self-Assembled Monolayers," *Nanomaterials,* vol. 6, p. 232, 2016.

[33] Y. Lai, J. Huang, Z. Cui, M. Ge, K. Zhang, Z. Chen and L. Chi, "Recent advances in TiO2-based nanostructured surfaces with controllable wettability and adhesion," *Materials Views,* vol. 12, no. 16, pp. 2203-2224, 2016.

[34] J. Wu, J. Chen, J. Xia, W. Lei and B. Wang, "A Brief Review on Bioinspired ZnO Superhydrophobic Surfaces: Theory, Synthesis, and Applications," *Advances in Materials Science and Engineering,* 2013.

[35] C. Yang, F. Wang, W. Li, J. Ou, C. LI and A. Amirfazli, "Anti-icing properties of superhydrophobic ZnO/PDMS composite coating," *Applied Physics A,* 2015.

[36] E. Jenner, C. Barbier and B. D'Urso, "Durability of hydrophobic coatings for superhydrophobic aluminum oxide," *Appied Surface Science,* vol. 282, pp. 73-76, 2013.

[37] X. Zhu, S. Zhou, Q. Yan and S. Wang, "Multi-walled carbon nanotubes enhanced superhydrophobic MWCNTs-Co/a-C:H carbon-based film for excellent self-cleaning and corrosion resistance," *Diamond & Related Materials,* vol. 86, pp. 87-97, 2018.

[38] S. Zhou, X. Zhu, L. Ma, Q. Yan and S. Wang, "Outstanding superhydrophobicity and corrosion resistance on carbon-based film surfaces coupled with multi-walled carbon nanotubes and nickel nano-particles," *Surface Science,* vol. 677, pp. 193-202, 2018.

[39] X. Liao, H. Li, L. Zhang, X. Su, X. Lai and X. Zeng, "Superhydrophobic mGO/PDMS hybrid coating on polyester fabric for oil/water separation," *Progress in Organic Coatings,* vol. 115, pp. 172-180, 2018.

[40] F. De Nicola, P. Castrucci, M. Scarselli, F. Nanni, I. Cacciotti and M. De Crescenzi, "Super-hydrophobic multi-walled carbon nanotube coatings for stainless steel," *Nanotechnology,* vol. 26, 2015.

[41] L. Calabrese, A. Khaskoussi and E. Proverbio, "Wettability and Anti-Corrosion Performances of Carbon Nanotube-Silane Composite Coatings," *Fibers,* vol. 8, no. 57, 2020.

[42] M. Ruan, Y. Zhan, Y. Wu, X. Wang, W. Li, Y. Chen, M. Wei, X. Wang and X. Deng, "Preparation of PTFE/PDMS superhydrophobic coating and its anti-icing performance," *RSC Advances,* vol. 7, pp. 41339-41344, 2017.

[43] Z. Luo, Y. Li, C. Duan and B. Wang, "Fabrication of a superhydrophobic mesh based on PDMS/SiO2 nanoparticles/PVDF microparticles/KH-550 by one-step dip-coating method," *RSC Advances,* vol. 8, pp. 16251-16259, 2018.

[44] L. Li, B. Li, J. Dong and J. Zhang, "Roles of silanes and silicones in forming superhydrophobic and superoleophobic materials," *Journal of Materials Chemistry A,* vol. 4, pp. 13677-13725, 2016.

[45] Z. Luo, Y. Li, C. Duan and B. Wang, "Fabrication of a superhydrophobic mesh based on PDMS/SiO2 nanoparticles/PVDF microparticles/KH-550 by one-step dip-coating method," *RSC Advances* , vol. 8, pp. 16251-16259, 2018.

[46] R. G. Karunakaran, C. H. Lu, Z. Zhang and S. Yang, "Highly Transparent Superhydrophobic Surfaces from the Coassembly of Nanoparticles," *Langmuir,* vol. 27, pp. 4594-4602, 2011.

[47] W. Li, Y. Zhan and S. Yu, "Applications of superhydrophobic coatings in anti-icing: Theory, mechanisms, impact factors, challenges, and perspectives.," *Progress in Organic Coatings*, vol. 152, no. 106117, 2021.

[48] F. Wang, T. E. Tay, Y. Sun, W. Liang and B. Yang, "Low-voltage and -surface energy SWCNT/poly(dimethylsiloxane) (PDMS) nanocomposite film: Surface wettability for

passive anti-icing and surface-skin heating for active deicing," *Composites Science and Technology,* vol. 184, no. 107872, 2019.

[49] N. Miljkovic, R. Enright and E. N. Wang, "Effect of Droplet Morphology on Growth Dynamics and Heat Transfer during Condensation on Superhydrophobic Nanostructured Surfaces," *ACS Nano,* vol. 6, no. 2, pp. 1776-1785, 2012.

[50] P. S. R. Beeram, "Characterization of ice adhesion strength over different surfaces pertinent to aircraft anti-/de-icing," Iowa State University, 2017.

[51] L. Makkonen, "Ice Adhesion - Theory, Measurements and Countermeasures," *Journal of Adhesion Science and Technology,* vol. 26, pp. 413-445, 2012.

[52] S. Ronneberg, J. He and Z. Zhang, "Standardizing the testing of low ice adhesion surfaces," in *Int. Workshop on Atmospheric Icing of Structures*, Reykjavik, 2019.

[53] V. Hejazi, K. Sobolev and M. Nosonovsky, "From superhydrophobicity to icephobicity: forces and interaction analysis," *Scientific Reports,* vol. 3, p. 2194, 2013.

[54] S. Lei, F. Wang, X. Fang, J. Ou and W. Li, "Icing behavior of water droplets impinging on cold superhydrophobic surface," *Surface & Coatings Technology,* vol. 363, pp. 362-368, 2019.

[55] J. Liu, J. Wang, L. Mazzloa, H. Memon, T. Barman, B. Turnbull, G. Mingione, K. Choi and X. Hou, "Development and evaluation of poly(dimethylsiloxane) based composite coatings for icephobic applications," *Surface & Coatings Technology,* vol. 349, pp. 980-985, 2018.

[56] S. Ji, W. He, K. Wang, Y. Ran and C. Ye, "Thermal Response of Transparent Silver Nanowire/PEDOT:PSS Film Heaters," *Small,* vol. 10, no. 23, pp. 4951-4960, 2014.

[57] V. F. Petrenko, "Pulse electro-thermal de-icer (PETD)," *Cold Regions Science and Technology,* vol. 65, no. 1, pp. 70-78, 2011.

[58] R. Li, W. Xu and D. Zhang, "Impacts of Thermal and Mechanical Cycles on Electro-Thermal Anti-Icing System of CFRP Laminates Embedding Sprayable Metal Film," *Materials,* vol. 14, no. 1589, 2021.

[59] O. Redondo, S. G. Prolongo, M. Campo, C. Sbarufatti and M. Giglio, "Anti-icing and de-icing coatings based Joule's heating of graphene nanoplatelets," *Composites Science and Technology,* vol. 164, pp. 65-73, 2018.

[60] X. Yao, S. Hawkins and B. Falzon, "An advanced anti-icing/de-icing system utilizing highly aligned carbon nanotube webs," *Carbon,* vol. 136, pp. 130-138, 2018.

[61] B. G. Falzon, P. Robinson, S. Frenz and B. Gilbert, "Development and evaluation of a novel integrated anti-icing/de-icing technology for carbon fibre composite aerostructures using an electro-conductive textile," *Composites: Part A,* vol. 68, pp. 323-335, 2015.

[62] M. Naftaly, S. Das, J. Gallop, K. Pan, F. Alkhalil, D. Kariyapperuma, S. Constant, C. Ramsdale and L. Hao, "Sheet Resistance Measurements of Conductive Thin Films: A Comparison of Techniques," *Electronics,* vol. 10, no. 960, 2021.

[63] S. K. Loganathan, V. Rollin and D. Kim, "Rapid Heat Generation using Carbon Nanotubes," American Institute of Aeronautics and Astronautics, Daytona Beach, FL, 2016.

[64] X. Huang, N. Tepylo, V. Pommier-Budinger, M. Budinger, E. Bonaccurso, P. Villedieu and L. Bennani, "A survey of icephobic coatings and their potential use in a hybrid coating/active ice protection system for aerospace applications," *Progress in Aerospace Sciences,* vol. 105, pp. 74-97, 2019.

[65] X. Lin, Y. Cao, X. Wu, H. Yang, J. Chen and W. Huang, "Microstructure and mechanical properties of laser forming repaired 17-4PH stainless steel," *Materials Science and Engineering A,* vol. 553, pp. 80-88, 2012.

[66] K. Choonee, R. Syms, M. Ahmad and H. Zou, "Post processing of microstructures by PDMS spray deposition," *Sensors and Actuators A: Physical,* vol. 155, pp. 253-261, 2009.

[67] MG Chemicals, "Techncial Datasheet - 843ER Liquid," [Online]. Available: https://www.mgchemicals.com/products/conductive-paint/conductive-epoxy-paints/copper-epoxy-paint/. [Accessed 20 08 2021].

[68] P. Wang, M. Chen, H. Han, X. Fan, Q. Liu and J. Wang, "Transparent and abrasion-resistant superhydrophobic coating with robust self-cleaning function in either air or oil," *Journal of Materials Chemistry A,* vol. 4, pp. 7869-7874, 2016.

[69] M. Mizuno, Y. Chaya, T. Takagi, K. Hirogaki and T. Hori, "Super high water-repellent treatments of various kinds of cloths using sol-gel method," *Sen'i Gakkaishi,* vol. 68, no. 4, 2011.

[70] B. J. Basu, V. D. Kumar and C. Anandan, "Surface studies on superhydrophobic and oleophobic polydimethylsiloxane–silica nanocomposite coating system," *Applied Surface Science,* vol. 261, pp. 807-814, 2012.

[71] C. Wang, T. Fuller, W. Zhang and K. Wynne, "Thickness Dependence of Ice Removal Stress for a Polydimethylsiloxane Nanocomposite: Sylgard 184," *Langmuir,* vol. 30, pp. 12819-12826, 2014.

[72] Z. Zhang, B. Ge, X. Men and Y. Li, "Mechanically durable, superhydrophobic coatings prepared by dual-layer method for anti-corrosion and self-cleaning," *Colloids and Surfaces A: Physicochemical and Engineering Aspects,* vol. 490, pp. 182-188, 2016.

[73] C. H. Xue, Z. D. Zhang, J. Zhang and S. T. Jia, "Lasting and self-healing superhydrophobic surfaces by coating of polystyrene/SiO2 nanoparticles and polydimethylsiloxane," *Journal of Materials Chemistry A,* vol. 2, pp. 15001-15007, 2014.

[74] Vaniman Manufacturing Co., "Problast - 80008," [Online]. Available: https://www.vaniman.com/product/problast-80008/. [Accessed 18 01 2022].

[75] Dataphysics, "OCA – Optical contact angle measuring and contour analysis systems," [Online]. Available: https://www.dataphysics-instruments.com/products/oca/. [Accessed 20 11 2020].

[76] Memorial University of Newfoundland, "Scanning Electron Microscope Laboratory," Memorial University of Newfoundland, 06 05 2020. [Online]. Available: https://www.mun.ca/creait/MAF/SEMMAIN_cs.php. [Accessed 07 02 2022].

[77] Elcometer Ltd., "Elcometer 456 Separate Coating Thickness Gauge," 2022. [Online]. Available: https://www.elcometer.com/en/coatings-inspection/all-coatings-inspection/dry-film-thickness/digital/elcometer-456-separate-coating-thickness-gauge.html. [Accessed 08 10 2022].

[78] A. Bateni, S. S. Susnar, A. Amirfazli and A. W. Neumann, "A high-accuracy polynomial fitting approach to determine contact angles," *Colloids and Surfaces A,* vol. 219, pp. 215-231, 2003.

[79] K. Poduska and X. Duan, "Liquid repellent surfaces to improve asset integrity and safety in harsh marine environments," Memorial University of Newfoundland, St. John's, 2019.

[80] J. J. Bae, S. C. Lim, G. H. Han, Y. W. Jo, D. L. Doung, E. S. Kim, S. j. Chae, T. Q. Huy, N. V. Luan and Y. H. Lee, "Heat Dissipation of Transpartent Graphene Defoggers," *Advanced Functional Materials,* vol. 22, pp. 4819-4826, 2012.

[81] Ulbrich Stainless Steels and Special Metals Inc., "17-4 PH® Stainless Steel, UNS S17400," [Online]. Available: https://www.ulbrich.com/alloys/17-4-ph-stainless-strip-coil-foil-wire/. [Accessed 31 05 2022].

[82] T. L. Bergman and A. S. Lavine, Fundamentals of Heat and Mass Transfer 8th Ed., Hoboken, NJ: John Wiley & Sons, Inc., 2017.

[83] S. A. Kulinich and M. Farzaneh, "How Wetting Hysteresis Influences Ice Adhesion Strength on Superhydrophobic Surfaces," *Langmuir,* vol. 25, no. 16, pp. 8854-8856, 2009.

[84] T. Bartels-Rausch, V. Bergeron, J. H. Cartwright, R. Escribano, J. L. Finney, H. Grothe, P. J. Gutierrez, J. Haapala, W. F. Kuhs, J. B. Pettersson, S. D. Price, C. I. Sainz-Diaz, D. J. Stokes, G. Strazzulla, E. S. Thomson, H. Trinks and N. Uras-Aytemiz, "Ice structures, patterns, and processes: A view across the icefields," *Reviews of Modern Physics,* vol. 84, 2012.

[85] J. Hu, K. Xu, K. Wu, B. Lan, X. Jiang and L. Shu, "The freezing process of continuously sprayed water droplets on the superhydrophobic silicone acrylate resin coating surface," *Applied Surface Science,* no. 317, pp. 534-544, 2014.

[86] J. Kim, J. Jeon, D. R. Kim and K. S. Lee, "Quantitative analysis of anti-freezing characteristics of superhydrophobic surfaces according to initial ice nuclei formation time and freezing propagation velocity," *International Journal of Heat and Mass Transfer,* no. 126, pp. 109-117, 2018.

[87] S. Z. Szilasi and L. Juhasz, "Selective etching of PDMS: Etching as a negative tone resist," *Applied Surface Science,* vol. 447, pp. 697-703, 2018.